UNIVERSITY OF CALIFORNIA SAN DIEGO

SAN DIEGO STATE UNIVERSITY

Opposed-Flow Flame Spread over Solid Fuels in Different Burning Regimes

A dissertation submitted in partial satisfaction of the
requirements for the degree Doctor of Philosophy

in

Engineering Sciences (Mechanical and Aerospace Engineering)

by

Luca Carmignani

Committee in charge:

San Diego State University

Professor Subrata Bhattacharjee, Co-chair
Professor Fletcher J. Miller

University of California San Diego

Professor Kalyanasundaram Seshadri, Co-chair
Professor Richard K. Herz
Professor Antonio L. Sánchez

2019

The Dissertation of Luca Carmignani is approved, and it is acceptable in quality and form for publication on microfilm and electronically:

_____

_____

_____

_____

Co-chair

_____

Co-chair

University of California San Diego

San Diego State University

2019

DEDICATION

To Mallery, for her patience and pure love.

To my parents, who did not get a chance to enjoy my achievements.

EPIGRAPH

Any technological advance can be dangerous. Fire was dangerous from the start, and so (even more so) was speech - and both are still dangerous to this day - but human beings would not be human without them.

Isaac Asimov, The Naked Sun

If you asked every engineer at NASA what the worst scenario for the Hab was, they'd all answer "fire." If you asked them what the result would be, they'd answer "death by fire."

Andy Weir, The Martian

TABLE OF CONTENTS

LIST OF FIGURES

LIST OF TABLES

LIST OF ABBREVIATIONS

BASS	Burning and Suppression of Solids
CFD	Computational Fluid Dynamics
CNC	Computer Numerical Control
EVA	Extra Vehicular Activity
FIAT	Flame Image Analyzer Tool
HVAC	Heating, Ventilation, and Air Conditioning
ISS	International Space Station
NASA	National Aeronautics and Space Administration
NIH	National Institute of Health
NIST	National Institute of Standards and Technology
PMMA	Polymethyl Methacrylate
RTD	Resistance Temperature Detectors
SSCE	Solid Surface Combustion Experiment

NOMENCLATURE

Symbols

B	Mass transfer number
c	Specific heat
E_a	Activation energy
g	Gravity acceleration
L_f	Flame length
L_g	Gas diffusive thermal length
L_p	Pyrolysis region length
$\dot{m}''$	Mass flux
V_g	Opposed-flow velocity
V_f	Flame spread rate
$\dot{r}$	Regression rate
r	Radius
r_{eff}	Effective radius
s	Stoichiometric coefficient
T_a	Activation temperature,
T_f	Flame temperature
T_p	Temperature of pyrolysis region
T_v	Vaporization temperature
x	Molar fraction

Greek Symbols

α	Thermal diffusivity
β	Burn angle (defined in Chapter 3)
δ	Boundary layer thickness
λ	Thermal conductivity

ν Kinematic viscosity

τ Fuel semi-thickness

τ_h Fuel depth heated by a flame

ρ Density

σ Stefan-Boltzmann constant

Subscripts

cyl Cylindrical geometry

eff Effective

g Gas phase

s Solid phase

th Thermal regime

thn Thin fuel

thk Thick fuel

∞ Free stream conditions

Superscripts

$'$ per unit width

$''$ per unit area

$'''$ per unit volume

ACKNOWLEDGEMENTS

The past few years have brought the best and worst days of my life. Personally, I feel lucky. No matter what, I have always been able to count on wonderful people. I did not get here by myself, and I am proud of it. I learned a lot from the people I met through this journey called life, and living in two continents definitely opened my mind.

I would like to start from thanking prof. Subrata Bhattacharjee from SDSU for his guidance and support both as an advisor and a person. His passion for teaching and problem solving are now part of my background. I would like to thank also prof. Kal Seshadri, my UCSD advisor, for following my progress throughout the years and his input on my work.

I would also like to thank the professors that assisted me with important feedback and discussions: professors Fletcher Miller, Antonio Palacios, Joaquin Camacho, and John Abraham from SDSU, and professors Carlos Coimbra, Richard Herz and Antonio Sánchez from UCSD.

Special thanks also to the NASA Glenn Research Center group from SoFIE and BASS, including Dr. Paul Ferkul, Dr. Sandra Olson, Dr. David Urban, and professors Carlos Fernandez-Pello, James T'ien, Ya-Ting Liao, Michael Gollner for their feedback and advice on my work at the monthly meetings and conferences.

And of course thank you to all the students I had the pleasure to work with in the SDSU laboratory, Blake, Grayson, Ken, Robert, Yonatan, the exchange students from Germany Daniel, Thomas, Chris, Onur, Peter, Ahmet, David and Eddie, and all the students that assisted me with the experiments.

Besides the people that helped me with my research, I have to thank the ones who have helped me through the struggles and adventures of these years. My wife Mallery, with her patience and genuine love has been my starlight; thank you for always being of my side.

Thanks to my sister Micol, one of the strongest women I know, for her help and sacrifices during our turbulent life.

And thanks to all of my friends, spread out through the world, who continue listening to my stories and adventures, and more importantly being people I can always count on.

Parts of Chapter 1 have been published in the Fire Safety Journal (S. Bhattacharjee, M. Laue, L. Carmignani, P. Ferkul, S. Olson, Opposed-flow flame spread: a comparison of microgravity and normal gravity experiments to establish the thermal regime, Fire Saf. J. 79, pp. 111-118, 2016). The dissertation author was among the primary contributors of this publication.

Chapter 2, in part, has been published in Fire Technology (L. Carmignani, G. Celniker, S. Bhattacharjee, The effect of boundary layer on blow-off extinction in opposed-flow flame spread over thin cellulose: experiments and a simplified analysis, Fire Technol. 53, pp. 967-982, 2017; L. Carmignani, K. Dong, S. Bhattacharjee, Radiation from flames in a microgravity environment: experimental and numerical investigations, Fire Technol., 2019, in press) and Combustion and Flame (L. Carmignani, S. Bhattacharjee, S. Olson, P. Ferkul, Boundary layer effect on opposed-flow flame spread and flame length over thin polymethyl-methacrylate in microgravity, Combust. Sci. Technol. 190, pp. 534-548, 2018). The thesis author was the primary investigator in these publications. Parts of Chapter 2 have also been published in the Applied Thermal Engineering Journal (G. Lange, L. Carmignani, S. Bhattacharjee, Thermal radiation measurements of downward spreading flames, App. Thermal Engin., 2019, in press) and Fire Safety Journal (S. Bhattacharjee, L. Carmignani, G. Celniker, B. Rhoades, Measurement of instantaneous flame spread rate over solid fuels using image analysis, Fire Saf. J. 91, pp. 123-129, 2017), of which the dissertation author was among the primary contributors in these papers.

Chapter 3, in part, has been published in the Proceedings of the Combustion Institute (T. Delzeit, L. Carmignani, T. Matsuoka, S. Bhattacharjee, Influence of edge propagation on downward flame spread over three-dimensional PMMA samples, Proc. Combust. Inst. 37, pp. 3203-3209, 2019) and Fire Technology (L. Carmignani, B. Rhoades, S. Bhattacharjee, Correlation of Burning Rate with Spread Rate for Downward Flame Spread Over PMMA, Fire Technol. 54, pp. 613-624, 2018) and Combustion Science and Technology (L. Carmignani, S. Bhattacharjee, Burn Angle and Its Implications on Flame Spread Rate, Mass Burning Rate, and Fuel Temperature for Downward Flame Spread over Thin PMMA, Combust. Sci. Technol., 2019, in press). The thesis author was the primary investigator in these publications.

Chapter 4, in part, has been published on the Fire Technology Journal (L. Carmignani, G. Celniker, S. Bhattacharjee, The effect of Boundary Layer on Blow-Off Extinction in Opposed-Flow Flame Spread over Thin Cellulose: Experiments and Simplified Analysis, Fire Technol. 53, pp. 967-982, 2017) and other parts are extracted from (L. Carmignani, O. Kaskir, E. Tagger, S. Bhattacharjee, S., Connecting Burning Rate and Flame Spread Rate in Opposed-Flow Flame Spread over Flat Fuel Beds, 11th U.S. National Combust. Meeting, Pasadena CA, March 24-27, 2019). The thesis author was the primary investigator in these publications. Parts of Chapter 4 have also been published in Combust. Theory and Modelling (S. Bhattacharjee, L. Carmignani, Burn angle in forced and natural convection: a simplified scaling approach, Comb. Sci. Modelling 23, pp. 956-968, 2019), of which the dissertation author was among the primary contributors in these papers.

Chapter 5, in part, has been published in Combustion Science and Technology (L. Carmignani, S. Bhattacharjee, S.L. Olson, P.V. Ferkul, Boundary Layer Effect on Opposed-Flow Flame Spread and Flame

Length over Thin Polymethyl-Methacrylate in Microgravity, Combust. Sci. Technol. 190, pp. 534-548, 2018), Fire Technology (L. Carmignani, K. Dong, S. Bhattacharjee, Radiation from flames in a microgravity environment: experimental and numerical investigations, Fire Technol., 2019, in press), and other parts are extracted from (L. Carmignani, S. Sato, S. Bhattacharjee, Flame spread over acrylic cylinders in microgravity: effect of surface radiation on flame spread and extinction, 48th ICES, Albuquerque, NM, July 2018). The thesis author was the primary investigator in these publications.

VITA

2011 Bachelor of Science in Aerospace Engineering, University of Pisa, Italy

2014 Research Assistant, San Diego State University, USA

2015 Master of Science in Space Engineering, University of Pisa, Italy

2019 Doctor of Philosophy in Engineering Sciences (Mechanical and Aerospace Engineering), University of California San Diego, San Diego State University, USA.

PUBLICATIONS

L. Carmignani, K. Dong, S. Bhattacharjee, Radiation from flames in a microgravity environment: experimental and numerical investigations, Fire Technol., 2019 (in press)

L. Carmignani, S. Bhattacharjee, Burn angle and its implications on flame spread rate, mass burning rate, and fuel temperature for downward flame spread over thin PMMA, Comb. Sci. Technol., 2019 (in press)

G. Lange, **L. Carmignani**, S. Bhattacharjee, Thermal radiation measurements of downward spreading flames, Appl. Therm. Eng. 160, 2019

S. Bhattacharjee, **L. Carmignani**, Burn Angle in Forced and Natural Convection: A Simplified Scaling Approach, Comb. Theory and Modelling 23, pp. 956-968, 2019

T. Delzeit, **L. Carmignani**, T. Matsuoka, S. Bhattacharjee, Influence of edge propagation on downward flame spread over three dimensional PMMA samples, Proc. Combust. Inst. 37, pp. 3203-3209, 2018

L. Carmignani, B. Rhoades, S. Bhattacharjee, Correlation of burning rate with spread rate for downward flame spread over PMMA, Fire Technol. 54, pp. 613-624, 2018

L. Carmignani, S. Bhattacharjee, S. Olson, P. Ferkul, Boundary Layer Effect on Opposed Flow Flame Spread and Flame Length over Thin Polymethyl Methacrylate in Microgravity, Combust. Sci. Technol. 190, pp. 534-548, 2018

S. Bhattacharjee, **L. Carmignani**, G. Celniker, B. Rhoades, Measurement of Instantaneous Flame Spread Rate Over Solid Fuels Using Image Analysis, Fire Saf. J. 91, pp. 123-129, 2017

L. Carmignani, F. Lotti, S. Bhattacharjee, Comparison of flame spread and blow off extinction over vertical and horizontal PMMA samples, Advance Publication of JSME, 2016

L. Carmignani, G. Celniker, S. Bhattacharjee, The effect of Boundary Layer on Blow Off Extinction in Opposed Flow Flame Spread over Thin Cellulose: Experiments and Simplified Analysis, Fire Technol. 53 , pp. 967-982, 2016

S. Bhattacharjee, M. Laue, **L. Carmignani**, P. Ferkul, S. Olson, Opposed flow flame spread: A comparison of microgravity and normal gravity experiments to establish the thermal regime, Fire Saf. J. 79, pp. 111-118, 2016

FIELDS OF STUDY

Major Field: Mechanical Engineering

Studies in Combustion

Prof. Subrata Bhattacharjee and Prof. Kalyanasundaram Seshadri

ABSTRACT OF THE DISSERTATION

Opposed-Flow Flame Spread over Solid Fuels in Different Burning Regimes

by

Luca Carmignani

Doctor of Philosophy in Engineering Sciences (Mechanical and Aerospace Engineering)

University of California San Diego, 2019

San Diego State University, 2019

Professor Subrata Bhattacharjee, Co-Chair

Professor Kalyanasundaram Seshadri, Co-Chair

Several aspects of opposed-flow flame spread are experimentally investigated because of their relevance in fire safety studies. Different burning regimes based on the intensity of the opposed flow velocity are identified for acrylic fuels. In downward flame spread, where the flow around a flame is only naturally induced by gravity, the spread rate is highly dependent on fuel size and geometry. The fuel cross-sectional shape is experimentally varied, and a formula which takes into account geometrical effects is proposed by extending previous solutions for two-dimensional flames.

The burning region of a solid fuel shows a consistent slope due to the competition between flame spread and surface regression. The angle at the vertex of the pyrolysis region, called burn angle, can be used to indirectly calculate the fuel burning rate. The burn angle depends on fuel thickness; a numerical model and a scale analysis are used to explore the reasons for this behavior.

Next, the effect of a forced flow is investigated. The extreme case of blow-off extinction over thin fuels is considered, with flames extinguishing at locations determined by the flow velocity. Results suggest that the interaction between fuel and flow field is more important than the dependence on fuel thickness. The evolution of flame structure and pyrolysis also appear to be driven by flow interactions. A scale analysis is used to explore these dependencies.

Finally, previous microgravity experiments are used to explore differences and similarities with ground-based results. By suppressing the buoyant flow, flame radiation becomes essential for the flame spread process. The experimental conditions are simulated numerically to describe the importance of a developing boundary layer in this regime.

A numerical parametric study of the radiative emission of flames in microgravity, inspired by the experimental data, shows its dependence on flame area, mass burning rate and flame temperature by changing the burning conditions. For these small flames, soot does not seem to dominate flame radiation, although its generation increases with fuel thickness, oxygen concentration and flow velocity.

The experiments in microgravity considered in this work showed flame extinction in a quiescent environment. However, two acrylic cylinders at higher oxygen concentrations from a previous investigation can burn vigorously. To clarify whether these flames are stable, a scale analysis is used to study the influence of surface curvature on radiation losses.

Chapter 1

Fire Safety: From Earth to Space

1.1 Diffusion Flames

Combustion has always played a crucial role in the progress of humanity, providing a heat source for cooking, forging metals and eventually for energy production. Flames and fires, seen as symbols of uncontrollable destruction and divine punishment by our ancestors, have become an essential part of our daily life thanks to a progressive understanding of the matter. Despite the progress in the field, several aspects of fires are still enigmatic and need to be explained in order to lessen the risks posed by fires to human lives and the environment. Because of the complexity of fires and their dependence on a variety of conditions, it is often useful to consider flames on a smaller scale to understand the fundamental mechanism of fire processes. In this regard, flames could be seen not only as building elements of larger fires, but also as their initial stages. It is therefore important to know under which conditions these flames can grow or diminish.

Generally speaking, combustion requires a fuel, an oxidizer, and an ignition source. Several categorizations for flames exist depending on the nature of the reactants and their consumption. A first classification is based on whether or not the fuel and oxidizer are mixed before ignition, defining respectively pre-mixed or diffusion flames. In diffusion flames the oxidizer is driven by concentration gradients of the participating species or convection (in case of an external flow). While pre-mixed flames prevail in energy applications to guarantee a uniform combustion, in nature diffusion flames are more common since fuel and oxidizer are usually in different phases, i.e. a condensed fuel (liquid or solid) burning in atmospheric air (gas). Diffusion flames can present pre-mixed regions, especially in the outer zones where the lower fuel concentration can mix with the oxidizer before reacting, but this effect is usually neglected in flame modelling for simplicity.

When a condensed fuel is heated up, its chemical components are released from the surface in a

gaseous phase. The transition process between condensed and vaporized fuel is specific of its nature and could include partial melting for solid fuels. This process is commonly referred to as pyrolysis, although the name thermolysis would be more appropriate. While they both indicate the molecular breakdown of a fuel due to high temperature, pyrolysis alludes to the absence of oxidizers (or presence of an inert atmosphere) during the process. Clearly a flame can only develop when an oxidizer is available. However, since the literature adopted the term pyrolysis in a broader way, including the problem of flame spread, we will use that for consistency with previous works.

The vaporized fuel from the pyrolysis region leaves the surface and mixes with the oxidizer, and a flame develops along the reactions zone. Incomplete products from flame reactions often consist of microscopic solid particles (soot) that make a flame more luminous (solid particles can emit radiation in a broader spectrum than gas molecules). For hydrocarbon fuels the sooty flame has the familiar yellow-orange color. In general, the total flame area is larger than the sooty region because of the reaction zones with lower rates (which are usually less luminous). Typically, flames are not attached to the condensed fuel because of the fuel molecules leaving the surface with a non-zero velocity (fluid dynamic interactions) and low concentration of the oxidizer on the fuel surface (chemistry), so the distance between flame and surface varies with the burning conditions.

Another important classification is based on the ability of a flame to spread. Sometimes it is necessary to look at stationary flames to study their behavior in time and to measure their growth. On the other hand, if a flame is not confined and finds more fuel to burn, such as a flame burning along a piece of paper, it is considered a spreading flame. The location of spreading flames along a fuel changes in time, but quasi-steady state conditions can be identified. It could be argued that non-spreading flames still change their position in time because of the regression of the fuel surface. To avoid confusion, we will indicate the variation of flame position along a fuel surface with the term flame spread, while the change in position along the fuel depth will be called flame regression.

A spreading flame can interact with an external flow, such as with wind or an air flow from a ventilation system. Flames can spread along the direction of flow velocity, or in the opposite direction. We distinguish these two cases as concurrent and opposed-flow flame spread respectively. Both categories are important in fire safety as they represent different aspects of flame-flow interactions, but in this work we will focus on the opposed flow configuration.

1.2 Flame Spread: Fire Safety Implications

Naturally, flames need more fuel in order to grow, and spreading flames reflect a more common situation in fire safety applications than stationary flames. One of the main objectives of fire safety is to minimize the damage of an accidental fire by limiting its growth. Due to the variety of scenarios, however, it is difficult to identify universal criteria to prevent fires.

To assess the possible risks of a fire, it is necessary to know the type of material that is burning. The chemical composition and structure of a fuel determine its flammability in a given environment. This information, however, is not enough to describe a potential fire, because fuel geometry and burning conditions affect flame growth as well.

Flammability tests provide fundamental guidelines for safer designs of areas at risk. There are many test methods based on their industrial applications; entire components or small samples are burnt in given conditions to measure smoke emissions, burning time, etc. Flammability tests can also compare different materials burning in the same conditions. In this way, safer materials can be selected for risky situations.

Knowing the time needed by a fire to become uncontrollable is extremely useful to develop safety procedures, especially when human lives are at risk. It becomes even more important when the escape solutions are limited, i.e. in enclosed habitats such as submarines, airplanes or spacecraft. The internal conditions which include pressure and temperature (in some cases also oxygen concentration) are typically controlled by HVAC systems, and could differ from the atmospheric levels. This variability could reflect in unexpected behavior or accidental flames, such as higher spread rates or toxic emissions.

Flame spread and mass burning rates over solid fuels are important parameters of the problem since they are related to the time required to burn a fuel. Furthermore, their dependencies on burning conditions can be theoretically studied in simplified configurations. The combination of flammability results with theoretical interpretation is often the best way to improve fire safety.

1.3 Microgravity Flames: Similarities

In microgravity the hot products of a flame are not moving upward because of their density gradient anymore, so the naturally induced buoyant flow is suppressed. Therefore, products can only diffuse away (at a much lower velocity) from the reaction zone without a preferential direction.

A qualitative representation of the microgravity environment is given in Fig. 1.1, where the blue arrows (facing the flame) and yellow arrows (leaving the flame) indicate respectively the oxidizer and products directions. In normal gravity the oxidizer reaches the reaction zone by diffusion and convection, while the

lighter products move mostly upward generating a flow in the vicinity of the flame that helps the mixing of the reactants. In microgravity, on the other side, diffusion drives products and oxidizer in opposite directions according to their concentration gradients. A candle flame, for example, in microgravity does not have the typical tailored shape; it is instead hemispherical (see right pictures of Fig. 1.1). The combination of a larger time available for chemical reactions to occur and a lower flame temperature due to radiation losses cause a lower generation of soot, making flames dimmer and sometimes hard to detect. Diffusion can limit the amount of oxidizer available in the reaction zone, and radiation usually acts as a loss mechanism, but this does not imply flame extinction in microgravity; it has been proven that candle flames can burn steadily for as long as 45 minutes in microgravity [1].

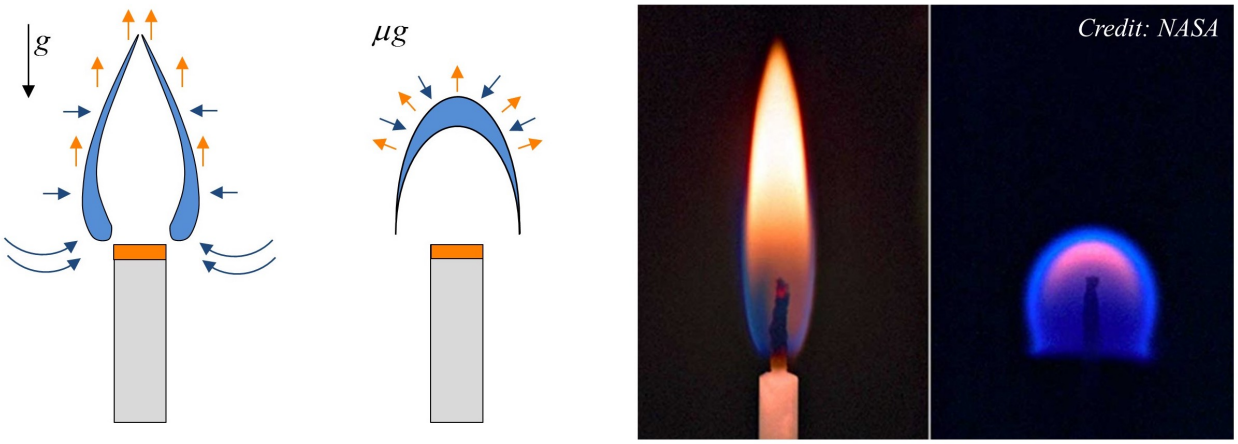

Figure 1.1: When gravity affects a flame, the hot products (yellow arrows) move upward giving the tailored shape typical of a candle flame. In microgravity, the hot products diffuse without a preferential direction and the flame becomes spherical, as shown in the right picture.

Microgravity conditions can be obtained in many ways and for different duration; the most common methods include drop tower tests (few seconds), parabolic flights (seconds), sounding rockets (minutes), or in orbit, with the latter being the most desirable because of the time flexibility and the low g-jitter levels. The drawback of these experiments is the cost in terms of money and preparation (which can last for years). There are some alternative methods to simulate microgravity conditions in ground-based experiments depending on the configuration considered. Flames over solid fuels in normal gravity shows a similar behavior to the ones from microgravity in a narrow channel or at low pressures [2, 3].

The microgravity environment offers the unique possibility of studying basic combustion phenomena. Many fields of combustion research have benefited from microgravity experiments, from droplet combustion to soot formation [4] and gaseous jet flames [5]. In fire safety, and specifically for the flame spread problem over solid fuels, microgravity gives an opportunity to study the influence of fuel geometry, flow velocity field,

oxidizer concentration and total pressure without the influence of buoyancy.

Flames in microgravity can be very similar to normal gravity flames, but also behave very differently. The lack of buoyancy has a strong influences also on the heat flux exchange between flame and fuel surface, which has to be enough to vaporize more fuel. Heat conduction can be very slow without the buoyant flow, allowing radiation to gain relevance in the problem. The different balance of heat fluxes can have consequences on the flammability of a material; flames over acrylic samples that easily burn in normal gravity can extinguish in microgravity because of the greater influence of radiation losses [6].

It is practically impossible to eliminate all the possible ignition sources in a habitable environment. As long as several questions regarding flames in microgravity remain unanswered the safest approach is improving fire prevention. To ensure the selection of safe materials onboard spacecraft, NASA requires designers to follow the testing methods described by NASA-STD-6001 [7]. A material passes the test if none of five samples burn for more than 15 cm in an upward configuration and do not propagate a flame by transferring burning debris. In normal gravity upward flame spread is helped by buoyancy, so it a worst-case scenario. However, materials considered safe for terrestrial applications can be dangerous in microgravity [8, 9]. Moreover, future space exploration missions might use non sea-level conditions, with higher oxygen concentrations (around 34%) and a lower pressure (~ 60 kPa) to reduce the time required for EVAs and the load on the spacecraft structure [10]. It is not clear how these conditions will affect material flammability [11], and better understanding of the flame behavior in microgravity is indeed necessary to keep crew and spacecraft safe.

1.4 Problem Description

In this work we consider diffusion flames spreading against an opposed flow (natural or forced). The symmetric half of a generic flame over a solid fuel with semi-thickness τ is considered in detail in Fig. 1.2. In our reference system, x is positive along the spreading direction of the flame with origin at the flame leading edge, whereas y is along the vertical direction away from the fuel surface (located at $y = 0$), and z reflects the fuel width. By considering a section of a flame with infinite width, the problem becomes two-dimensional.

The flame in Fig. 1.2 has a length L_f and is spreading at a rate V_f against a flow velocity V_g, which can be naturally driven or forced. Part of the heat generated by the flame vaporizes the solid fuel and is proportional to the mass flux $\dot{m}''$. The pyrolysis region (orange section in Fig. 1.2, with length L_p) does not necessarily start at the flame leading edge, but usually this difference is small compared to the other length scales of the problem and can be neglected. The temperature gradient inside the solid fuel depends on its conductivity, and will affect the fuel up to a depth τ_h that is in general larger than τ. It should be noticed

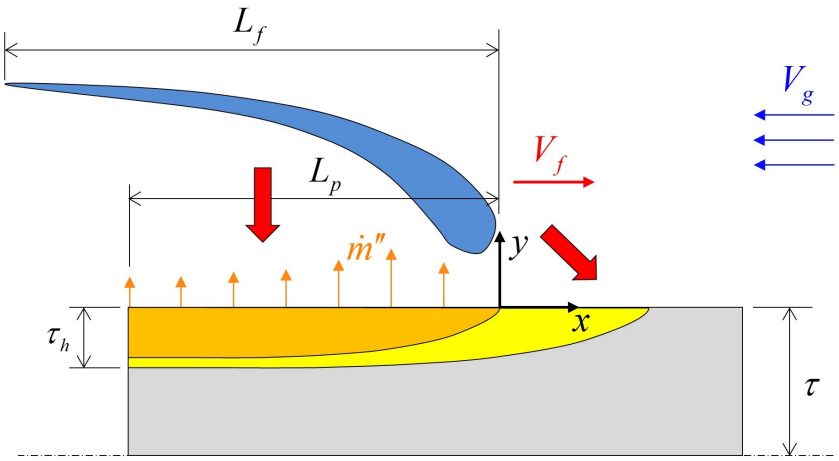

Figure 1.2: Schematics of a generic flame spreading over a solid fuel. The coordinate system is located on the fuel surface by the flame leading edge.

that the direction of gravity is not specified, so the generic concepts described for the case of Fig. 1.2 apply to any flame facing an opposed-flow velocity V_g, either spreading vertically, horizontally or in absence of gravity.

Even in this simplified configuration a number of complexities can arise. The temperature gradient inside the fuel will vary with its thickness. Furthermore, the chemistry to predict the burning rate of the fuel or the gas-phase reactions may not be well known. Despite the simplifications that the assumption of a two-dimensional laminar flow brings in, a theory that includes gas phase radiation, chemical and pyrolysis kinetics is still too complicated to yield a solution without the application of numerical analysis or semi-empirical models. However, it is still possible to estimate which aspects of the problem play a major role by making appropriate assumptions, for example through scale analysis.

Polymethyl Methacrylate (PMMA) is an acrylic material that has been widely used in previous studies [12] because it does not produce char. PMMA is an extremely versatile material thanks to its similarity with glass, used from construction to medical applications. PMMA can be produced by extrusion or cell casting, with the latter method giving a more compacted and resistant structure. When PMMA is heated up bubbles of the monomer MMA start forming [13]. Bubbles in extruded PMMA seem to grow faster than in cast PMMA, which could be the cause of the common dripping of melted PMMA that can occur during flame experiments. All the samples considered in this work are made of cast PMMA, which is a non-charring material, with the exception of the 0.05 and 0.075 mm films that are extruded (these small thicknesses of PMMA are commercially available only from extrusion). However, for such small thicknesses the dripping does not compromise flame spread experiments. It should be noticed that the thickness values

refer to the nominal values given by the manufacturers, although some small deviations were measured.

1.5 Flame Characteristics

Opposed-flow flame spread over solid fuels has been under investigation for more than five decades because of its importance in fire safety and basic understanding of combustion phenomena [12, 14]. To find the driving mechanisms of the problem, researchers modeled different aspects of flame spread by isolating the influence of single parameters (oxygen concentration, flow velocity) on many flame aspects, from spread rate to soot production, etc.

Throughout this dissertation, we will focus our attention on the variation of three main characteristics: flame spread rate, mass burning rate, and flame length. Flame spread rate, besides the importance in fire safety, is a comprehensive parameter of a flame because of its dependence on the heat conducted to the fuel upstream (which depends on the heat generated by the flame in the leading edge region and in general varies with the burning conditions). It has been shown that V_f mainly depends on the heat conducted in the gas phase [15], although the solid phase component can be important when the thermal conductivity is high [16].

The mass burning rate is another critical aspect of flames over condensed fuel, and it can be used to predict the size of a flame, its growth or even the radiative emission. It is the amount of vaporized fuel leaving the surface per unit time and is proportional to the incident heat flux, which is in general not uniform on the surface. Mass burning rates are highly dependent on the temperature of the pyrolysis region, which could vary with burning conditions or heat transfer. The mass burning rate determines the regression rate of a solid fuel. To avoid complicated direct measurements of mass burning rates, often the evolution of surface regression is used to indirectly estimate these values.

The length of a flame generated by a solid fuel is an important concern in fire safety. Longer flames could potentially reach other objects in the surroundings helping the growth of a fire. Experimentally, visible flames or temperature profiles are relatively easy to measure, and can provide information on the stability of a flame.

Diffusion flames strongly depend on the mixing of fuel and oxidizer. To evaluate how the burning conditions affect the reactants it is useful to introduce a time scale, the residence time. This is defined as the time spent by the oxidizer near the flame leading edge, and its comparison with other time scales of the problem can help us understanding the driving mechanisms responsible of flame spread. The chemical time, defined as the time needed by the reactions to occur, is another important time scale of the problem. If residence and chemical times are similar, we expect finite-rate chemistry to be important in the description

of a flame.

The ratio between residence time and chemical time is called Damköhler number, and can be used to define three main regimes of flame spread [17, 18]: (i) thermal regime, where reactions have enough time to occur and changes in the Damköhler number are not relevant; (ii) kinetic regime, where the Damköhler number becomes small and chemical kinetics becomes important. In microgravity, by suppressing the buoyant flow the residence time can drastically increase. This allows radiation to affect the heat transfer between flame and fuel, and we refer to this case as the (iii) radiative regime.

The structure of this dissertation follows the concept of the three regimes, analyzed separately in Chapter 3, 4, and 5. Specifically, we will look at how the flame characteristics mentioned above (spread rate, length and mass burning rate) vary in these three regimes. In the next Chapter, details about the experimental apparatuses and the numerical model used to collect the data are presented.

Parts of Chapter 1 have been published in the Fire Safety Journal (S. Bhattacharjee, M. Laue, L. Carmignani, P. Ferkul, S. Olson, Opposed-flow flame spread: a comparison of microgravity and normal gravity experiments to establish the thermal regime, Fire Saf. J. 79, pp. 111-118, 2016). The dissertation author was among the primary contributors of this publication.

Chapter 2

Experimental Set-up and Numerical Model

2.1 Experimental Parameters

The experimental conditions analyzed in this work have a relatively large range of forced flow velocities (0 - 150 cm/s), fuel thicknesses (0.05 - 25 mm), and fuel geometry. To study the influence of these variables many experimental apparatuses have been built and implemented during the years in the Computational Thermodynamics Laboratory at San Diego State University. The main ones consist of a wind tunnel (called Flame Tunnel, Sec. 2.2), the Flame Stabilizer (Sec. 2.3), which is a versatile set-up to fix a spreading flame in a stationary location, and the small-scale wind tunnel used for the experiments in microgravity (Sec. 2.4).

All the flame experiments are video recorded. A tool for image analysis has been internally developed to track a flame almost automatically. After presenting previous flame tracking methods found in literature, an overview of the MATLAB-based code is given in 2.5.

A numerical model previously developed and used to simulate flames over thin fuels is described in section Sec. 2.6.

2.2 The Flame Tunnel

A schematic representation of the Flame Tunnel is illustrated in Fig. 2.1. It is a wind tunnel with a square base of 20 $\times$ 20 cm, which necks down to a 10 $\times$ 10 cm section by the sample location at the top. The total height of the tunnel is about 80 cm. The Flame Tunnel is mounted on a greater structure built

with T-slot aluminum bars, at about 120 cm from the ground. The structure also allows the Flame Tunnel to rotate up to 180° with respect of the vertical direction, with steps of 30°.

The flow is generated by four computer fans (Antec® Tricool 92 mm) mounted on a steel plate placed at the bottom of the tunnel. The fans are controlled by an Arduino® microcontroller unit (MCU) which is connected to a computer running a MATLAB code. The speed of each fan is controlled by pulse width modulation (PWM), and one PWM pin was assigned to each fan. PWM works by turning the pin on and off very quickly with an adjustable duty cycle. There are 256 settings starting from 0 (always off) up to 255 (always on), and all of the settings in between have some intermediate duty cycle. The pin is either 0 or 5 V, and the setting determines how much time it spends on each state. Since the MCU cannot produce enough power for the whole fan system, each pin is connected to a transistor which controls the power from the 12 V power supply.

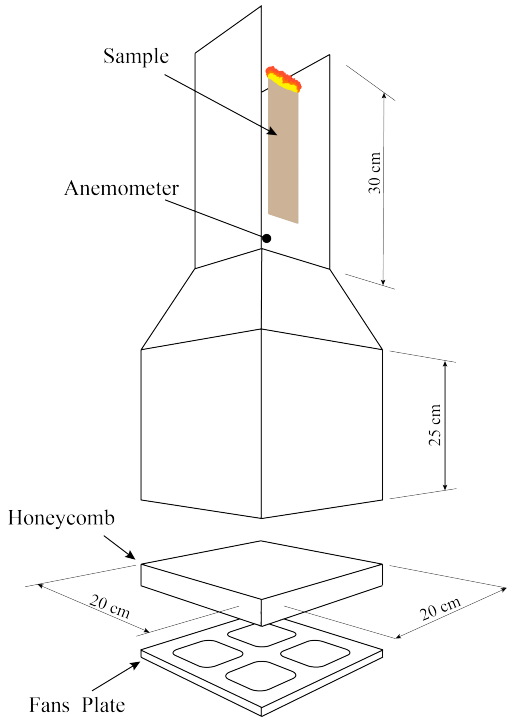

Figure 2.1: Schematic representation of the Flame Tunnel. The tunnel is mounted on a rotatable structure not indicated in the figure.

The flow generated by the fans passes through two layers of honeycomb (aluminum, pore size 6.35 mm, thickness of 12 mm) to reduce turbulence before reaching the sample. The honeycomb layer also protects the fans plate from possible dripping of acrylic fuel. Flow velocities up to 250 cm/s can be obtained in the upper section of the tunnel when all the fans are at full speed.

The measurement of flow velocity, especially at low values, can be challenging. Most of the commercially available anemometers (mechanical and hot-wire sensors) cannot measure velocities below 20 cm/s

since they are usually designed for HVAC systems. For this reason, in the first version of the Flame Tunnel the velocity was measured with two Resistance Temperature Detectors (RTDs). The RTDs (configuration 4100 Ω, platinum) were located about 5 cm below the sample and connected in a Wheatstone bridge. Only one RTD was actively heated, with its resistivity changing as a consequence of the flow velocity trying to cool off the sensor, and changes in resistivity reflected in the variable resistance of the Wheatstone bridge. The non-heated RTD adjusted its resistivity with the room temperature. In this way the measurements of the velocity were independent from it. The voltage difference from the RTDs was amplified and collected by the MCU, and a feedback control was employed to create constant velocity. Despite the high sensibility of the RTDs to flow velocity changes and the durability of the sensors, they had some practical limitations, such as reliability and maintenance. Every sensor adjustment could vary the contact between RTDs and the Flame Tunnel structure, affecting the RTD resistivity and therefore the velocity readings. Consequently, any change in the RTD position required a new velocity calibration. The RTDs calibration was carried on by matching the voltage output with velocity values independently obtained with an external anemometer.

To guarantee a better repeatability, the RTDs were substituted by an omni-directional air velocity transducer (TSI® 8475-03, the same used for the BASS experiments described in Sec. 2.4), which can measure flow velocities as low as 5 cm/s and up to 250 cm/s. This anemometer has an accuracy of ±3% on the reading and ±1% on full scale (smaller velocity ranges can be selected, reducing this error), and the velocity calibration is certified by NIST. During experiments, the anemometer can be influenced by the heat generated by a flame, causing the readings to change in time. For this reason the flow velocity is calibrated before the experiments and kept constant for the entire duration by controlling the fan voltage.

The Flame Tunnel was initially designed to test thin sheets of acrylic and cellulosic fuels, so the sample holder was not suitable for thicknesses larger than 0.5 mm. The upper part of the Flame Tunnel, including the sample holder, has been completely redesigned to accommodate thicker fuels. The current sample holder keeps the samples in compression with the help of screws adjustable from the front of the Flame Tunnel, and allows tests with thicknesses up to 25 mm. Flames over thick slabs of acrylic fuels can become very large in size, especially compared to the 10 × 10 cm section of the upper Flame Tunnel, and potentially ruin the apparatus. Therefore, the maximum sample thickness allowed in the Flame Tunnel is about 15 mm.

The sample ignition was included in the Flame Tunnel software and the user could decide when to start by heating up a Kanthal wire coil. The power supplied, however, was not enough to guarantee ignition at high flow velocities, and a higher power would drastically reduce the life of the Kanthal wire. This system was designed to work for the original sample holder, so it was removed when upgrading the Flame Tunnel. For the experiments carried on in this work, samples ignition is manually achieved by passing a blow torch

over the top cross-section of the sample until a stable flame (and uniform along the sample width) is obtained. The time required for ignition changes with thickness; while only a few seconds are sufficient to ignite thin samples, up to a few minutes can be necessary for the thicker fuels to establish a steady flame.

2.3 The Flame Stabilizer

The schematic of the Flame Stabilizer is shown in Fig. 2.2. Its purpose is to keep a spreading flame at the same vertical location by moving the sample holder in the opposite direction of flame spread [19]. This is convenient to produce a fixed coordinate system with respect to the leading edge of the flame. Conceptually, the Flame Stabilizer is divided in two parts: (i) flame stabilization and (ii) data acquisition system.

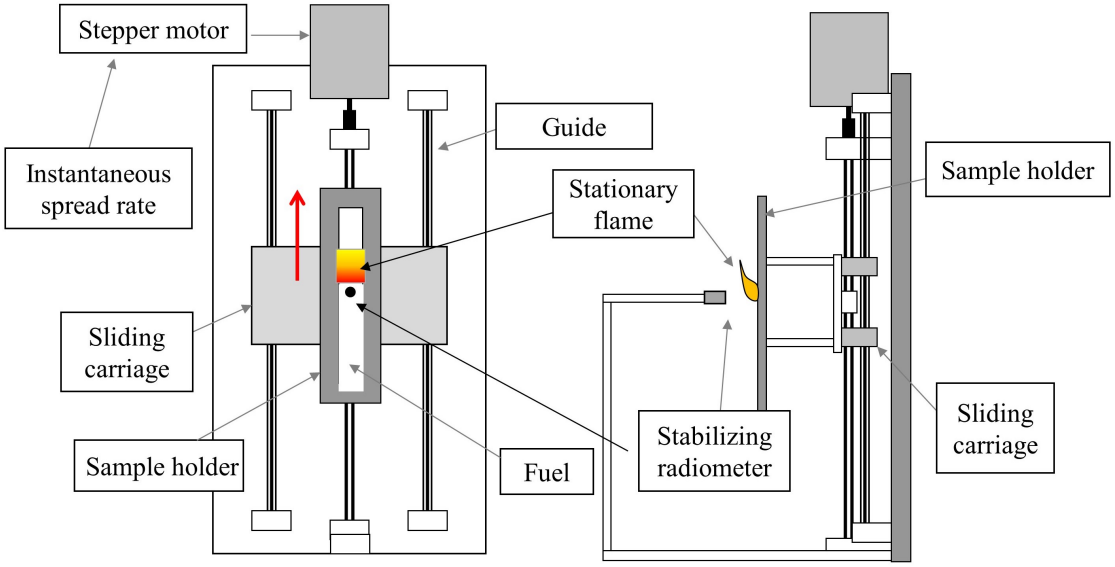

Figure 2.2: Schematic of the Flame Stabilizer apparatus.

Flame stabilization is achieved by moving the burning sample upwards at velocity V_f, the spread rate of the flame, effectively making the flame stationary in space. The basis for this comes from steady-state analytical modeling of a downward spreading flame, in which the fuel approaches the flame's leading edge at V_f and the oxidizer approaches the flame at the relative velocity of $V_g + V_f$. During downward spread, $V_g = 0$ sufficiently far upstream of the leading edge. The boundary conditions are slightly altered since stabilization creates a situation in which oxidizer approaches the flame at V_g and not $V_g + V_f$. However, it has been previously established experimentally and computationally that this change in boundary conditions due to flame stabilization has negligible effect since V_f is small compared to V_g induced by buoyancy [19].

The Flame Stabilizer uses a radiometer fixed to the laboratory coordinates to detect the leading edge

of the flame, whereas the earlier version used a thermocouple as the sensor [19]. The radiometer approach offers several benefits over the thermocouple; it is completely non-contact, eliminating any conductive loss through thermocouple leads and radiative loss through the thermocouple bead, that can affect the flame shape at the leading edge. Once the leading edge is detected, a PID (proportional gain, integral time, and derivative time) control system is used to actuate a stepper motor that moves vertically the sample holder at a speed equal to the flame spread rate (but opposite direction).

The radiometer used is a thermopile-style detector (2M thermopile) produced by Dexter Research. The radiometer is built on the design provided by Camperchioli [20] and used by Son [21]. It consists of the thermopile itself, a viewing window, encapsulation gas, and the housing. The 2M thermopile has an active area of 48 junctions between antimony (Sb) and bismuth (Bi) over a 2 $\times$ 2 mm area. Sapphire is chosen as the viewing window material to allow passage of wavelengths from 0.1 - 7.0 µm. Xenon (Xe) is used as the encapsulation gas, which has an increased sensitivity compared to the typically used argon (Ar). The opening on the radiometer's housing provides the detector with a field of view of 95°. The thermopile is mounted to a printed circuit board over the top of a temperature sensor used to measure the cold junction temperature. The board provides a reference voltage V_{ref} of 1.25 volts. The output voltage V_{out} from the thermopile is amplified by an onboard chip, and V_{out} ranges from V_{ref} to a limit of 5 volts, at which point the detector is fully saturated.

The data acquisition system is independent of flame stabilization and consists of a moving shelf where several sensors can be mounted. By using the same flame-fixed coordinate system indicated in Fig. 1.2, the shelf can be automatically moved with a MATLAB code and an Arduino controlling the stepper motors along the x and y directions, whereas along the z-axis the sensors have to be manually moved (we are currently working to automatize the motion along z as well).

For radiation measurements, a thermopile-style detector identical to the one used for flame stabilization is mounted on the acquisition system. The total radiation of a flame can be measured with the full field of view of the detector, but in many cases it is desirable to limit the area seen by the detector in order to explore radiation emissions from specific locations in the flame. To obtain line of sight radiation, the radiometer field of view can be modified by placing a covering plate with a small hole connected to a tube. By knowing the dimensions of the tube and the location away from the sample, a geometric analysis provides (see symbols in Fig. 2.3):

$$\theta = \frac{D}{L} = \frac{d}{2x} \qquad \rightarrow \qquad x = \frac{dL}{2D} \tag{2.1}$$

$$l = x + \frac{L}{2} = \frac{L}{2}\left(1 + \frac{d}{D}\right) \tag{2.2}$$

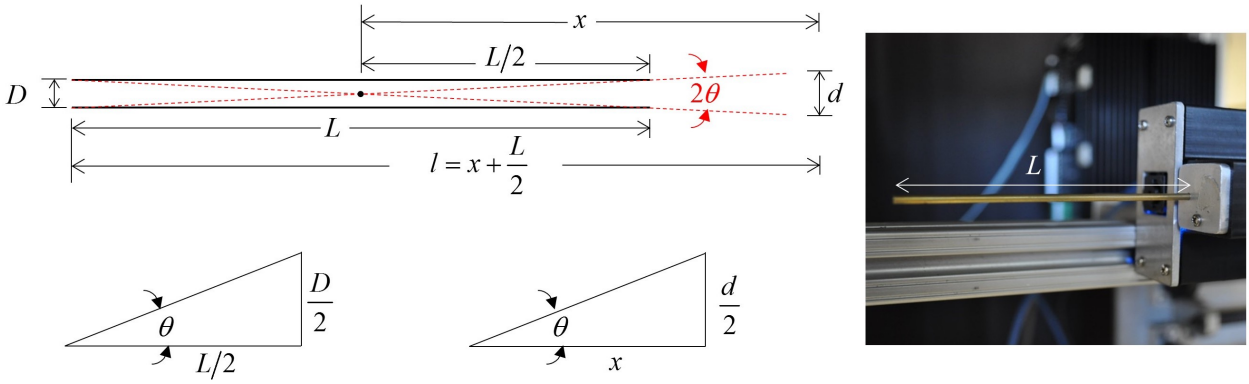

Figure 2.3: Geometric analysis for creation of line of sight faceplate.

A brass tube with a length L of 102 mm and inner diameter D of 1.5 mm (and an outer diameter of 2.38 mm) is inserted in a faceplate such that the radiometer sees a spot size with a diameter of 3 mm when the radiometer is positioned at the proper distance l of 153 mm away. Additionally, a removable black backboard is mounted in the Flame Stabilizer behind the controlling sensor to provide a uniform backing behind the burning samples for the probe on the opposing side.

The radiometer used for data acquisition was calibrated with a blackbody infrared (IR) light source (Oriel® 67030), which has a temperature range between 50 and 1050 °C. The radiometer was aligned with the blackbody by using the frontal aperture of the same diameter of the line-of-sight tube. The output voltages were measured with steps of 200 °C until the sensor got saturated. The radiation intensity of a blackbody is defined as:

$$i_b = \sigma T^4 / \pi \tag{2.3}$$

with σ being the Stefan-Boltzmann constant ($5.67 \cdot 10^{-8} \mathrm{W} \cdot \mathrm{m}^{-2} \cdot \mathrm{K}^{-4}$) and T the temperature in Kelvin. By taking into account the radiometer spectral range (going from 0.1 to 7 µm), we can express the relation between voltage and radiation intensity as:

$$V_{\mathrm{out}} = \mathrm{c} \cdot i_b \left(F_{0-\lambda_2} - F_{0-\lambda_1}\right) \tag{2.4}$$

where $F_{0-\lambda}$ is the fraction of blackbody emission in the wavelength range $0-\lambda$ and c is a proportionality constant to be determined experimentally. The measured voltages as function of the radiation intensity are reported in Fig. 2.4, which includes both total and partial emissions (by using the fraction emissions in Eq. 2.4). In the given temperature range the difference $F_{0-\lambda_2} - F_{0-\lambda_1}$ increases from a value of 0.112 at 50 °C to 0.817 at 700 °C. In the typical temperature range of PMMA flames (1000 - 2000 K depending on the burning conditions), we expect a large component of the total flame emission to be in the near and mid infrared regions, with $0.8 < F_{0-\lambda_2} - F_{0-\lambda_1} < 0.95$. Therefore, it is reasonable to simplify Eq. 2.4 to $V_{\text{out}} \approx \text{c} \cdot i_b$, obtaining $\text{c} = 4.37$ m^2 sr V/kW from Fig. 2.4.

A Logitech c615 High Definition webcam mounted next to the radiometer is used to capture still images during experiments to control the flame evolution (black square next to the tube on the right of Fig. 2.3). An optional face plate restricts the field of view to match that of the radiometer so that webcam captures just the part of the flame responsible for the radiometer output.

Samples to be tested are pinched between two steel plates held together by magnets, and the entire sample holder is kept vertical by aluminum bars. Samples are ignited at the top with a pilot flame and no dependence on the ignition procedure has been observed (flames over thin fuels reach steady state conditions in a few seconds).

The sample holder of the Flame Stabilizer allows the burning of thin samples up to 1.5 mm in thickness, and 30 mm in width. The sample length usually varies based on the speed of the flame, from a minimum of a few cm up to 50 cm. Flames usually get stabilized within 20 - 30 s.

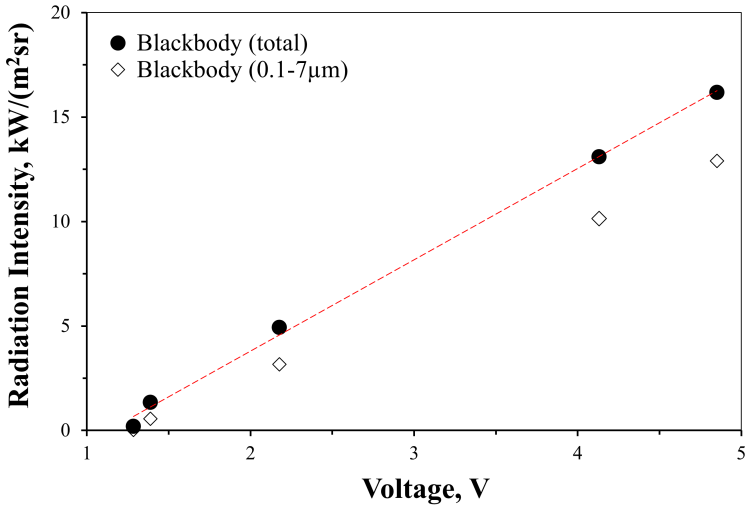

Figure 2.4: Comparison of the output voltages from the radiometer by considering the entire wavelength spectrum (total) and the operating band of the radiometer (0.1 - 7 µm).

2.4 The BASS Apparatus

BASS and the following BASS-II are recent investigations conducted onboard the ISS to study the flammability of solid materials [22, 23].

The hardware used for the BASS experiments consists of a square cross-section wind tunnel with an internal section of 76 × 76 mm, placed in the Microgravity Science Glovebox onboard the ISS [24]. A schematic of the BASS set-up is given in Fig. 2.5. A sample holder like the one shown in the inset of Fig. 2.5 was mounted on the median plane of the tunnel. A fan on the right side of the tunnel created a forced flow, whose velocity was measured by an omnidirectional spherical air velocity transducer (TSI® 8475). A thermopile detector (Oriel® 71768, spectral range of 0.13 - 11 µm), positioned on the top wall, makes an angle of approximately 20° with the middle of the sample and captures the total radiation from the spreading flame. The radiometer was not calibrated against blackbody emission; nevertheless, its signal can be assumed to be proportional to the total hemispherical radiation received, most of which is controlled by the flame and the burning fuel surface. The time response of the sensor has a delay of a few seconds.

Twenty-two flat samples of PMMA, each about 100 mm long, were tested with flow velocities between 0 and 42 cm/s, oxygen concentration between 15 and 22.2%, sample thickness between 0.1 and 0.4 mm and width of 10 and 20 mm. Pressure is held constant at 101 kPa. The experimental conditions are described by Table A.2. On the left end of the sample, a Kanthal wire was powered for 5 - 10 s to ignite the samples. A Panasonic camera WV-CP654 with a resolution of 760 x 480 pixels recorded the experiments from the side of the duct by using a mirror, while still pictures (4320 × 2968 pixels) from the top of the duct were taken with a Nikon D300s (equipped with a CMOS sensor, 23.6 × 15.8 mm, and a 35 mm $f/2.0$ lens), about every 1 s. Values of the radiometer signal, measured flow velocity, and fan power were superimposed on the experiment videos and could be associated to the flame positions with image analysis.

2.5 Video Processing and Flame Tracking

All the experiments considered in this dissertation were video-recorded in order to track the flame behavior. The need for processing a large number of videos, which progressively increased in quality and size during the years thanks to better cameras, led to the desire and idea of developing a tool that would automatically track a flame. The idea was to create an intuitive tool to obtain fast and reliable results. In this way we could explore different aspects of flames at the same time. Image analysis offered the solution to many of these problems. Due to the broad variety of applications, image analysis has improved significantly over the years, and the amount of information that can be extracted from images and videos has increased

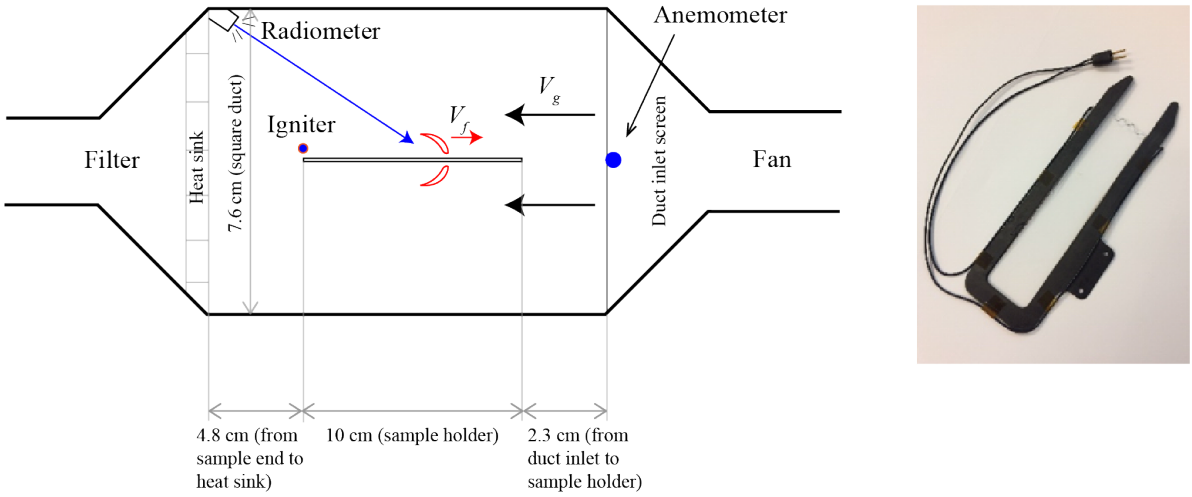

Figure 2.5: Schematic of the experimental set-up used for the BASS investigation (left), and picture of a sample holder (right).

as well. Starting with the intent of calculating the flame spread rate of a flame, the first versions of the Flame Image Analyzer Tool (FIAT) were developed [25, 26]. They were also able to track flame length and area based on different methods. Since the previous versions have been already presented, this section will refer to the new version, which has been created during this work with the intent of improving the tracking methods and make it more user-friendly.

Before illustrating how FIAT works, we will review the principal methods used for flame tracking described in the literature. More details about the software are available for the research community at *flame.sdsu.edu* (along with instructions and video tutorials).

2.5.1 Flame Tracking: Methods Overview

Determining the correct value of flame spread rate in different burning conditions has always been challenging, and many different approaches have been tested and refined in the last fifty years. In the early studies, flames (with velocity lower than about 2.5 mm/s) were tracked with stop-watch-measurements. By using regular marks on fuel samples, the time required by a flame to spread could be tracked [27, 28]. This approach could work only for steady flames that do not accelerate or decelerate during the experiment, and it is not very accurate for very slow flames (that take a long time to cross a mark generating uncertainties) or very fast flames (that can spread between marks too quickly). For more consistent results it seemed necessary to calculate the spread rate using other methods, such as video analysis. During video analysis, the user was required to manually measure the distance covered by the flame on a monitor [27, 29], or on printed pictures [30]. A good alternative to video analysis for relatively fast flames was the use of thermocouples; the thermal

profiles tracked in time were used to find the flame location. In their experiments, Fernandez-Pello et al. used arrays of thermocouples placed at regular intervals normal to the direction of propagation to calculate the flame spread rate [28]. Thermocouples were also used in a similar way for the Solid Surface Combustion Experiments (SSCE) in microgravity [6]. Bhattacharjee et al. [31] tracked flames with thermocouples as well, but in a completely different way: flames spreading downward were rendered stationary with the Flame Stabilizer described in Sec. 2.3.

Even though thermocouples are relatively cheap and reliable, they can make the experimental apparatus very complicated for small scale flames or particular conditions, not to mention the heating interactions with flame and fuel due to the direct contact, with possible consequences on flame spread. An interesting alternative is the use of infrared sensors to obtain temperature profiles, like in the study of Arakawa et al. [32], who measured two-dimensional flame spread rates over vertical solid fuel, showing good agreement with the results obtained with thermocouples. IR cameras can give really accurate temperature profiles of the solid fuel [33], and they are superior compared to the thermocouples because there is no contact with the sample or the flame. However, the flame can interfere with the readings so obtaining good IR images can be challenging. Ito et al. obtained temperatures profiles by using holographic interferometry [34], even though they had to use an additional video camera in order to calculate flame spread rate and pulsation frequency. To overcome the limitations of IR camera and interferometry, Konishi et al. combined the two techniques in the so called infraredholographic interferometry (IR-HI) [35], and they were able to gather temperature profiles and species concentration at the same time. However, this technique requires a special apparatus and high precision systems, whereas video cameras are more accessible. Furthermore, the rapid growth in the last couple of decades of video quality and coding software made video analysis for flame spread rate much easier and faster. The concept of area tracking is used in Spotlight, a piece of software developed by NASA [36], and used by many authors during the last decade [31, 37, 38]. Processing large amounts of videos of experiments can become time-consuming with Spotlight.

Other image analysis tool are available, such as the Java-based ImageJ. Initially developed by NIH, this open-source program has become extremely useful in several fields of image analysis. Despite the advantages of ImageJ, it was desirable to develop a tool in MATLAB since it could better integrate with the experimental apparatuses illustrated in the previous Sections. It is not easy to find many details in the literature, but there are examples of researchers developing their own codes in MATLAB, such as Avinash et al. [39], who mentioned tracking a certain region of the flame for different frames in order to calculate the downward flame spread rate with an accuracy of ± 1 mm/s.

2.5.2 Flame Image Analyzer Tool

FIAT can track several flame characteristics: leading edge position, length, area, and spread rate. By considering for example a still picture of a flame from the BASS experiments (see Fig. 2.6), we can analyze the flame in two ways: (i) intensity tracking and (ii) area or color tracking. With the first method, FIAT transforms the flame image from the RGB to the YCrCb color space, where Y is the luminance intensity and Cr and Cb the chrominance channels, and then averages the Y intensity along the direction perpendicular to the flame, creating a two-dimensional image as in Fig. 2.6b. The part of the image covered by the flame is much brighter than the background, and by choosing appropriate threshold values for the luminance intensity Y, flame leading and trailing edges can be defined as illustrated by the white vertical lines in Fig. 2.6b. We define the flame length as the difference between these two locations. FIAT can also be used to measure the area of a flame with the second method: area tracking. Frames are kept in the RGB color space, and minimum and maximum values (represented in 8-bit, with values from 0 to 255) are chosen for each color channel. By excluding the points outside of the color-channel intervals, specific parts of the flame such as the blue region (Fig. 2.6c) and yellow sooty part (Fig. 2.6d) can be isolated and measured. The area tracking method also provides the flame leading edge and trailing edge positions respectively as the first and last points of the flame region in the spreading direction. By repeating the process for every frame, the evolution in time of flame length and flame area are obtained, as well as flame position and spread rate.

2.5.3 Error Analysis

The video recording of the experiment has two parameters that can be controlled directly by the user before the experiments: the frame rate f, expressed in frames per second (or simply fps), and the spatial resolution p, measured in pixel per mm (indicated as px/mm). Obviously, the higher the values of f and p, the higher is the storage requirement, and, more importantly, the image processing time. In order to find a good trade-off between quality of the video and its relative size, and to achieve a certain time resolution for an eventually unsteady flame spread, it is important to have an understanding of how these parameters affect the time resolution and the error.

Suppose the flame advances through n_p pixels over a span of n_f frames. The spread rate V_f then can be calculated from:

$$V_f = \frac{\Delta x}{\Delta t} = \frac{n_p/p}{n_f/f} = \frac{n_p}{n_f}\frac{f}{p} \tag{2.5}$$

Taking the logarithm of both sides and then the differentials, we obtain:

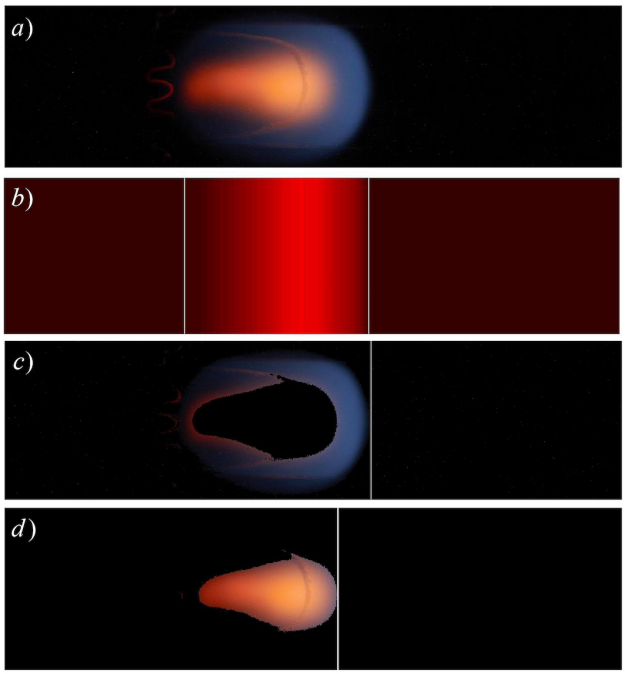

Figure 2.6: Example of FIAT capabilities. Starting from (a) the original flame, the code averages the luminance intensity in the vertical direction and creates (b) a 2D image, where flame leading and trailing edges can be identified. By using color filtering in the RGB space, (c) the blue region or (d) the sooty area of the flame can be measured and tracked.

$$d\left(\ln V_f\right) = d\left[\ln n_p - \ln n_f + \ln\left(f/p\right)\right] \quad \longrightarrow \quad \left|\frac{dV_f}{V_f}\right| = \left|\frac{dn_p}{n_p}\right| + \left|\frac{dn_f}{n_f}\right| \tag{2.6}$$

The left hand side can be interpreted as the measurement error in the computed spread rate, which can be seen to depend on the number of pixels swept by the leading edge during the period of observation Δt. Given that n_p and n_f are integers, we substitute the maximum error as 1. Also, substituting $n_p = pV_f\Delta t$ and $n_f = f\Delta t$, we obtain:

$$\varepsilon = \frac{dV_f}{V_f} = \frac{1}{n_p} + \frac{1}{n_f} = \frac{1}{pV_f\Delta t} + \frac{1}{f\Delta t} = \left(\frac{1}{pV_f} + \frac{1}{f}\right)\frac{1}{\Delta t} \tag{2.7}$$

Clearly, the error can be seen to decrease as the time resolution Δt is increased, which is due to the averaging effect. From this point of view the error in Eq. 2.7 could be interpreted as a sensitivity factor. If a single spread rate is calculated over the entire time span of the experiment by fitting a straight line through the data, there is zero variation in spread rate. For an acceptable error in spread rate of say, 10%, the time resolution can be seen to be a function of frame rate f and the distance pV_f swept by the leading edge per unit time. To minimize the error, f and pV_f should both be large and of the same order. For a relatively fast flame, Eq. 2.7 predicts that frame rate f should be high, whereas for small spread rates, the error is

mostly controlled by p.

For a given value of acceptable error, the time and spatial resolution can be obtained from Eq. 2.7:

$$\Delta t = \left(\frac{1}{pV_f} + \frac{1}{f}\right)\frac{1}{\varepsilon} \qquad \text{and} \quad \Delta x = \Delta t V_f \tag{2.8}$$

The spatial resolution is dependent on the temporal resolution, and a desired spatial resolution can be translated to a desired temporal resolution by knowing the overall flame spread rate. To study an unsteady flame spread to a desired temporal resolution, Δt cannot be arbitrarily reduced since, according to Eq. 2.7, the error bound is inversely proportional to Δt. A reduction in Δt, therefore, must be matched by a reduction in the term in bracket on the right hand side of Eq. 2.7. For example, to capture unsteadiness in spread rate in the order of 20% over a certain time period, Δt must be selected based on the desired time resolution. The imaging system must be designed with the values of f and pV_f sufficiently high to make the error in spread rate much less than 20% to discern uncertainty from the actual unsteadiness.

2.6 The Numerical Model

The computational model consists of a computational fluids dynamics (CFD) model and a radiation model. The CFD code developed by Bhattacharjee's group during the years [40–43], separately solves gas-phase and solid-phase equations with flame spread rate being the eigen-value of the problem. The mathematical flame model consists of the 2D, steady, elliptic, partial differential equations describing conservation of energy, species, mass, and momentum in the gas phase; furthermore, there are ordinary differential equations for conservation of mass and energy in the solid phase. Gas and solid phases are solved sequentially and are coupled by the interface conditions using the SIMPLER algorithm of Patankar [44]. A schematic of the symmetric half of the flame domain is shown in Fig. 2.7, along with the boundary and interface conditions. Given the symmetry of the problem, only one side of the sample is analyzed numerically, while the other half is considered to be a boundary condition along the symmetry axes.

The solution seeks a unique value for the spread rate that anchors the flame leading edge at the desired location, x-eigen, within the computational domain. This is done by requiring the solid absolute temperature to be a certain value (20% above ambient) at the eigen-location. The domain is divided in a non-uniform grid structure. The gas-phase balance equations for total mass, fuel, oxygen, and nitrogen species mass, x- and y-momentum, and energy can be expressed in the canonical form:

$$\frac{\partial}{\partial x}(\rho u \varphi) + \frac{\partial}{\partial y}(\rho v \varphi) = \frac{\partial}{\partial x}\left(\Gamma_\varphi \frac{\partial \varphi}{\partial x}\right) + \frac{\partial}{\partial y}\left(\Gamma_\varphi \frac{\partial \varphi}{\partial y}\right) + \dot{S}'''_\varphi \tag{2.9}$$

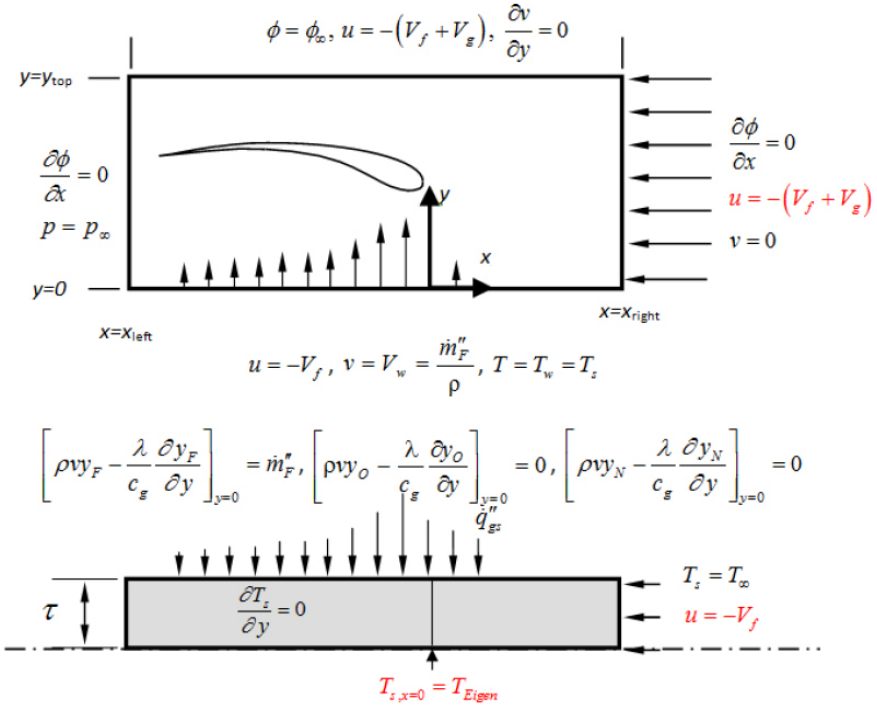

Figure 2.7: Computational domain showing boundary conditions between gas and solid phases.

Where the meaning of each variable is defined in Table 2.1 (more details about the CFD code are available in [43]). For thin fuels, with temperature T remaining constant across the fuel thickness (as it will be explained in Chapter 3), a 1D energy equation in terms of a variable fuel density can be written as:

$$\begin{cases} -\tau \rho_s c_s V_f \cdot dT_s/dx = \dot{m}'''_F \left[\Delta h_c^\circ + (c_g - c_s)(T_s - T_\infty)\right] = \lambda_g \left.\frac{\partial T}{\partial y}\right|_{y=0^+} - \varepsilon_s \sigma T_s^4 \\ \dot{m}'''_F = A_s \rho_s \tau e^{-E_s/(RT_s)} = d(\rho_s \tau V_f)/dx \end{cases} \tag{2.10}$$

The fuel density varies along the pyrolysis region to take into account the vaporization process, and a preset value determines when the fuel is considered completely burnt.

Temperature fields and other properties can be plotted in MATLAB. Without soot modeling, the flame length is determined by using a threshold temperature that defines a boundary for the flame, and by calculating the difference between the minimum and maximum x-coordinates of the flame boundary.

2.6.1 The Radiation Model

Both gas and solid radiation including radiation feedback are included in the model. A constant total emissivity of the fuel surface and the thin-gas approximation in the gas phase are used to simplify the model. However, the Planck mean absorption coefficient a_p is calculated by equating the total emission from

Table 2.1: Meaning of the generic variables in Eq. 2.9.

Equation	φ	Γ_φ	$\dot{S}'''_\varphi$
Continuity	1	0	0
x-momentum	u	μ	$-\partial p/\partial x + \rho g_x$
y-momentum	v	μ	$-\partial p/\partial y + \rho g_y$
Fuel mass	y_F	μ/c_g	$\dot{m}'''_F = -B_g \rho^2 y_O y_F e^{-E_g/(v\overline{RT})}$
Oxygen mass	y_O	μ/c_g	$\dot{m}'''_O = -sB_g \rho^2 y_O y_F e^{-E_g/(v\overline{RT})}$
Nitrogen mass	y_F	μ/c_g	0
Energy	T	μ/c_g	$-\left(\dot{m}'''_F \Delta h_c^\circ + \dot{q}'''_R\right)/c_{p,g}$

a box around the flame using narrow-band radiation solver RADCAL [45] and the thin-gas approximation. RADCAL is also used to solve for the radiative fluxes for each band according to:

$$\dot{q}''_\lambda = \int i_\lambda \cdot d\omega \tag{2.11}$$

The integral of i_λ, which represents the line-of-sight radiation intensity for a given wavelength, over the solid angle $d\Omega$ is evaluated considering the finite width of the flame, therefore including the three-dimensionality of a flame. The radiation solver is separated from the CFD solver and a_p, along with the radiative flux contributions, are updated in a nested iteration scheme. A CPU time on the order of one to several hours is required for convergence. More details about the radiation model are available in Bhattacharjee et al. [46].

Chapter 2, in part, has been published in Fire Technology (L. Carmignani, G. Celniker, S. Bhattacharjee, The effect of boundary layer on blow-off extinction in opposed-flow flame spread over thin cellulose: experiments and a simplified analysis, Fire Technol. 53, pp. 967-982, 2017; L. Carmignani, K. Dong, S. Bhattacharjee, Radiation from flames in a microgravity environment: experimental and numerical investigations, Fire Technol., 2019, in press) and Combustion and Flame (L. Carmignani, S. Bhattacharjee, S. Olson, P. Ferkul, Boundary layer effect on opposed-flow flame spread and flame length over thin polymethyl-methacrylate in microgravity, Combust. Sci. Technol. 190, pp. 534-548, 2018). The thesis author was the primary investigator in these publications. Parts of Chapter 2 have also been published in the Applied Thermal Engineering Journal (G. Lange, L. Carmignani, S. Bhattacharjee, Thermal radiation measurements of downward spreading flames, App. Thermal Engin., 2019, in press) and Fire Safety Journal (S. Bhattacharjee, L. Carmignani, G. Celniker, B. Rhoades, Measurement of instantaneous flame spread rate over solid fuels using image analysis, Fire Saf. J. 91, pp. 123-129, 2017), of which the dissertation author was among the primary contributors in these papers.

Chapter 3

The Thermal Regime

3.1 Introduction

In this Chapter, we consider a specific case of opposed-flow velocity, the buoyant flow created by a flame burning in atmospheric conditions. Specifically, we analyze flames spreading vertically along a solid fuel (from top to bottom), and we refer to this problem as downward flame spread. For PMMA, the buoyant flow is fast enough to guarantee a stable flame (the opposing flow velocity is not too small or too large so that neither radiation nor chemistry play any significant role in the mechanism of flame spread).

A flame spreading downward along a solid fuel behaves in a quasi-steady, quasi-laminar manner (the flame trailing edge may show fluctuating patterns) with a constant flame spread rate. Since the burning conditions are the ones at sea level, this configuration can be easily reproduced to study the influence of solid fuel parameters on flame spread. The variation of fuel thickness, for example, can affect the flame characteristics. The effect of fuel thickness on flame spread rate has been largely studied in the literature, and it can be used as a baseline for the other flame characteristics.

3.2 Flame Spread Rate

3.2.1 A Closed-Form Solution: de Ris' Spread Rate

An analytical solution of the governing equations of the problem is possible by neglecting radiation and assuming infinite-rate kinetics. The closed-form solution obtained by de Ris and Delichatsios for flame spread rate in the thermal regime provides a baseline for experimental results, and helps understanding the dependence of flame spread on fuel and environmental parameters [47, 48]. According to de Ris, flame spread rates can be divided in two categories based on fuel thickness: thin and thick. For thin fuels, the

inner temperature is uniformly distributed along the cross section, while thick fuels experience a temperature gradient across their thickness. The expressions for flame spread rate in the two regimes proposed by de Ris, and refined by Delichatsios, are:

$$V_{f,\text{thn}} = \frac{\pi}{4}\frac{\lambda_g}{\rho_s \tau c_s} \cdot F \tag{3.1}$$

$$V_{f,\text{thk}} = V_g \frac{\lambda_g \rho_g c_g}{\lambda_s \rho_s c_s} \cdot F^2 \tag{3.2}$$

The term $F = (T_f - T_v)/(T_v - T_\infty)$ depends on the concentrations of fuel and oxidizer. The value of F is not unique in literature, varying between 4.4 and 5.5, but experimental data for thin fuels in both normal gravity and microgravity show good agreement with Eq. 3.1 when $F = 4.76$ [49]. It is interesting to notice that the thin fuel formula is independent on the flow velocity V_g, which makes it suitable to calculate the coefficient F, and the product $V_f \cdot \tau$ only depends on thermodynamic properties. The spread rate for thick fuels is independent of τ, but increases with the flow velocity V_g. Figure 3.1 shows the previously published experimental flame spread rates over PMMA samples over several thicknesses by Fernandez-Pello and Williams [15], NASA and Lastrina et al. [29], as well as data from our laboratory [49, 50]. To match the experimental values for thick fuels, the opposing velocity in downward flame spread facing the flame front is found to be about 2 cm/s (the velocity of buoyancy-induced flow at the leading edge), in agreement with the velocity measured through interferometry near the leading edge of a PMMA flame by Fernandez-Pello and Williams [51]. It is clear that Eq. 3.1 and 3.2, indicated in Fig. 3.1 respectively by the red and blue dashed lines, are in good agreement with the experimental data and well describe the fundamental physics of two-dimensional flames, although there are other formulations by different authors [12]. Given their simplicity, Eq. 3.1 and 3.2 have been widely used to normalize flame spread rate to develop new correlations away from the thermal regime such as the kinetic or the radiative regimes [52].

These well-known formulae for opposed-flow flame spread, however, have some drawbacks. The flame temperature included in F is based on a linearized mass diffusion theory and can be quite different than the thermodynamic adiabatic flame temperature, and the temperature in the pyrolysis region, which is used to characterize the fuel gasification process, is assumed constant. Also, use of constant properties in the theory allows room for significant variability in how properties such as the thermal conductivity of air, specific heat, etc. are evaluated. As a result, when an experimental spread rate does not agree reasonably well with the theoretical prediction, it is not clear whether the disagreement is due to incorrect use of properties in the formula or due to more fundamental reason such as the flame spread being not in the thermal regime.

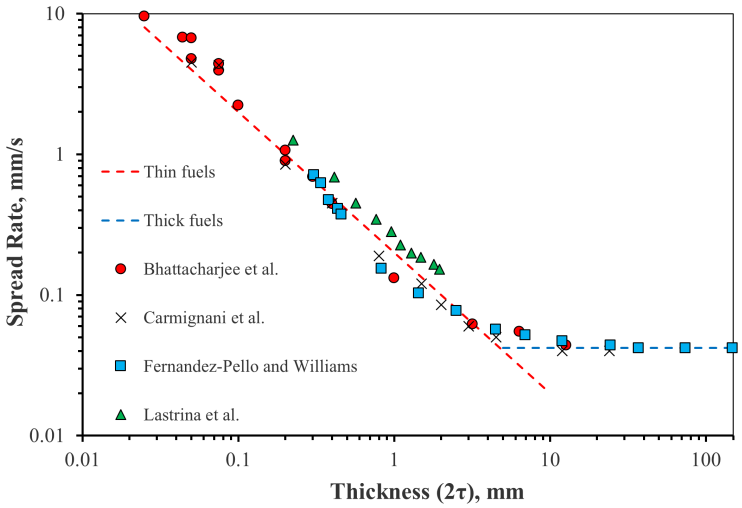

Figure 3.1: Downward flame spread rate variation with fuel thickness; experimental data from Lastrina et al. [29] and our recent work on thick fuels (from [50] and described in Sec. 3.3.2) are added to previously published data [49], which already included results from Fernandez-Pello and Williams [15].

3.2.2 Influence of Fuel Geometry on Downward Flame Spread

Theoretical solutions of two-dimensional flames are fundamental in the understanding of flame spread, but often are not directly applicable to realistic scenarios. Yet, they can represent a baseline to isolate the effect of the third dimension in a flame over a more realistic geometry.

Experimentally, two-dimensional flames can be obtained using samples that are wide enough for the central part of a flame not to be affected by the sides of a burning sample. A more practical solution is to inhibit the lateral flames, as shown on the left of Fig. 3.2. In this case the flame front tends to proceed uniformly along the sample, in contrast with the typical reversed "V" shape of the flame affected by the edges (see right flame of Fig. 3.2). According to Fig. 3.2, flames propagating along the sample edges will be called edge flames and the flames along the center of each surface will be called central flames, for the lack of standard terminology.

The presence of edge flames causes the global flame to spread faster with respect to the inhibited case. However, flame spread rates may vary depending on geometry and size of the fuel, such as cross-sectional shape and aspect ratio of the sample (ratio between width and thickness), making it harder to identify a single spread rate. The influence of lateral flames over rectangular prisms of PMMA was first investigated by Markstein and de Ris [53], who found an empirical relation between spread rate and angle formed by the pyrolysis region with the vertical axis on the sample sides. This angle assumes a constant value of about 30° according to the experimental work of Creeden and Sibulkin [54]. This angle became the link for edge studies between downward and horizontal spread, which started with Emmons and Shen for paper arrays

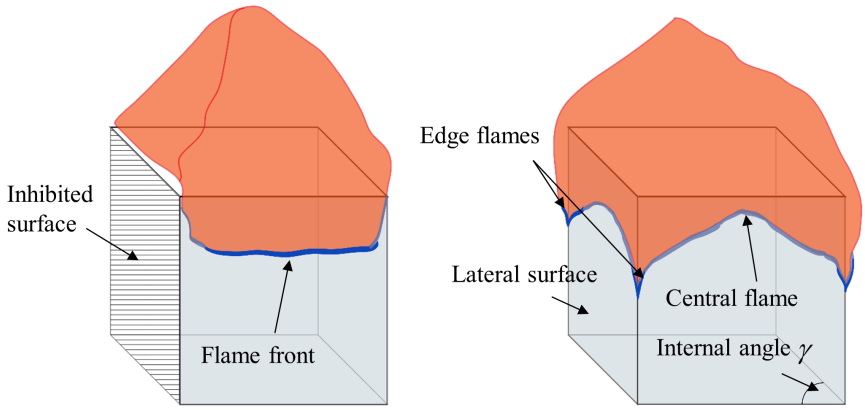

Figure 3.2: Schematic representation of a flame burning over a flat surface without the influence of edges (*left*), and with the unrestrained combustion of the lateral surfaces (*right*).

[55], and continued with other investigators comparing results also from microgravity [56, 57], albeit the edges were mostly considered for ignition and transient phenomena. The microgravity environment, as well as the downward configuration, was also considered in the computational study of Kumar and Kumar [58], who quantified the spread rate with and without side burning over thin fuels. They justified the increase in the unrestrained configuration with a higher temperature of the burning solid and a rise of oxygen supply, as discussed also in the experimental study of Comas and Pujol [59]. These recent studies focused on thin fuels, so the edge-effect is considered more as a secondary effect of a finite geometry rather than an enhancing phenomenon due to the three-dimensionality of the problem. Gong et al. recently developed a model for downward spread over PMMA slabs based on their experiments [60]. They concluded that the enhanced heat transfer from the side flame and higher oxygen supply are responsible of the higher flame spread rate, in analogy with the previous works [58, 59].

In parallel to the work on flat solid fuels, the influence of fuel geometry on spread rate was investigated for cylindrical samples. This geometry is very important for fire safety as the configuration relates to propagation along cables and pipes, as well as trunks or pillars. Fernandez-Pello and Santoro investigated the heat transfer mechanisms along rods [61], concluding that either solid or gas-phase conduction become more dominant based on the rod diameter (when the fuel is thicker or thinner, respectively), in analogy with other fuel geometries [29]. However, the distinction between thick and thin fuel rods can be complicated as discussed in the energy analysis of Sibulkin and Lee [62]. Differences and similarities of flat and cylindrical fuels were studied by Delichatsios et al. using both experimental and numerical results (including microgravity) [63]. The spread rate expression is derived from an energy balance and assumptions in analogy with the flat geometry, corrected with two factors related to the effects of curvature in the solid phase and greater

heat transfer in the gas phase.

It is well known that flames over fuel samples with edges are faster than those over cylindrical samples (with similar values of τ and radius r), which in turn are faster than over flat fuel samples, but there are no predictive formulae that quantify these geometrical effects. With a comprehensive experimental study we explore the role played by faster edge flames in three-dimensional PMMA samples, and their influence on the overall flame spread rate. The objective is to correlate the spread rate of three-dimensional flames to established equations for downward spread rate over flat fuel samples (two-dimensional geometry).

3.2.3 Experimental Results: Sample Edges

All the samples of cast PMMA were burnt in a downward configuration, held from the bottom and kept vertical with a vice fixed to the structure of the Flame Stabilizer. To provide enough air entrance, the vice was mounted at a height of about 1 m from the floor, and the samples were 10 - 15 cm long. The top surface of the samples was manually ignited with a blowtorch flame; thinner fuels took only a few seconds to develop a self-sustained flame, while thicker ones needed a longer amount of time (30 - 50 s). By igniting the top surface, the initial location of edge flames was slightly affected, but not the spread rate or repeatability of the results.

Samples with multiple types of cross-sections were prepared starting from cast PMMA rods. The smaller samples were obtained manually with a belt sander machine, whereas a CNC milling machine was used for the bigger ones. The sample cross-sections presented small irregularities due to the machining process, so in this section we report all the data points obtained instead of average values from repetitions of the same experiment.

Figure 3.3 shows the flame over a sample with rectangular cross-section of 30 $\times$ 12 mm (the smaller dimension is considered the thickness of the sample) and the spread rate tracked at three different locations of the flame front (the two edges and the central region). The error in the instantaneous spread rate was limited to less than 5% (see Sec. 2.5.3 or ref. [64] for the error analysis). As soon as the flame is established, the spread begins down all the four edges (even though only the two visible ones are tracked), and the plot in Fig. 3.3 shows that edge flames spread at an almost constant rate from the very moment of ignition through the entire duration of the experiment, similar to what Zhao et al. observed [65]. The central flame, on the other hand, develops slower, accelerates, and eventually catches up with the edge flames (after about 400 s). A steady state is reached when the inverted V shaped flame front (see Fig. 3.3) propagates at a constant spread rate. In this specific case, the steady-state flame spread rate is found to be 0.11 mm/s, which is more than twice the initial rate of 0.05 mm/s of the central flame. Without the edges, the initial rate of the central flame corresponds to the 2D limit for the sample with same thickness as shown from the data of Fig. 3.1.

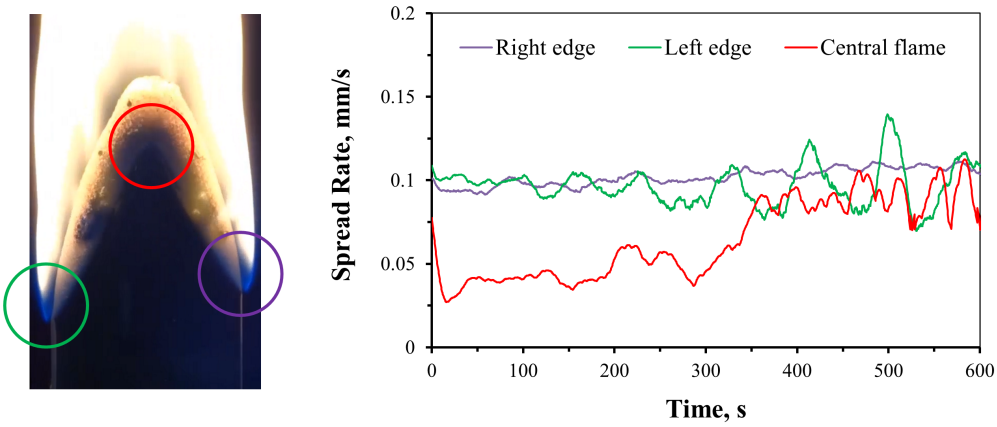

Figure 3.3: Samples with rectangular cross sections burn faster at the edges, creating the typical reversed V shape of the pyrolysis region as shown on the left. The three points of the flame indicated by the colored circles are tracked during time to determine their spread rates.

To explore if the sample width is responsible for this behavior, experiments were conducted with samples of different widths and same thickness. The resulting spread rates are plotted against the aspect ratio (width divided by the thickness $T = 2\tau$) in Fig. 3.4, although the thickness was held constant at the same value ($T = 12$ mm) as the sample in Fig. 3.3 (its average spread rate is indicated by the dashed line). The spread rate variation seems to be random in nature, showing no definitive effect of width. Previous studies had the same conclusion showing that width variations in rectangular prisms can affect the shape of the flame front [60, 66], while the spread rate remains almost constant (the central flame spread rate tends to approach the two-dimensional limit for large values of sample width).

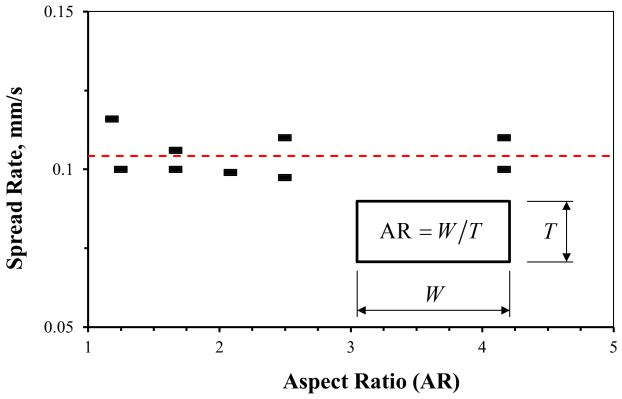

Figure 3.4: The dashed line represents the average spread rate in steady-state over a 12 × 30 mm rectangular sample and is compared with different aspect ratios obtained by 12 mm thick samples.

Another possible factor influencing the edge flames spread is the area of the cross-section; experiments were repeated using triangular prisms with different cross-sectional areas but equal internal angles of 60°. The observed flames behaved very similarly to the ones over rectangular prisms described by Fig. 3.3,

where the edge flames spread at a faster, constant rate and the central flame eventually catches up. The spread rates for multiple values of cross-sectional areas, plotted in Fig. 3.5, have an average value of 0.19 mm/s (shown by the dashed line), which is larger than the baseline case of rectangular sample (0.11 mm/s) of Fig. 3.4. Given the evidence that aspect ratio and cross-sectional area do not play any major role, we hypothesize that the internal angle at the edge (90° for a rectangular sample, 60° for triangular samples) is responsible for the faster flames: the smaller the angle, the higher the spread rate.

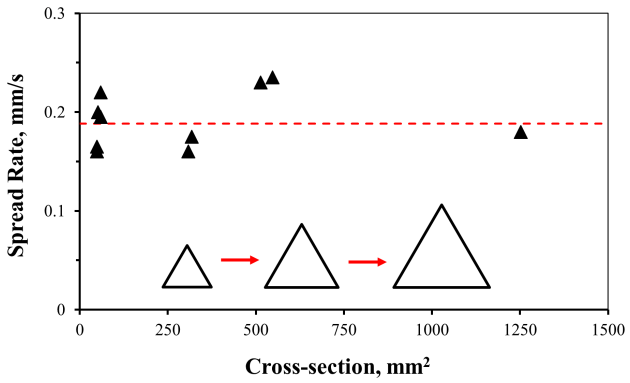

Figure 3.5: Experimental flame spread values for similar triangles with different values of cross-sectional area. The difference in spread rates for increasing areas is not statistically significant.

To test this hypothesis, multiple samples were prepared with a wide variety of regular cross-sectional shapes (triangle, square, hexagon, octagon, etc.), and the average spread rates for each edge flame tracked (corresponding to the internal angles measured before the experiment with image analysis) are plotted in Fig. 3.6. Circular cross sections can be treated as composed by an infinite number of edges with internal angles of 180°. To achieve internal angles different from the ones of regular geometries, samples with irregular cross-sections were prepared, such as triangular or trapezoidal. For irregular samples, different spread rates were maintained along different edges and a steady state was never obtained in the duration of any experiment (as illustrated in the right picture of Fig. 3.6, the flames were at much different locations over the different edges). Data from the irregular samples in Fig. 3.6 can be seen to continue along the trend of an increasing spread rate with a reduction in the internal angle. On the other hand, higher values of the internal angle (including cylindrical cross-sections) have spread rates closer to the 2D value of Eq. 3.2 indicated by dashed line, suggesting that circular cross-sections can be alternatively considered edge-less just like flat surfaces.

The variation of spread rate with thickness and radius for rectangular and circular cross sections is also included in Fig. 3.6, but since they share the same value of internal angle they just displace vertically, with the thicker fuels having the lower values. Although the results establish the internal angle as a dominant parameter, an effective correlation must develop a connection between the internal angle and an equivalent flat sample for which closed-form formulae are available, including the dependence on thickness. The dual

definition of the circular cross section as edge-less or with an infinite number of edges suggests a connection between cylinders and flat samples or cylinders and samples with edges, while the thickness dependence is maintained (thinner cylinders have higher spread rates). Starting from cylindrical and flat fuel spread rates, we can develop a correlation to convert an edge propagation to the cylindrical case by defining an effective diameter (related to the internal angle of the edge).

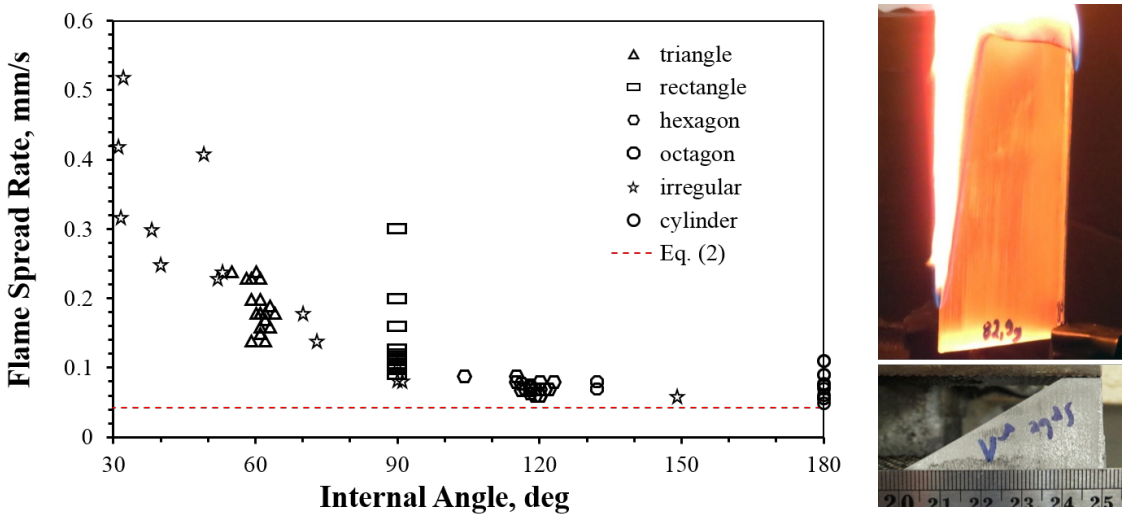

Figure 3.6: Variation of flame spread rate with the internal angle between two adjacent surfaces. On the right there is an example of irregular cross-section with one sharp angle (30°) and one of 90°. The flame over the sharp edge is much faster than the other one, and the central flames could not reach steady-state before the end of the experiment.

3.2.4 Connecting Different Geometries: the Effective Radius

The works of Higuera and Linan [67] and Delichatsios et al. [63] prove that flame spread rate over cylinders is higher than for two-dimensional flat fuels with comparable thickness for two main reasons: (i) enhanced heat transfer between flame and fuel due to curvature, (ii) and the temperature in the solid rises faster because of less material per unit length along the curved surface. These two effects can be expressed by two separate factors, that we indicate respectively with f_{HT} (heat transfer factor), and f_{C} (curvature factor). Delichatsios et al. define these two terms as [63]:

$$f_{\mathrm{HT}} = \frac{c \cdot L_g/r}{\ln\left(1 + c \cdot L_g/r\right)} \tag{3.3}$$

$$f_{\mathrm{C}} = \left(1 - \frac{\tau_h}{2r}\right)^{-1} \tag{3.4}$$

Where r is the cylinder radius and c is a constant that takes into account the particular configuration (natural or forced flow, microgravity conditions, etc.); in this work we consider $c = 1$ for simplicity, since the value for downward spread rate was found to be 1.8 [63]. The factor f_{HT} is derived assuming an Oseen flow with a uniform velocity profile and constant properties, whereas f_{C} follows from the geometry of the heated layer in a circular cross-section. For thin fuels the heated layer is equal to the entire radius ($\tau_h = r$), therefore $f_{\mathrm{C}} = 2$, whereas for thick fuels we can define τ_h from the balance of heat conduction calculated on the solid surface (between gas and solid phases):

$$\lambda_s \frac{T_v - T_\infty}{\tau_h} = \lambda_g \frac{T_f - T_v}{L_g} \qquad \longrightarrow \qquad \tau_h = \frac{\lambda_s}{\lambda_g} \frac{L_g}{F} \tag{3.5}$$

Writing the spread rate over cylinders as $V_{f,\mathrm{cyl}} = V_{f,\mathrm{flat}} \cdot f_{\mathrm{HT}} \cdot f_{\mathrm{C}}$, with $V_{f,\mathrm{flat}}$ given by Eq. 3.1 and 3.2 respectively for thin and thick fuels, and assuming $\tau = r$ we obtain:

$$V_{f,\mathrm{cyl,thn}} = \frac{\pi}{2} \frac{L_g}{r \ln\left(1 + L_g/r\right)} \frac{\lambda_g}{\rho_s c_s r} \cdot F \tag{3.6}$$

$$V_{f,\mathrm{cyl,thk}} = \left(1 - \frac{\tau_h}{2r}\right)^{-1} \frac{L_g}{r \ln\left(1 + L_g/r\right)} V_g \frac{\lambda_g \rho_g c_g}{\lambda_s \rho_s c_s} \cdot F^2 \tag{3.7}$$

The curvature can be seen to have a stronger effect on spread rate for thin cylinders than thick ones, and in the limit for $r \to \infty$ the two-dimensional limit $V_{f,\mathrm{cyl}} = V_{f,\mathrm{flat}}$ is satisfied.

Because of the ease of use of Eq. 3.6 and 3.7 and the advantages of a circular cross section mentioned before, it is worth connecting the edge propagation illustrated in Fig. 3.6 to the cylindrical flame spread rate. To develop an expression for an effective diameter starting from the internal angle, we observe that a sharp edge makes the effective thickness of the fuel smaller near the edge compared to a blunt edge. We propose an effective radius for a given internal angle as the semi-distance between two adjacent sides at a depth from the edge apex chosen between τ_h (thermal penetration distance) and the half of the sample side length l, as illustrated in Fig. 3.7 and expressed by:

$$L_d = \min\left(\tau_h, l/2\right) \qquad \longrightarrow \qquad r_{\mathrm{eff}} = L_d \tan\left(\gamma/2\right) \tag{3.8}$$

The value of τ_h can be derived from Eq. 3.5 using the known values of thermal conductivity (see Table A.1), and temperature ratio $F = 4.76$ [49], obtaining $\tau_h \sim L_g$. The diffusion length L_g scales with the thermal diffusivity $\alpha_g = \lambda_g / \left(\rho_g c_g\right)$, and the flow velocity V_g, in which downward flame spread assumes a value of about 2 cm/s [49, 51], so $\tau_h \sim L_g \sim \alpha_g / V_g \approx 4$ mm. Knowing the value of τ_h, it is straight forward to determine the length L_d, so the effective radius can be calculated trigonometrically (see Eq. 3.8). This

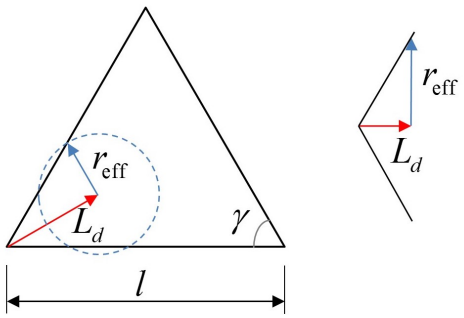

Figure 3.7: After defining L_d as the minimum between thermal length and half-length of the sample side, the effective radius is calculated trigonometrically.

definition of the effective radius combines the complex geometric effects of edges into a single variable. Note that a single sample with an irregular cross-section will present multiple effective radii depending on the internal angle, or equivalently on the edge.

Figure 3.8 shows the predicted flame spread rates for cylinders described by Eq. 3.6 and 3.7, as well as the experimental data of Fig. 3.6 as a function of the effective radius. Note how the experimental data are well captured by the thin and thick limits of the cylindrical formula; the spread of some of the data between the thin and thick limits suggests that the effective semi-thickness (radius) of the fuel is in an intermediate regime, in analogy with the two-dimensional spread in Fig. 3.1. A higher effective radius produces a smaller spread rate, reducing the fire spread danger. Besides the thickness of the fuel, the presence of an edge significantly affects its effective radius and thus its inherent fire danger. Predicted and measured spread rates for five different cross-sections are shown in the inset of Fig. 3.8 in the order of fire danger (the reported values are from the thick regime, where $L_d = \tau_h$), showing that the spread rate over a triangular fuel is about 5 times higher than the corresponding one over a flat sample. Equations 3.6 and 3.7 with the effective radius obtained from Eq. 3.8 could be used to estimate the spread rate of flames along realistic geometries.

3.3 Mass Burning Rate

3.3.1 A Coupled Problem

Emmons [68] obtained a closed-form solution for burning rates over liquid fuels (which applies also to horizontal flat solid fuels), showing their dependence on wall shear stress and flow velocity using the B-number. This number, introduced by Spalding [69] for droplet combustion (it is also called Spalding mass transfer number), depends on fuel properties and governs mass transfer. There are some discrepancies in

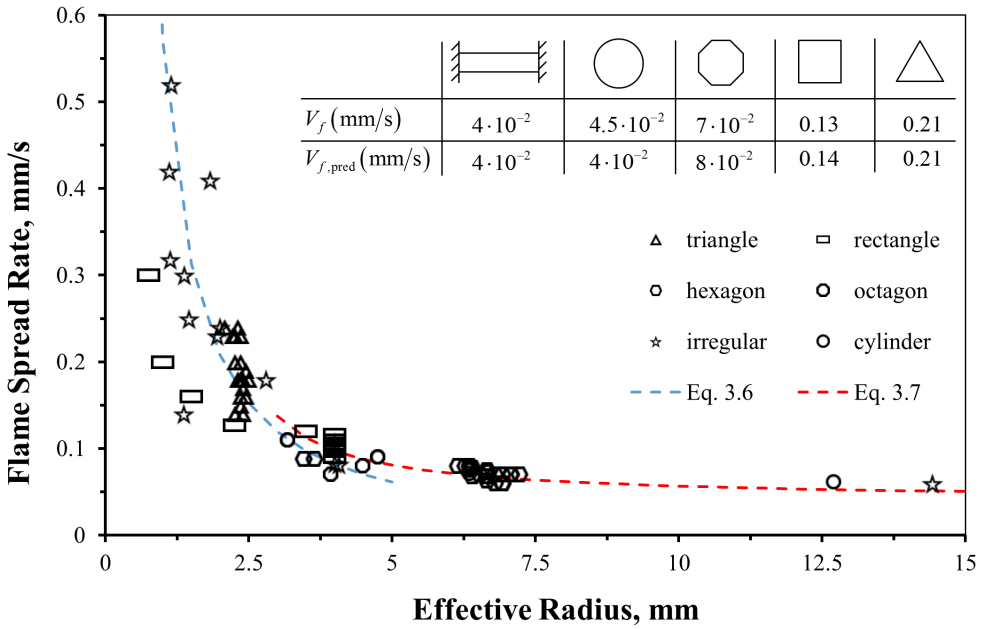

V_f (mm/s)	$4 \cdot 10^{-2}$	$4.5 \cdot 10^{-2}$	$7 \cdot 10^{-2}$	0.13	0.21
$V_{f,\text{pred}}$ (mm/s)	$4 \cdot 10^{-2}$	$4 \cdot 10^{-2}$	$8 \cdot 10^{-2}$	0.14	0.21

Figure 3.8: Flame spread rate predicted by Eq. 3.6 and 3.7 and measured over different sample geometries are correlated using the effective radius determined by the internal angles and Eq. 3.8. The top table shows values of measured and predicted spread rates in the thick regime, in increasing order.

estimated values of the B-number for PMMA due to heat losses approximations, varying from 1.3 to 1.8 [70]. The B-number is generally assumed constant for a given problem, although Rangwala [70], following the work of Torero et al. [71], proposed a time-dependent B-number based on the flame stand-off distance for upward flame spread to explain the differences between experimental and theoretical results.

Emmons closed-form solution has been extensively explored by several researchers. Sibulkin et al. [72] studied the effect of finite chemical reaction rates on flames burning over vertical fuels in buoyancy-driven flows, whereas the influence of a forced flow was described by Zhou and Fernandez-Pello [73], who confirmed Emmons' prediction of a decreasing burning rate with distance downstream of the flame leading edge. A detailed spatial distribution of the burning rate was given by Ananth et al. [74] for PMMA burning against a forced flow, revisiting the approximations adopted by the boundary layer theory. Time-dependent and local mass burning rate have been effectively measured in the past, from the vertical walls of Orloff et al. [75] to more recent experiments. Pizzo et al. found that the mass burning rate over a vertical wall decreases with distance from the leading edge with a power law: $x^{-0.37}$ [76] (since flames cover the entire fuel surface the coordinate x is positive along the pyrolysis region). A similar configuration was used by Singh and Gollner [77], who found an almost identical decrease ($x^{-0.35}$) in a naturally driven flow by extending the Chilton-Colburn analogy and measuring the temperature gradients. The same authors found a similar decrease in the case of forced-flow [78]. Local heat fluxes and burning rates in different configurations are

available in literature [79–81], but it should be noticed that the fuel surface profile varies in time because the mass burning rate is not uniform. Therefore, the correlation between $\dot{m}''$ and x may vary in time [82].

Emmons' solution stimulated research on burning rates of non-spreading flames as the ones mentioned above, but there are studies that consider upward flame spread as well [75, 83]. The influence of a forced concurrent flow (same direction of flame spread) on horizontal flame spread and burning rates for PMMA and wood samples was studied by Mekki et al. in a wind tunnel [83], whereas attempts to characterize the analogous problem with opposed-flow or simply downward flame spread are rare.

Flame spread rate is driven by the heat transferred to the virgin fuel ahead of the flame, while the mass burning rate is associated with the fuel region covered by the flame. Due to the distinct nature of these phenomena and their different response to ambient conditions such as flow velocity [84], or orientation respect to gravity [62], it is not surprising to find a limited number of studies analyzing the coupled problem, despite the extensive volume of work in each area. Furthermore, most flame spread investigations in literature focus on thin fuels, whereas burning rate studies typically examine flames over thick fuels for practical reasons.

The mass burning rate is also related to the regression of the fuel surface, so it can be indirectly estimated from the study of the fuel pyrolysis region. In the experiments of Sibulkin and Lee on flame spread over PMMA cylinders with different orientations with respect to gravity, the pyrolysis region presented a conical shape [62]. The regression rate, related to the mass burning rate by $\dot{r} = \dot{m}/\left(\rho_s L_p W\right)$ (where W is the width of the sample and $L_p \cdot W$ is the area of the pyrolysis region), was calculated from the geometry of the pyrolysis zone relating the angle of the pyrolysis cone (cone angle) and flame spread rate. A few years later, Sibulkin and Little [85] noticed that oxygen concentration affected the cone angle and spread rate. At low oxygen levels flames were not able to spread, but the conical region kept burning shortening the pyrolysis region and increasing the cone angle. A similar behavior was observed by Fernandez-Pello and Santoro [61].

Experiments suggest that the cone angle represents the competition between flame spread and mass burning rates, which are differently affected by the ambient conditions. When a flame cannot spread but still burns (often labelled as regressing flame) the pyrolysis region starts shrinking. A critical cone angle of 45° has been proposed by Huang et al. [86] for the transition between spreading and regressing flames, based on flame spread experiments over PMMA cylinders varying opposed flow velocity, pressure and gravity level.

Flat fuels, like cylindrical fuels, present a declined pyrolysis region, as shown in the work of Ayani et al. [87]. They measured the angle at the vertex of the pyrolysis region of flat slabs of PMMA (with thickness varying from 1.5 to 10 mm) and assumed it constant in their heat transfer model.

3.3.2 Experimental Results: the *Burn Angle*

Thin samples (thickness from 0.05 to 1.5 mm) were tested in the Flame Stabilizer (see Sec. 2.3), while the thicker samples (up to 24 mm) where burnt between ceramic plates attached to a vice mounted on the structure of the Flame Stabilizer (same set-up used for the experiments described in the previous section, but with samples burning between the plates to inhibit the later surfaces as indicated in Fig. 3.2).

The width of the thin samples is 30 mm, which was increased to 50 mm for thicker samples ($2\tau > 2$ mm) to guarantee enough air entrance between the plates. Experiments were repeated at least twice in order to obtain consistent results. Due to the faster nature of flames over thin fuels, thinner samples were longer (up to 40 cm long) than the thicker ones (about 10 cm long). The time required for a flame to reach steady state (pyrolysis region, flame height and spread rate not changing in time) depends on fuel thickness. Thin fuels need only a few seconds, whereas thicker samples require up to 10 - 15 minutes.

After the desired amount of time of steady-state flame spread, the pyrolysis region can be measured by quickly extinguishing the flames to preserve shape and size of the burning region, which was maintained in position until it cooled off and the molten layer solidified. The pyrolysis region is clearly visible in PMMA samples by the dark particles covering the surface as shown in Fig. 3.9 for a 2 mm thick sample. From the front view it is not possible to notice whether the pyrolysis area is declined with respect to the surface, therefore burnt samples were cut along their centerlines (A-A in Fig. 3.9). The triangular shape of the pyrolysis section clearly shows the angle with respect to the fresh fuel. We refer to the complimentary angles as regression angle α and *burn angle* β (indicated in Fig. 3.9). The burn angle corresponds to the cone angle of the cylindrical samples, and it geometrically relates semi-thickness τ and pyrolysis region length L_p:

$$\sin\beta = \tau / L_p \tag{3.9}$$

According to this definition, burn angles can be obtained in two ways: (i) from image analysis, directly measuring the complimentary regression angle α (measurements of β could lead to mistakes because of the rounded shape of the pyrolysis region vertex), or (ii) deduced from Eq. 3.9 by knowing τ and L_p.

For fuel thicknesses above 1.5 mm, a Canon® PowerShot SX720 HS has enough resolution to distinguish the pyrolysis region contour and the angle α, but for thinner fuels a microscope was required. Specifically, the Keyence VHX-600 digital microscope was used with the wide-range zoom lens VH-Z100R (100× to 1000×).

One of the advantages of the downward configuration is that the flame spread rate is constant throughout the entire length of the experiments. The only exceptions are the initial transient (not considered here), and a slight increase in spread rate (less than 10%) over a long time (more than 10 min) for $2\tau = 25$

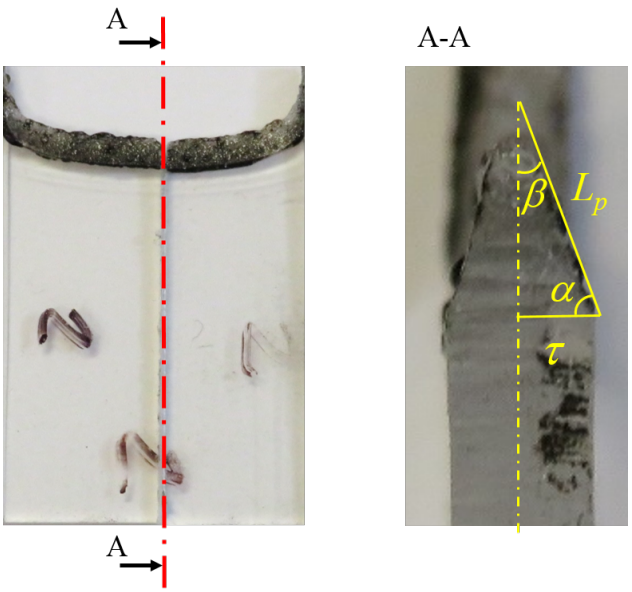

Figure 3.9: PMMA sample with thickness of 2 mm after the experiment (left). The sample is cut along the centerline A-A to measure the burn angle β, which is indicated in an enlargement of the pyrolysis section (right). The cut out shows the typical triangular shape.

mm, probably due to the influence of the hot ceramic plates that progressively heat up the sample.

Direct measurements of mass burning rates for flames spreading on both sides of a vertical flat plate can drastically increase the complexity of the experimental set-up. Measurement of instantaneous mass fluxes can also become difficult because of the fast-moving nature of a flame (up to 4.5 mm/s for $2\tau = 0.05$ mm) and the relatively high measurement error due to the sample weight being low (increasing the required accuracy of a scale). In this work, the average mass flux is obtained measuring the sample mass (with scale resolution of ± 0.01 g) before and after an experiment and dividing this difference by the time of flame spread and the area of the pyrolysis surface. A similar procedure was used by Krishnamurthy and Williams [81], and the average mass flux expression is:

$$\overline{\dot{m}}''_{\text{exp}} = \frac{m_f - m_i}{\Delta t \, (2 L_p W)} \tag{3.10}$$

where m_f, m_i are respectively final and initial mass of the sample, Δt is the time of spread, and W is the sample width.

It is well known that the pyrolysis region of spreading flames tends to increase with fuel thickness. On the other hand, from Fig. 3.1 we can see that the flame spread rate decreases with thickness until it reaches an asymptotic limit. Since the burn angle represents the competition between mass burning rate and flame spread rate and it is geometrically related to the pyrolysis region, it comes natural to question

whether the burn angle changes with fuel thickness. Four different PMMA thicknesses, from 1.5 mm to 25 mm, are shown on the left of Fig. 3.10; the pyrolysis zone can be easily identified by the brown region of fuel for each of these samples (indicated by the red dashed boxes). The pyrolysis length L_p is indicated by the red arrow and it is calculated along the centerline of the samples to be consistent with the burn angle measurements. The pyrolysis region does not change once the flame reaches steady state, and according to the experimental data reported on the right of Fig. 3.10 its length L_p increases almost linearly with fuel thickness.

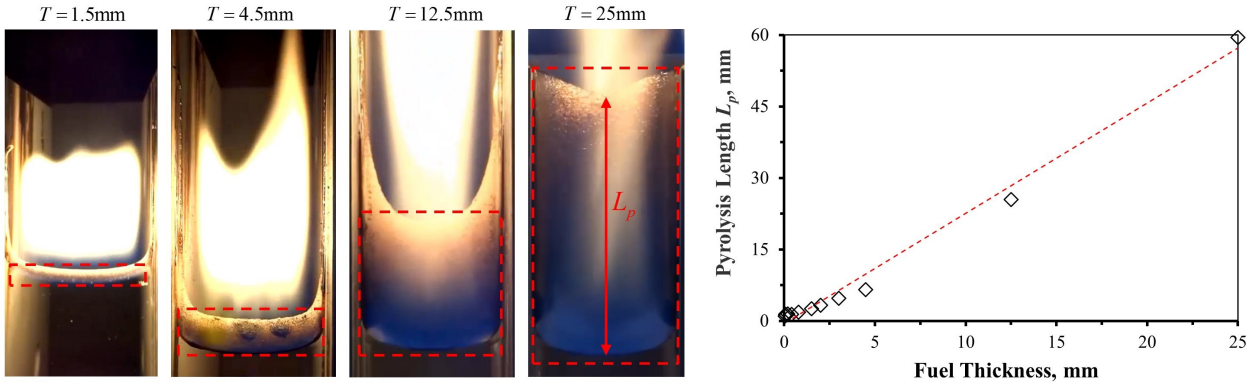

Figure 3.10: Downward spreading flames over PMMA slabs of different thicknesses, with the pyrolysis regions highlighted by the red dashed boxes. The pyrolysis length L_p (calculated along the sample centerline), increases almost linearly with the sample thickness, as shown in the graph.

The burn angles of samples with thickness between 0.4 mm and 25 mm are shown in Fig. 3.11, where the sample contour is highlighted by the red-dashed line. Similar pictures for PMMA samples between 1.5 and 10 mm can be found in the work of Ayani et al. [87]. Pyrolysis regions maintain a triangular shape decreasing fuel thickness until a value of 0.8 mm, whereas samples with thickness equal or below 0.4 mm show a curved profile. Figure 3.11 suggests that the burn angle changes with thickness.

The burning surface of PMMA has a soft consistency, and pyrolysis regions seem to collapse under the effect of gravity for fuel thicknesses below 0.4 mm. This could be the reason why samples with thickness between 0.05 and 0.4 mm all have a similar length of pyrolysis region of about 1.3 mm (see Fig. 3.10). To evaluate if the pyrolysis region is thickness dependent for $2\tau < 0.4$ mm, samples from the microgravity experiments were considered. Four samples were selected from the BASS investigation with thicknesses ranging from 0.1 to 0.4 mm and similar testing conditions (refer to Table A.2). The length of their pyrolysis region was measured with FIAT from the pictures taken at the end of the experiments, which are illustrated in Fig. 3.12 along with the measured L_p. Even though these values are not directly comparable with the downward experiments from Fig. 3.11, it is clear that L_p increases with sample thickness, from a value of about 2 mm for $2\tau = 0.1$ mm to 20 mm for $2\tau = 0.4$ mm. These results suggest that the pyrolysis region in

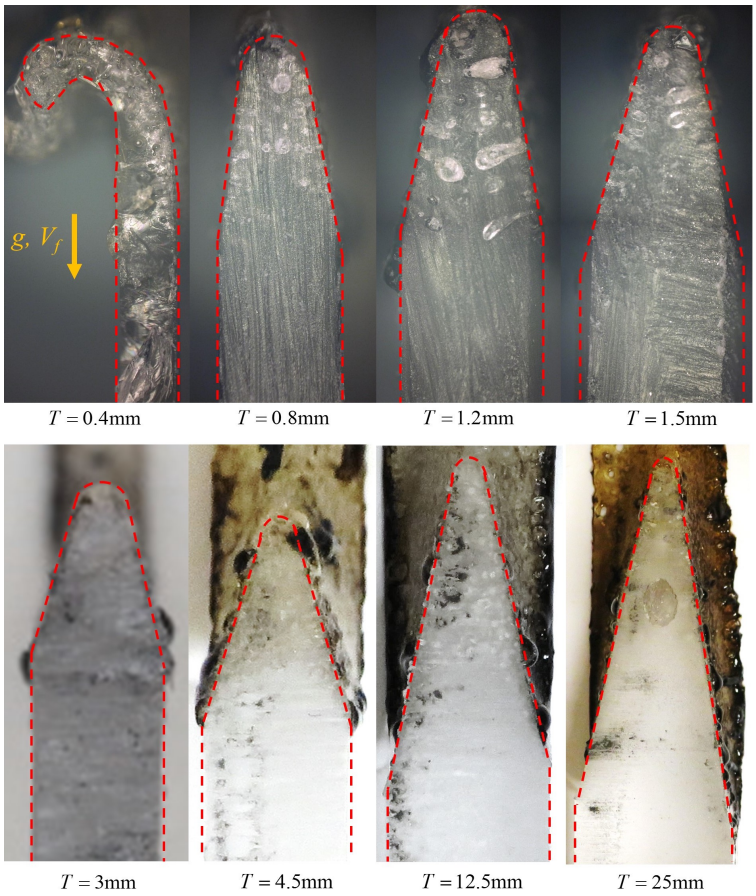

Figure 3.11: Sample pictures obtained with a microscope (2τ from 0.4 to 1.5 mm) and a digital camera (3 to 25 mm). Only the pictures obtained with the microscope have the same scale (pixel/mm). All the samples show a triangular pyrolysis region, with the exception of $2\tau = 0.4$ mm, where the burning region collapsed. The red dashed lines approximate the contour of the samples.

downward flame spread would differ in length for thin samples if they did not collapse because of gravity.

Burn angles measured through image analysis and the ones deduced from the BASS values of L_p and τ are presented in Fig. 3.13. This figure also includes data from Ayani et al. [87]. The burn angle varies with the sample thickness in a consistent way; it rapidly increases with thickness for very thin fuels, reaching a peak of about 20° and then it gently decreases, approaching an asymptotic value of about 11° for thick fuels. Figure 3.13 also suggests that the burn angle becomes less depend on thickness in the limit for thick fuels, in analogy with the flame spread rate behavior described by Eq. 3.1. The microgravity data (labeled BASS) are extremely important to define the thin-fuel limit. They indicate that the burn angle tends to zero when fuel thickness decreases, because of the different order of magnitude between τ and L_p in the Eq. 3.9.

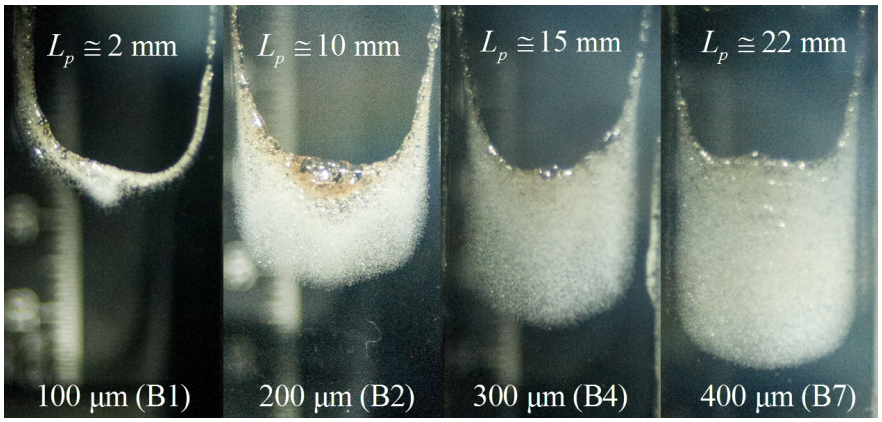

Figure 3.12: Frames after flame extinction from the BASS experiments. The burning conditions are specified in Table A.2.

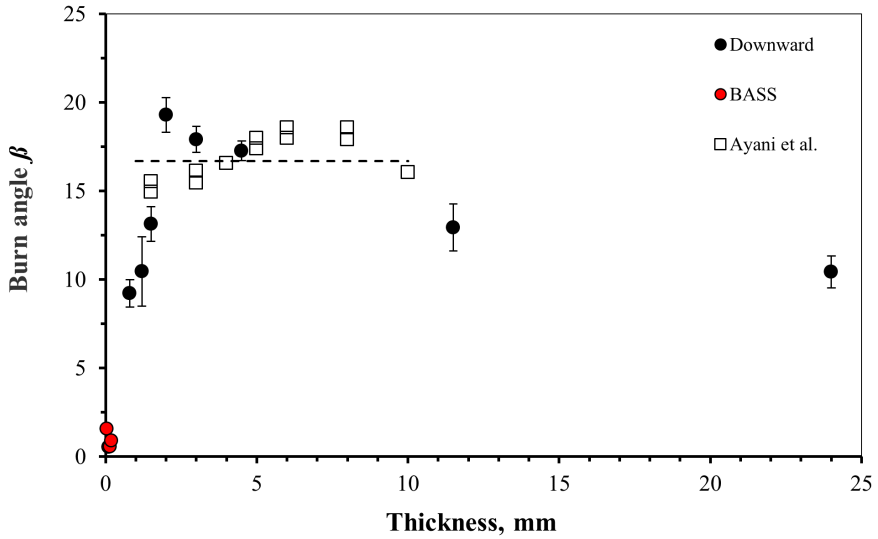

Figure 3.13: Burn angles from different works are compared. The constant value suggested by Ayani et al. [87] is indicated by the dashed line, and it agrees with the experimental values in that thickness range. However, with a larger set of thickness it is clear that the burn angle changes with fuel thickness, increasing for thin fuels and then asymptotically decreasing for thick fuels.

3.3.3 Physical Interpretation: Thin Fuels

The distinction between thermally thin and thick solid fuels is based on the comparison of fuel semi-thickness τ and τ_h (see Fig. 1.2). When $\tau < \tau_h$ the fuel is treated as thermally thin, with no temperature gradient along the y-direction. Consider the leading edge of a spreading flame as shown schematically in Fig. 3.14. In this flame-fixed coordinate system the virgin fuel approaches the flame with constant velocity V_f, and the solid temperature rises from the ambient value to the temperature of the pyrolysis region T_p, where the fuel vaporizes.

The vaporization temperature corresponds to the temperature of the pyrolysis region, and it is

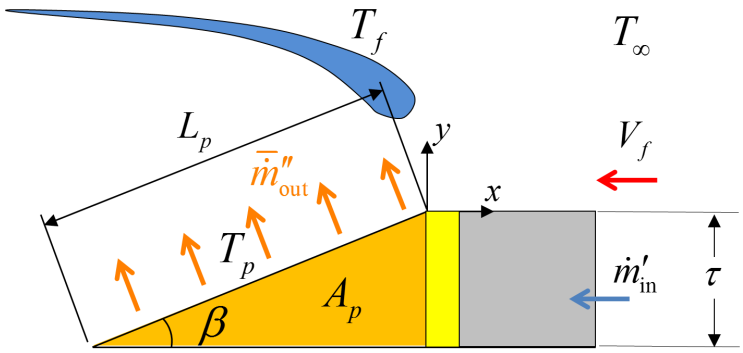

Figure 3.14: Symmetric-half of a control volume in flame-fixed coordinates, where the fresh fuel approaches the flame at a speed equal to V_f. In the thin-fuel approximation the pyrolysis region has a uniform temperature.

assumed to be a fuel property. The burn angle reflects the competition of flame spread and surface regression rates, and a relation for the mass burning rate can be obtained starting from a mass balance. The mass flow rate per unit width entering the control volume of Fig. 3.14 is:

$$\dot{m}'_{\text{in}} = \rho_s V_f \tau \tag{3.11}$$

and using V_f from Eq. 3.1 we obtain:

$$\dot{m}'_{\text{in}} = \frac{\pi}{4} \frac{\lambda_g}{c_s} F \tag{3.12}$$

The right-hand side of Eq. 3.12 is independent of fuel thickness and the thermodynamic parameters are constant for a given environment, therefore $\dot{m}'_{\text{in}}$ must be constant for thin fuels. By substituting property values from Table A.1 and $F = 4.76$, $\dot{m}'_{\text{in}}$ can be calculated to be about 0.238 g/(m·s). In Fig. 3.15 this value is compared to Eq. 3.11 calculated with experimentally measured spread rates, showing good agreement for almost all the thicknesses explored.

The mass burning rate per unit width can be obtained alternatively by integrating a volumetric burning rate over the pyrolysis cross-sectional area A_p (see Fig. 3.14):

$$\dot{m}' = \iint_{A_p} \dot{m}''' dA \tag{3.13}$$

An expression for the volumetric burning rate can be derived from a first-order Arrhenius equation [88, 89], in analogy to the ones used by Kacem et al. [90] and by the Fire Dynamics Simulator (FDS) code from NIST [91]. In symbols:

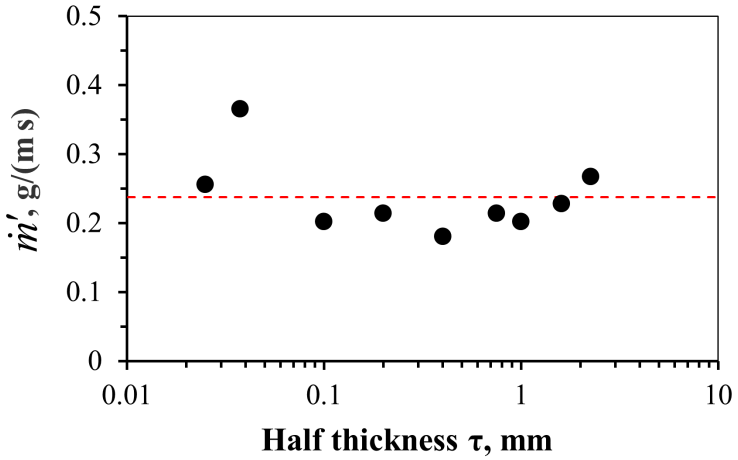

Figure 3.15: The mass consumption rate per unit width is not dependent on thickness according to de Ris' spread rate (Eq. 3.1) and experimental data.

$$\dot{m}''' = \rho_s A \exp\left(-\frac{E_a}{RT_p}\right) \tag{3.14}$$

with T_p being the temperature of the pyrolysis region, which is constant along the y-direction (thin fuel approximation). To simplify the integration of the mass burning rate in Eq. 3.13, an average temperature of pyrolysis $\overline{T}_p$ could be used in Eq. 3.14 instead of T_p. This assumption is hard to prove experimentally for thin fuels for practical reasons, hence the temperature profile in the solid phase is numerically investigated. With the flame located at $x = 0$ and the virgin fuel at $x > 0$, Fig. 3.16 shows the rise in temperature from the ambient to the pyrolysis values along the burning region. The profiles relative to five values of τ, from $12.5 \cdot 10^{-3}$ to 0.75 mm, are compared; temperatures of very thin fuels keep increasing until the fuel completely burns out, but this increase gets smoother with thickness. We can calculate an average fuel temperatures between the burn out point and $x = -2$ mm (indicated by the red dashed line in Fig. 3.16), reducing eventual uncertainties due to the initial temperature rise from the preheating zone. For a given fuel thickness, the temperature along the x-direction does not vary more than 5% with respect to the average value, justifying the constant temperature assumed for the integration of Eq. 3.14.

The numerical results in Fig. 3.16 also show (i) temperatures of the pyrolysis regions varying with thickness, with higher temperatures for thinner fuels, and (ii) longer pyrolysis regions for thicker fuels (in agreement with the experiments). Five additional intermediate thicknesses (not shown in the figure) are used to correlate $\overline{T}_p$ and τ, giving a logarithmic dependence:

$$\overline{T}_p = -50.8 \ln \tau + 215 \tag{3.15}$$

The variation of the average temperature of the pyrolysis region $\overline{T}_p$ is in contrast with de Ris' as-

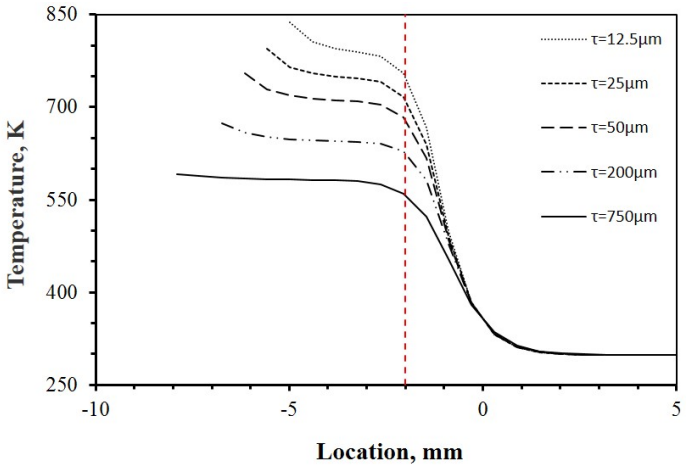

Figure 3.16: Temperature profiles in the solid fuel for different thicknesses. These results show the decrease in temperature for larger thicknesses, as well as a little increment in the length interested by pyrolysis. The flame is located at $x = 0$.

sumption of a fixed fuel vaporization temperature ($T_p = T_v = \text{const.}$). However, $\overline{T}_p$ is not a thermodynamic property, but a result of pyrolysis kinetics and heat balances between flame and fuel. A priori vaporization temperature has been strongly criticized by Sirignano [92], who claimed that it should change with thermodynamic parameters as well as burning and fuel characteristics. Frey and T'ien [89] showed that a constant vaporization temperature is a good assumption when the pyrolysis zone is much longer than the thermal length, but it is not a fuel constant and rises approaching the end of the pyrolysis region. By varying the fuel thickness, we expect the average temperature to decrease because of the larger section that needs to be heated up, as suggested by Fig. 3.16.

Referring again to Fig. 3.14, the pyrolysis area can be approximated as $A_p = \tau^2 / (2 \tan \beta)$, and the integration of Eq. 3.14 results in:

$$\dot{m}' = \frac{\tau^2}{2 \tan \beta} \rho_s A \exp\left(-\frac{E_a}{R\overline{T}_p}\right) \tag{3.16}$$

Substituting $\dot{m}'$ from Eq. 3.12 we obtain a predictive equation for the burn angle:

$$\tan \beta = \tau^2 \frac{2\rho_s c_s}{\pi \lambda_g F} A \exp\left(-\frac{E_a}{R\overline{T}_p}\right) \tag{3.17}$$

Equation 3.17 shows that the burn angle increases with τ^2 and is inversely proportional to the temperature ratio F. The latter dependence implies that when the flame temperature decreases, for example because of a lower oxygen concentration, the burn angle increases.

The burn angle in Eq. 3.17 also depends on the average pyrolysis region temperature $\overline{T}_p$, which

varies with fuel thickness; both mass burning rate and burn angle increase with an increase in $\overline{T}_p$. By using the property values from Table A.1 for the parameters in Eq. 3.17 and numerical temperatures from Eq. 3.15, the behavior of β as a function of τ is plotted in Fig. 3.17, adjusted by a multiplicative factor of 2 to match the experimental values from Fig. 3.13. The model shows a gradual increase with semi-thickness, and more importantly it seems to slowly reach a maximum before decreasing at larger thicknesses. It should be noticed that a variable $\overline{T}_p$ with thickness also affects the ratio F, which is not constant anymore. The use of a F number with varying vaporization temperatures modifies the burn angle curve moving up the peak obtained with constant F, as indicated by the blue dash line in Fig. 3.17 (in this case we used a multiplicative factor of 3), but does not change the qualitative results. Furthermore, the prediction of Eq. 3.17 with a fixed $\overline{T}_p$ indicated by the gray dot-and-dash line in Fig. 3.17 shows a rapid increase of β for very thin fuels, but as τ keeps increasing the trend diverges. Although there is no direct experimental evidence for variations in the average temperature $\overline{T}_p$, these could be responsible of the non-monotonic behavior of burn angles.

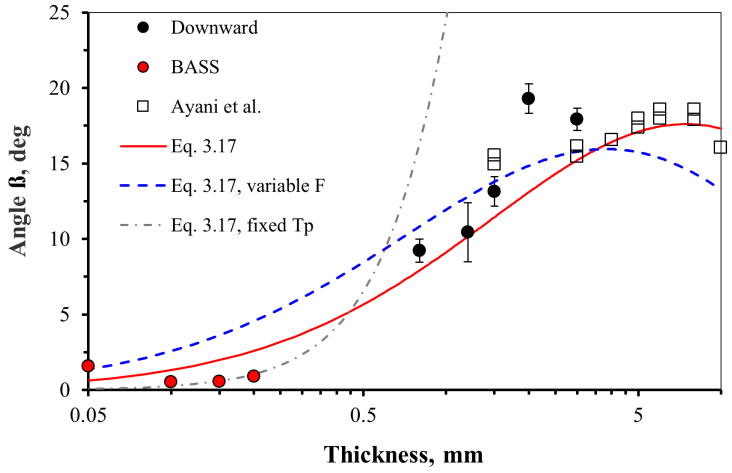

Figure 3.17: By using a constant vaporization temperature, Eq. 3.17 can describe the increase of the burn angle in thin fuels (gray line), but only with a variable temperature the burn angle behavior is well approximated.

The calculated burn angles using Eq. 3.17 can be used to predict the average mass flux leaving the pyrolysis region. By considering again the flame schematic of Fig. 3.14, the mass flow rate leaving the surface can be expressed as $\dot{m}'_{\text{out}} = \overline{\dot{m}}'' L_p = \overline{\dot{m}}'' \tau / \sin\beta$, where $\overline{\dot{m}}''$ is the average mass flux:

$$\overline{\dot{m}}'' = \rho_s V_f \sin\beta \tag{3.18}$$

Because of the relatively small size of the pyrolysis regions with respect of the flames considered in

this study, we do not expect large differences of local burning rates from their average values. Furthermore, by substituting V_f in Eq. 3.18 from de Ris' solution of Eq. 3.1:

$$\overline{\dot{m}}'' = \frac{\pi}{4}\frac{\lambda_g F}{c_s \tau}\sin\beta \tag{3.19}$$

Figure 3.18 compares the mass flux obtained from Eq. 3.19 combined with Eq. 3.17 with a variable (red line) and fixed (gray line) temperature $\overline{T}_p$, along with the values obtained experimentally by using Eq. 3.10 that clearly show higher mass fluxes for thinner fuels. The model with constant $\overline{T}_p$ catches the qualitative behavior of the experimental values, but a varying solid temperature in Eq. 3.17 agrees with experimental results within a 10% range for $0.4 < \tau < 1.5$ mm. Furthermore, the burn angle model with varying $\overline{T}_p$ is used to determine the pyrolysis region length increase with τ (simply as $L_p = \tau/\sin\beta$), and the results are compared to the experimental data in Fig. 3.18.

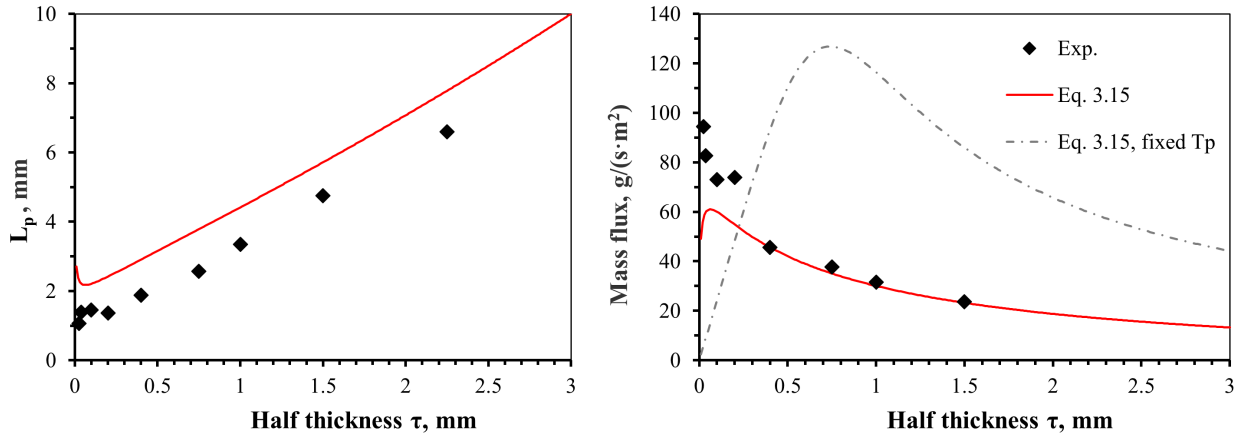

Figure 3.18: Mass flux predicted using Eq. 3.18 (red solid line) and with a fixed vaporization temperature (gray line). Data points from experiments are reported according to Eq. 3.10. Pyrolysis length values measured from image analysis agree with calculated values starting from the burn angle.

The good agreement of $\overline{\dot{m}}''$ and L_p with the predicted values fails only when τ becomes very small. This issue can be explored with a sensitivity analysis on how a measurement error for the burn angle propagates to the prediction of $\overline{\dot{m}}''$. Taking the logarithm of Eq. 3.18 and evaluating the differentials of each side produces:

$$\ln\overline{\dot{m}}'' = \ln(\rho_s) + ln(V_f) + \ln(\sin\beta) \qquad \longrightarrow \qquad \frac{d\overline{\dot{m}}''}{\overline{\dot{m}}''} \sim \frac{dV_f}{V_f} + \frac{d\beta}{\beta} \tag{3.20}$$

The term containing the solid density ρ_s is approximately constant, and while V_f has a finite value, a decreasing burn angle makes the term $d\beta/\beta$ very large, especially for the very thin fuels. Therefore, small errors in determining for extremely thin fuels propagate significantly in the mass flux calculation.

3.3.4 Physical Interpretation: Thick Fuels

In the thick-fuel approximation the burning region has a temperature gradient along the fuel depth, so the control volume, illustrated in Fig. 3.14 for thin fuels, qualitatively changes to the one indicated in Fig. 3.19. Despite the temperature gradient, the simple model to calculate an average mass burning rate based on a mass balance (see Eq. 3.18) is still valid.

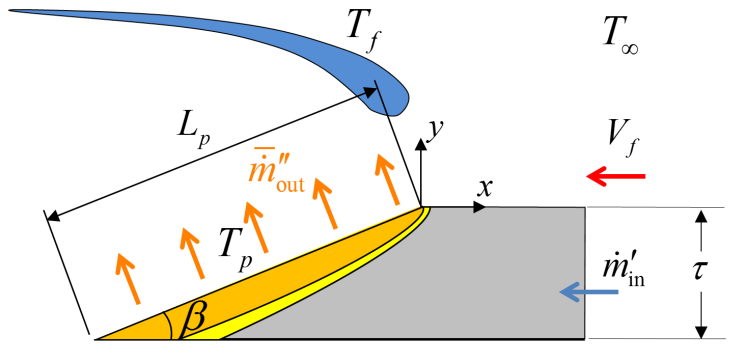

Figure 3.19: Control volume of spreading flames over thick fuels. The flame is stationary and the virgin fuel is fed with a velocity equal to the flame spread rate V_f. Only the superficial region of the fuel is heated up the flame.

It is interesting to notice that, although both V_f and β vary with thickness (see Figs. 3.1 and 3.13), it is reasonable to expect the average mass flux in Eq. 3.18 to vary as well. From Fig. 3.17, however, we can see that $\overline{\dot{m}}''$ is higher for thin fuels and then gently decreases with thickness. Assuming the asymptotic values for V_f and β for thick fuels according to the experimental results (respectively 0.042 mm/s and about 11°), the average mass flux leaving the burning surface is 9.54 g/(m$^2 \cdot$ s), really close to the average value of 9.72 g/(m$^2 \cdot$ s) reported by Singh et al. [77]. Their theoretical expression of the local mass flux for vertical PMMA is function of the distance x from the flame front, $\dot{m}'' = 0.00132 \cdot x^{-0.374}$ (with x expressed in cm), and it slightly overestimates the experimental values. Integrating this relation over the burning length L_p, which is directly proportional to the sample thickness (see Fig. 3.11), and dividing the result by L_p we were able to obtain average mass fluxes to compare with our experimental results. Figure 3.20 shows the values of mass flux obtained from our direct measurements compared to the averaged values from Singh et al. theoretical and experimental expressions. The decreasing trend is consistent with the data from thin fuels (Fig. 3.18), and could be justified with the increase in thickness that would gradually increase the heat conducted to the deeper and fresh fuel. When the sample thickness is much larger than the conductive scale length in the solid fuel the mass flux approaches the same average value of non-spreading flames or flames spreading only on one side of a vertical wall.

The strong dependence on thickness of burn angle and mass flux, and their eventual thick limits,

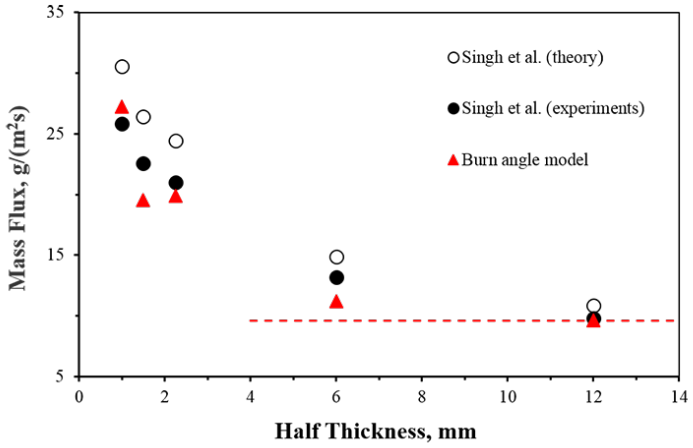

Figure 3.20: The average mass flux decreases for increasing thickness, as shown by the experiments and the comparison with Singh et al. experimental and theoretical correlations [77], which were integrated along the measured pyrolysis length L_p.

suggests a connection with the thick fuel limit for the flame spread rate. To justify the variation of the burn angle it can be useful at this point to refer to the vertical regression rate at the flame leading edge instead of the mass flux by using the relation $\dot{r} = \overline{\dot{m}}''/\rho$. The regression rate in the vertical direction is not constant, especially in the ignition transient, as suggested by other studies [76, 93]. The nature of the burn angle behavior could be explained as follows; in 2D flames, the flame spread rate in a purely convective configuration is constant, and experiments confirm that the spread rate does not change from the beginning to the end of the experiments. Moreover, the flame spread rate becomes independent on thickness in the thick limit. The regression rate seems to have a similar behavior; it is higher at the beginning (in the first layer of the fuel surface), and then decreases until it reaches a constant value at a critical depth. The higher values in the first region of the sample thickness could be justified with a higher heat transfer rate due to the vicinity of the flame (intuitively, the fuel layers exposed to the flame are hotter than the ones below the surface). When the half-thickness is lower than the critical depth, the equilibrium between spread rate and regression rate is not achieved and the burn angle varies with thickness, as shown qualitatively at the top of Fig. 3.21, where the blue and red dots represent the vertical regression and the horizontal spread at different time-steps. On the contrary, when this depth is smaller than half-thickness of the fuel, both flame spread rate and regression rate become constant and the burn angle approaches an asymptotic value, as shown at the bottom of Fig. 3.21. According to Fig. 3.13, the burn angle is close to the thick value for $\tau \sim 6$ mm, so the critical depth is expected to have a similar value for downward flame spread (this value is also in agreement with the transition between thick and thick fuels).

Of course, the complexity of assigning an appropriate B number and integrating the hydrodynamic effect is avoided in this model because the proposed formula is only for downward spreading flame over a

specific fuel, but it provides a very simple approach to experimentally measure the average burning rate.

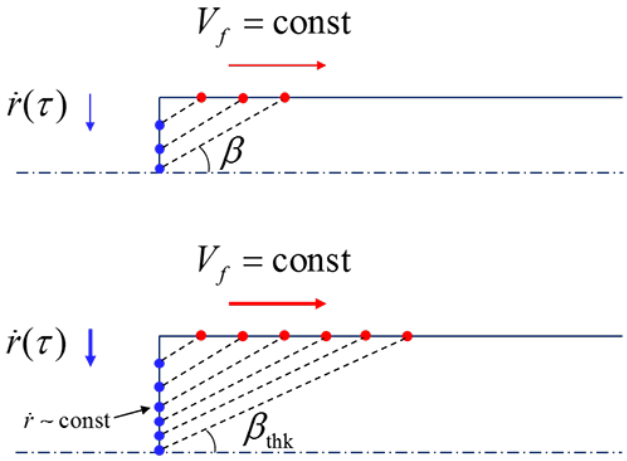

Figure 3.21: The burn angle depends on the fuel thickness. If the regression rate becomes constant before reaching the semi-thickness depth, the burn angle becomes constant with a value of about 11°.

3.4 Flame Length

3.4.1 A Broader Comparison

In Chapter 1 we have seen how flames are traditionally classified in order to simplify their analysis and isolate the importance of a few parameters at the time. However, due the common nature of flames, it is often possible to find similarities that can help with a wider generalization of models. The length of a flame, for example, can be compared across almost all types of problems. Intuitively, the flame length is driven by the amount of fuel that is burning. It is not surprising to find similarities in flame length calculations between gaseous jet flames [94, 95], flames over solid fuels [96], and bigger flames such as in pool fires [97]. In all of the mentioned works, the flame length is somehow related to the amount of fuel injected (gaseous fuels) or produced by vaporization (condensed fuels). The aim of this section is to see if these developed models agree with the experimental results from small spreading flames over solid fuels, where the thickness and geometry of the sample can be varied.

3.4.2 Analogy with Pool Fires: Experimental Results

Several PMMA samples with thicknesses varying between 0.05 and 12 mm were burnt in the Flame Tunnel without any forced flow, and the flame length was measured from the experiment videos with FIAT (the same samples burning against an opposed flow will be considered in the next Chapter). The dimensions of the samples with $2\tau > 2$ mm were 50 mm in width and 50 mm in length, while thinner samples were

longer (200 mm) and less wide (30 mm). The flame length increases with fuel thickness, as shown by the representative flames in Fig. 3.22. Larger values of thickness could not be tested because of the fast increase in flame size and the limited space available in the Flame Tunnel. It is this transition to turbulent and big flames that suggests a similarity between these spreading flames and larger pool fires.

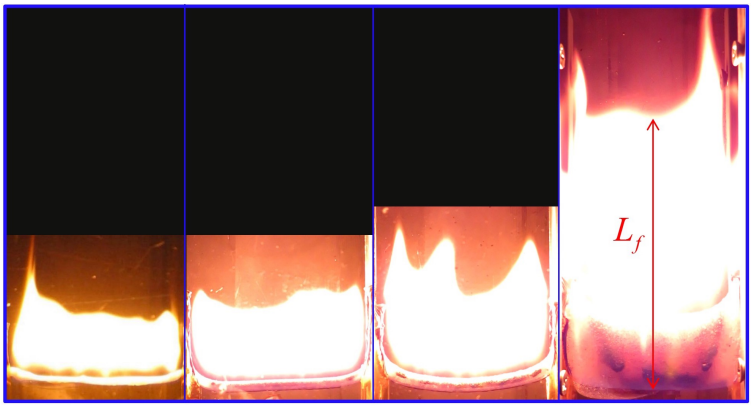

Figure 3.22: Flame length over PMMA samples with different thickness.

There are several studies analyzing many aspects of pool fires. Different correlations have been developed between mass flux and flame height of pool fires [98, 99], which can be summarized by [97]:

$$\frac{L_f}{d} = k \left(\frac{\dot{m}''}{\rho_g \left(gd\right)^{1/2}} \right)^n \tag{3.21}$$

with k, n being constants that depend on the pan size, varying respectively between 16 and 46 and 0.4 and 0.8, whereas d is the diameter of the pan. The flame length is proportional to the fuel mass flux $\dot{m}''$ and inversely proportional to a term representing the buoyant flow. To test the validity of Eq. 3.21, we can assume the pan diameter d to be analogous to the thickness 2τ of a flat sample, and calculate the average mass flux with the mass balance $\dot{m}'' = \rho_s V_f \tau / L_p$ (equivalent to Eq. 3.18). Table 3.1 shows the comparison of flame lengths measured with FIAT and calculated with Eq. 3.21 (assuming $k = 30$ and $n = 0.4$). From this first comparison, we can see that the values predicted by the pool fire expression have the same order of magnitude of the experimental results.

Table 3.1: Measured flame lengths are compared to estimated value from Eq. 3.21 by using the experimental values of V_f and L_p. All the values are indicated in mm.

Fuel Thickness	L_f (exp.)	L_f (pool fires)
0.2	18.01	6.72
0.8	18.48	17.6
2	30.75	30.4
4.5	50.37	49.5

Since the measured flame length agree well with Eq. 3.21, the next step is to provide an estimate for the mass flux to use in the equation. An expression for mass flux over thin fuels has been developed starting from de Ris' theory, resulting in Eq. 3.19. The pyrolysis length increases almost linearly with thickness (see Fig. 3.10), so we can approximate $L_p \sim 2\tau$. In alternative, we can consider the mass flux in a free convective flow as function of the Grashof number (defined as $\mathrm{Gr}_x = gx^3 \left(T_w - T_\infty\right) / \left(\nu_g^2 T_\infty\right)$) and the coordinate along the solid fuel [96]:

$$\dot{m}''(x) = -\frac{3\nu_g \rho_g f(0) \mathrm{Gr}_x^{1/4}}{x\sqrt{2}} \tag{3.22}$$

Because of the limited length of the pyrolysis region (less than 10 mm for all sample thicknesses less than 12 mm), we can average the mass flux by integrating it along the pyrolysis region:

$$\overline{\dot{m}}'' = \frac{\int_0^{L_p} \dot{m}''(x)}{L_p} = -\frac{2^{3/2}\nu_g \rho_g f(0) \mathrm{Gr}_x^{1/4}\Big|_0^{L_p}}{L_p} \tag{3.23}$$

To obtain the average mass flux it is necessary to estimate the variation of the pyrolysis length L_p with thickness, which is introduced for thin fuels by Eq. 3.17 and Eq. 3.15. The comparison between experimental values of flame length and the estimates from thermal theory (Eq. 3.19) and from a convective flow (Eq. 3.23), is shown in Fig. 3.23. This comparison suggests that the flame length for downward spreading flames can be estimated from the same relation used for pool fires. Furthermore, the averaged mass flux from Eq. 3.23 well describes the variation of flame length with thickness, while the thermal theory from de Ris better represents the flame lengths over thin fuels.

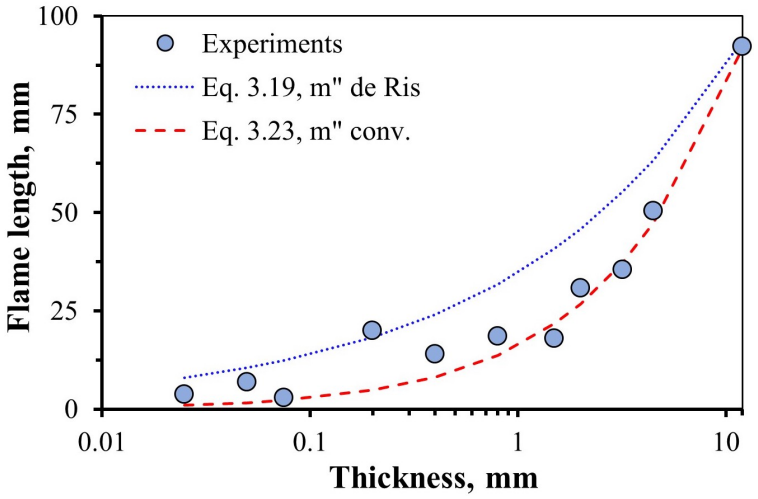

Figure 3.23: Experimental values of flame length are compared to the pool fires relations from Eq. 3.21. The average mass flux is calculated with Eq. 3.19 or 3.23, estimating the pyrolysis length from Eq. 3.17.

Chapter 3, in part, has been published in the Proceedings of the Combustion Institute (T. Delzeit, L. Carmignani, T. Matsuoka, S. Bhattacharjee, Influence of edge propagation on downward flame spread over three-dimensional PMMA samples, Proc. Combust. Inst. 37, pp. 3203-3209, 2019) and Fire Technology (L. Carmignani, B. Rhoades, S. Bhattacharjee, Correlation of Burning Rate with Spread Rate for Downward Flame Spread Over PMMA, Fire Technol. 54, pp. 613-624, 2018) and Combustion Science and Technology (L. Carmignani, S. Bhattacharjee, Burn Angle and Its Implications on Flame Spread Rate, Mass Burning Rate, and Fuel Temperature for Downward Flame Spread over Thin PMMA, Combust. Sci. Technol., 2019, in press). The thesis author was the primary investigator in these publications.

Chapter 4

The Kinetic Regime

4.1 The Effect of a Forced Flow

The downward flame spread described in Chapter 3 is a special case of opposed-flow flame spread, where the velocity experienced by the flame leading edge is naturally driven. Yet, in several scenarios the opposed flow could have an additional components from external sources, such as from a ventilation system.

A forced flow can affect the flame in several ways. It can slow down chemistry by reducing the residence time of the oxidizer near the flame leading edge, or help a flame in microgravity to spread more vigorously. The residence time scales with:

$$t_{\text{res}} \sim L_g/V_g \sim \alpha_g/V_g^2 \tag{4.1}$$

where $L_g \sim \alpha_g/V_g$ is the gas diffusive length. The residence time, as suggested in Chapter 1, can be compared to other time scales of the problem to determine the burning regime.

The chemical time required to consume the fuel in a control volume (assuming a second-order Arrhenius kinetics) can be defined as [100]:

$$t_{\text{chem}} \sim \frac{\rho_g x_F}{\rho_g^2 x_F x_O A_g \exp\left(-T_a/T_f\right)} \sim \frac{1}{\rho_g x_O A_g \exp\left(-T_a/T_f\right)} \tag{4.2}$$

where A_g is the pre-exponential factor. The ratio of residence and chemical time, defined as the Damköhler number, becomes:

$$\text{Da} \sim \frac{t_{\text{res}}}{t_{\text{chem}}} \sim \frac{\alpha_g \rho_g A_g x_O x_F \exp\left(-T_a/T_f\right)}{V_g^2} \tag{4.3}$$

Other expressions of the Damköhler number are available in the literature [17, 89, 101, 102], but despite their differences they all indicate the importance of chemical reactions for flame structures. A non-dimensional number analogous to Eq. 4.3 was defined by Frey and T'ien [89], and its dependence on flow velocity, ambient pressure and oxygen concentration was numerically investigated. The Damköhler number well explains variations in flame spread rate due to flow velocity [84, 103–105], but it depends on several thermodynamic parameters. The effect of oxygen concentration under a forced flow was investigated by Fernandez-Pello et al. [28], who showed how flame spread rates over flat fuels first increase and then decrease as a function of flow velocity, with the peak values depending on fuel thickness and oxygen level. More recently, Zhao et al. explored the effect of pressure on flame spread rate and flame height for downward spread [65]. By testing PMMA slabs in locations with three different ambient pressures, they measured the increase in flame strength at higher pressures. However, the evaluation of the Damköhler can cause some deviations from experimental results [12, 105].

When the Damköhler number is large, meaning that $t_{\text{res}} \gg t_{\text{chem}}$, finite-rate chemistry effects can usually be neglected. In contrast, they become increasingly important with lower values of Da, eventually causing flame extinction when $t_{\text{res}} \sim t_{\text{chem}}$.

The interaction between solid fuel and flow field could modify the velocity facing the flame leading edge with respect to the upstream value, with implications on local Damköhler number and flame spread. The influence of a boundary layer has been included in some previous works by using a linear velocity gradient [103, 106], with good agreement with the experimental results especially at higher values of Da. Altenkirch and Vedha-Nayagam used these conclusions to evaluate the scale of a critical velocity at extinction by varying oxygen concentration and flow velocity over thin PMMA [105]. Bhattacharjee et al. [43] introduced an effective velocity to justify the variation of flame spread rate with the development length of the boundary layer in front of a flame. Assuming a linear velocity gradient over the boundary layer thickness, this effective velocity is calculated at a location $y = L_g$ from the fuel surface (see Fig. 4.1). From scale analysis refined with the numerical results [43]:

$$V_{\text{eff}} \sim \frac{V_g}{\sqrt{\text{Pr}}\text{Re}_x^{1/3}} \tag{4.4}$$

The velocity V_{eff} and its relation with the local Reynolds number Re_{x} at the flame leading edge is in agreement with experiments on cellulosic fuel (ashless filter paper) [38]. Because of the local Re_{x}, the effective velocity is function of the location along the boundary layer (development length x_d, see Fig. 4.1). According to Eq. 4.4: $V_{\text{eff}} \sim V_g^{2/3} x_d^{-1/3}$.

If a developing boundary layer has significant influence on the extinction velocity, then much of

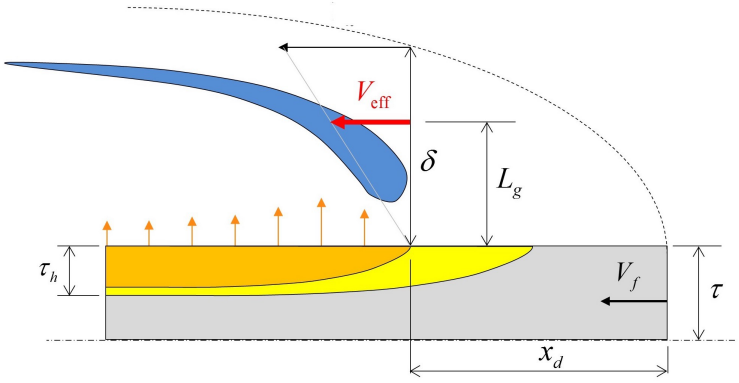

Figure 4.1: The effective velocity is the velocity seen by the flame at the leading edge at $y = L_g$. The velocity gradient is assumed linear.

the experimental data in literature, which do not mention the length of the developing boundary layer, may not be of much use in that regard. In this Chapter, we experimentally explore the importance of development length on blow-off extinction, which is an extreme case of the kinetic regime, starting from the definition of an effective velocity. We also expand the burn angle study from the previous Chapter with a scale analysis to explore its dependence on burning conditions, focusing on the effect of flow velocity which can be compared to experimental results. Finally, the evolution of flame length in the kinetic regime is experimentally investigated.

4.2 Blow-off Extinction

4.2.1 Experimental Results: Thin Fuels

Ashless filter paper (Whatman® grade 1) samples of thickness 0.18 mm, and PMMA samples with thickness of 0.05 and 0.2 mm, were tested in the Flame Tunnel. The samples measured 20 × 200 mm (width and length, respectively). The opposed-forced velocity ranges from 0 (downward configuration) to 100 cm/s.

For the purely downward configuration, the measured spread rate remains invariant, at 1.9 mm/s. This was expected as the buoyancy induced opposing flow is independent of the location of the flame. In the presence of a forced flow, however, the spread rate decreases as the flame moves along the developing boundary layer towards the leading edge, as shown in Fig. 4.2 for a flame spreading over paper against a flow with $V_g = 60$ cm/s. The last part of the sample is shown to highlight the progressive slow down, until the flame extinguishes at about $x = 12$ mm.

The effect of flow velocity on flame spread rates averaged over the experiments duration (not considering the time after flames start experiencing partial blow off) is shown for filter paper in Fig. 4.3. For

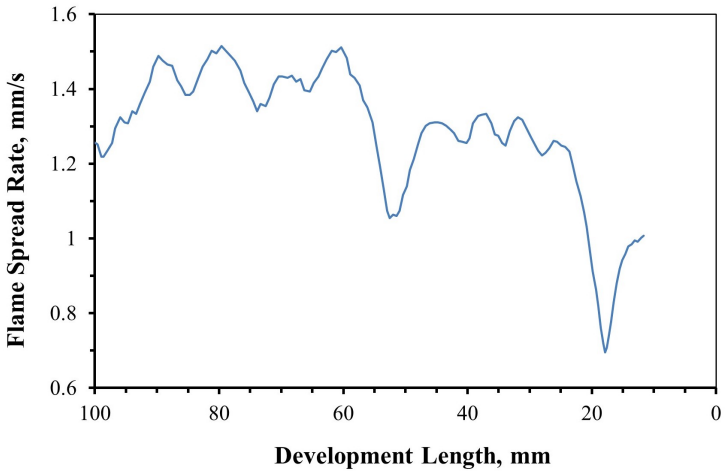

Figure 4.2: Spread rate values as the flame proceeds along the thinning boundary layer generated by a forced flow of 60 cm/s. The flame over filter paper eventually extinguishes about 12 mm before the end of the sample.

$V_g < 20$ cm/s the spread rate is not affected by the forced flow, whereas it decreases with higher flow velocities. The filled symbols indicate that the flame extinguished before reaching the end of the sample. As we can see from this graph the forced flow velocity at extinction is not unique.

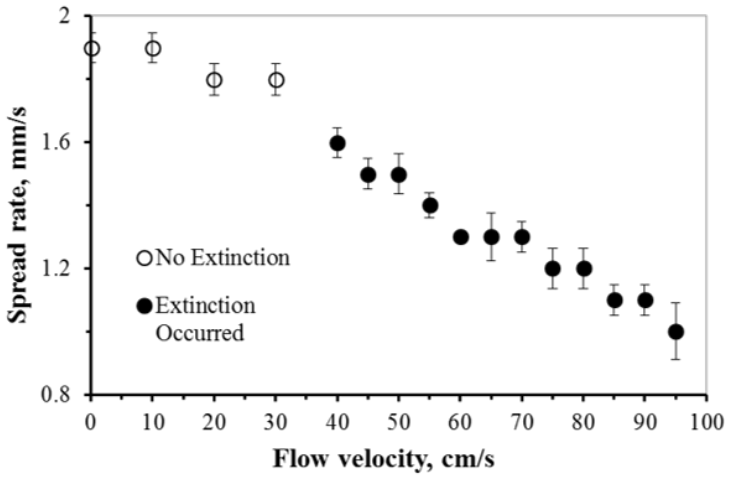

Figure 4.3: Spread rates for filter paper averaged over the entire duration of the experiments. With a velocity above 40 cm/s flames extinguish before reaching the end of the sample (indicated by the filled symbols).

Images of burnt paper samples after blow-off extinction at $V_g = 65$ cm/s and $V_g = 90$ cm/s are shown in Fig. 4.4. Three samples for each extinction velocity are compared to show the repeatability of the results. Samples consistently present a similar extinction location when exposed to the same flow velocity. Moreover, flames extinguish much earlier at higher velocity. The profile of the residual fuel is not perfectly

straight because of smoldering before extinction, but the value of x_d at extinction can be estimated with ImageJ by isolating the unburnt area of the samples and dividing it by the sample width, as indicated on the right of Fig. 4.4. By repeating the experiments 10 to 15 times for each opposing flow velocity ranging from 40 cm/s to 100 cm/s, development lengths at extinction and their standard deviations are reported in Fig. 4.5 for the PMMA and fiter paper samples. The uncertainty of the measurement increases at higher flow velocities, because of partial blow off and smoldering (the latter occurs only for paper). However, there is a clear trend of an increase in extinction values of x_d (called extinction length [105]) with flow velocity.

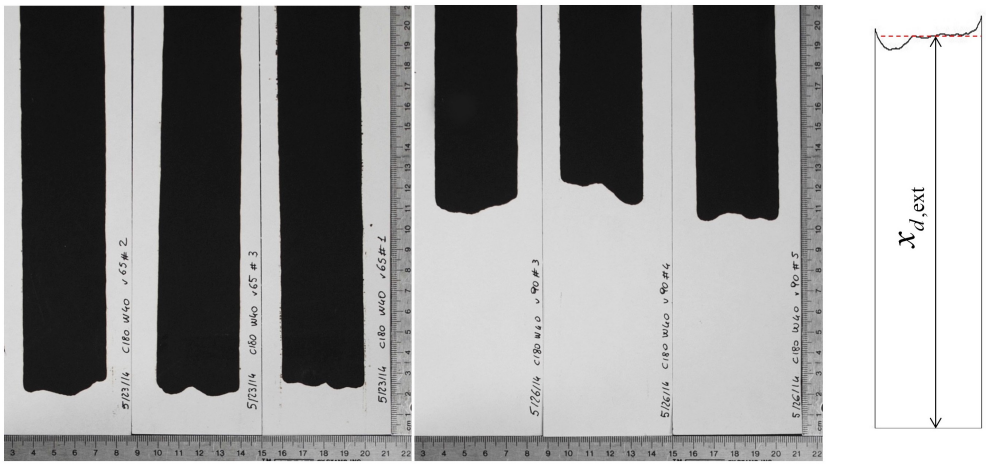

Figure 4.4: Fuel samples after extinction from 3 sets of experiments for Vg = 65 cm/s (left) and 90 cm/s (right) show the repeatability of the extinction length, respectively about 20 and 110 mm in these two cases.

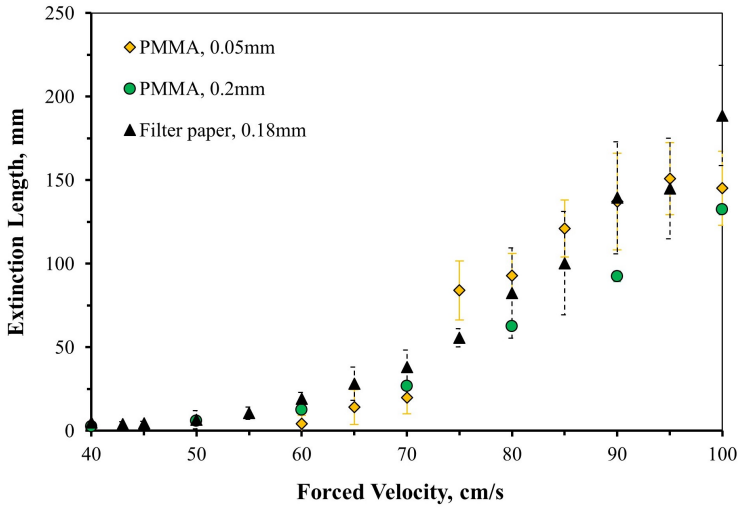

Figure 4.5: Extinction length for different opposing flow velocities for three thin fuels.

4.2.2 Extinction Velocity

The Damköhler number in Eq. 4.3 decreases with V_g because of the residence time, while the chemical time does not change significantly with flow velocity. If flame extinction occurs when Da approaches a critical value, we should expect the existence of a critical value of flow velocity that would extinguish the flame. This critical velocity, here called extinction velocity, depends on burning conditions such as oxygen concentration and ambient pressure [105]. In a developing boundary layer the velocity faced by a flame changes with its location. By referring to the effective velocity introduced by Bhattacharjee et al. [43], V_{eff} increases at lower x_d, therefore the spread rate of a flame is supposed to decrease along the sample and eventually extinguish when the critical velocity $V_{\text{eff,ext}}$ is encountered.

The assumption of a critical effective velocity at extinction implies that the ratio between the free stream velocity V_g and the local Reynolds number (we can assume Pr = 1) in Eq. 4.4 should be constant. The experimental values of x_d can be used to calculate Re_x, and the two terms from Eq. 4.4 are plotted in Fig. 4.6. The data points agree well with the linear relation between V_g and $\text{Re}_x^{1/3}$.

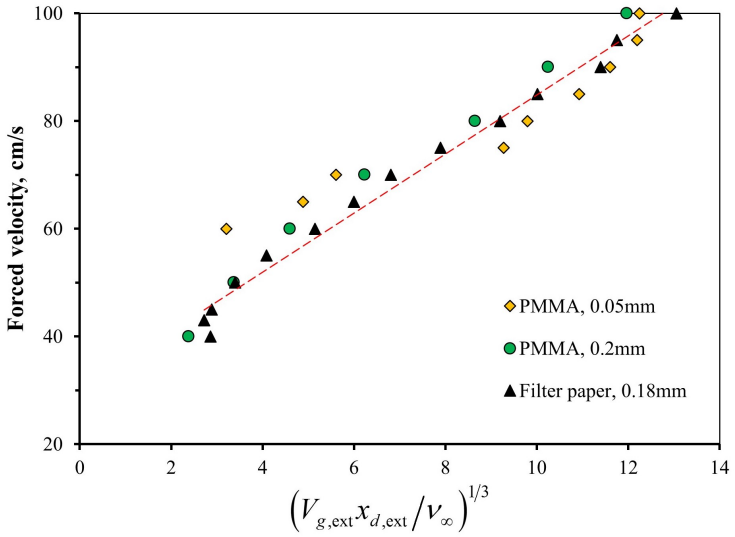

Figure 4.6: The experimental values of extinction length for three thin fuels are used to calculate the local Reynolds numbers. The data show a linear relation between numerator and denominator from Eq. 4.4, suggesting the existence of a critical value of V_{eff} at extinction.

From the experimental data we can deduce that the effective velocity causing extinction is in the range of 30-40 cm/s. This value can be much different from the free stream velocity, depending on the thickness of the boundary layer developed over the fuel surface.

4.3 Experimental Results on Flame Spread

Flames over PMMA samples with thicknesses between 0.05 and 12 mm were exposed to flow velocities from 0 to 120 cm/s in the Flame Tunnel. To reduce the duration of the experiments the sample length was limited to 50 mm for $2\tau > 2$ mm (enough to reach a quasi-steady flame spread), and the exposed width was 50 mm, with the exception of 0.05 and 0.2 mm were the width was 30 mm.

We arbitrarily chose a distance from the leading edge $x_d = 25$ mm as a reference length for fuels with $2\tau > 2$ mm. Flames were extinguished after they consumed half of the sample in order to have comparable measurements for burn angles and other flame characteristics when fuel thickness and flow velocity were varied. Preliminary experiments indeed revealed that these quantities change with x_d because of thinning boundary layer.

The shape of the sample leading edge of fuels thicker than 1 mm could affect the flow along the plate; three different shapes (flat leading edge, V and U-shapes) were tested with a forced flow velocity of 120 cm/s. Sample width, length and thickness (4.5 mm) were kept constant in the three cases. Figure 4.7 shows pictures of the flame fronts and average spread rates of samples with the different shapes. In case of flat leading edge, the flame advancement is very irregular along the sample width, suggesting that the flow is not uniform. Furthermore, the flames on the two sides of the sample were not at the same vertical location. However, the outcome totally changes by repeating the same experiments with the other shapes. Flames spread with a flat front by using U and V shapes. No significant differences were noticed between these two shapes, which produced a similar evolution in time of the spread rate. The V and U shapes were obtained machining the PMMA samples. Since the U shape was easier to obtain in a consistent way because of the small thickness of the samples, it was chosen over the V shape for the rest of the experiments.

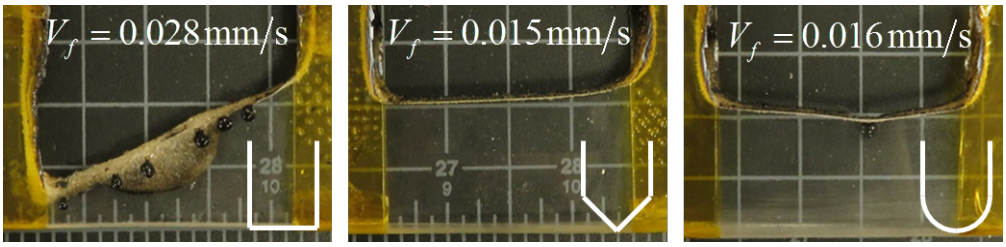

Figure 4.7: Pictures of burnt samples with different shapes of leading edge (from left to right: flat, V, and U-shape). The flame front for the flat case is highly irregular because of the interaction with the forced flow

Figure 4.8 shows flames over the same sample thicknesses of Fig. 3.22 spreading against a velocity of 60 and 90 cm/s (respectively a and b in the figure). From the comparison with Fig. 3.22, we can see how the flames over the thinner fuels ($2\tau < 1$ mm) at 60 cm/s shrunk and changed their colors from bright yellow to blue. At $V_g = 90$ cm/s the flame length over samples with $2\tau < 1$ mm reach a minimum value

before extinguishing at higher velocities, and also the flame over the 3.2 mm thick sample shows a reduction in length and yellow region.

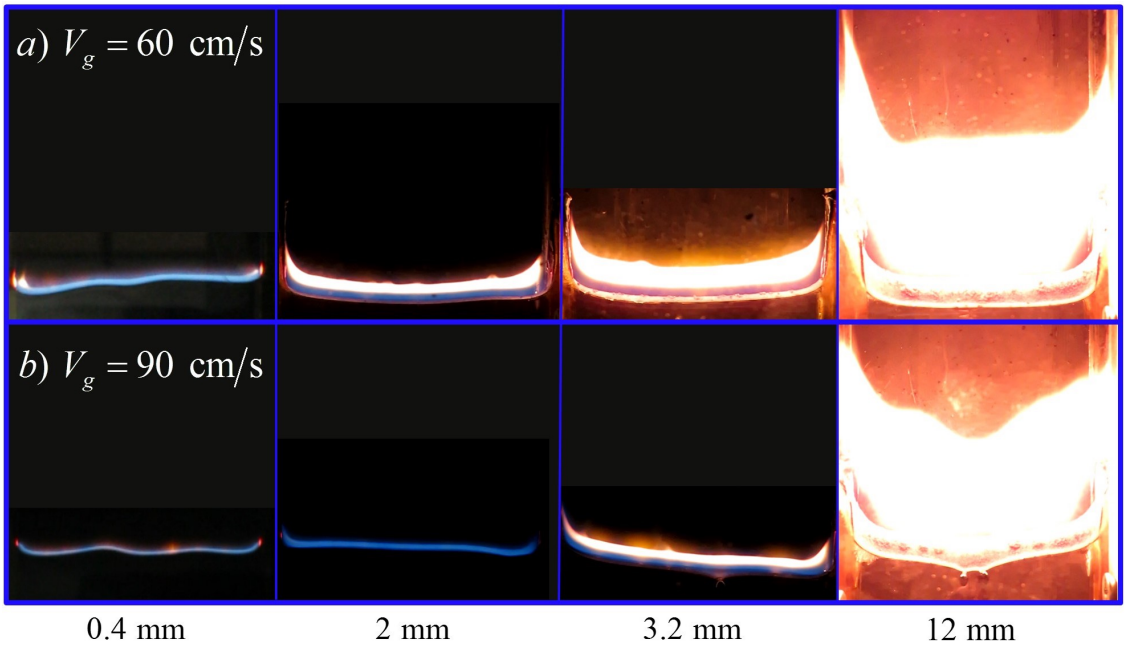

Figure 4.8: Flame length over different thicknesses of PMMA, with velocity V_g of 60 cm/s (top) and 90 cm/s (bottom).

Flames over thinner fuels tend to look very similar to each other when exposed to high flow velocities, suggesting that the flame length is dominated by the gas-phase interaction between the vaporized fuel and the flow velocity. Eventually, also the 3.2 mm thick samples experience a similar flame shrinkage near extinction. This is not clear for the thicker fuel, 12 mm, because the velocity required to extinguish the flame is higher than the maximum speed of the Flame Tunnel. However, with a strong opposed flow the flame could only burn along the sample cross section, "hiding" from the flow along the fuel surface. This behavior partially cancels out the effect of a higher opposed velocity, and it is shown from flame pictures taken from a side window of the Flame Tunnel in Fig. 4.9. The flame region that is directly impacted by the flow has a blue color, typical of weak flames close to extinction over thin fuels, but in the middle of the sample the flow recirculation zone allows the flame to burn vigorously as proven by the presence of soot. By increasing fuel thickness, we expect the flame to become less sensitive to the flow velocity (reconnecting to the pool fire problem), although V_g could be high enough to extinguish the spreading flame along the surface.

After the experiments, when the softened layer solidified, the PMMA samples were cut along their centerline to measure their burn angles as shown in Fig. 3.9. Figure 4.10 shows the variation of burn angles with flow velocity for a sample with thickness of 4.5 mm. From these pictures the burn angle clearly increases with flow velocity, reaching a value of about 90° when $V_g = 120$ cm/s.

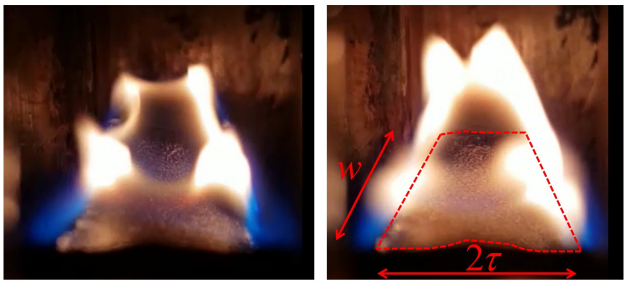

Figure 4.9: Pictures representing the side view of a flame (at two different times) burning against $V_g = 200$ cm/s. The flame is not able to spread along the surface but can burn along the fuel cross-section.

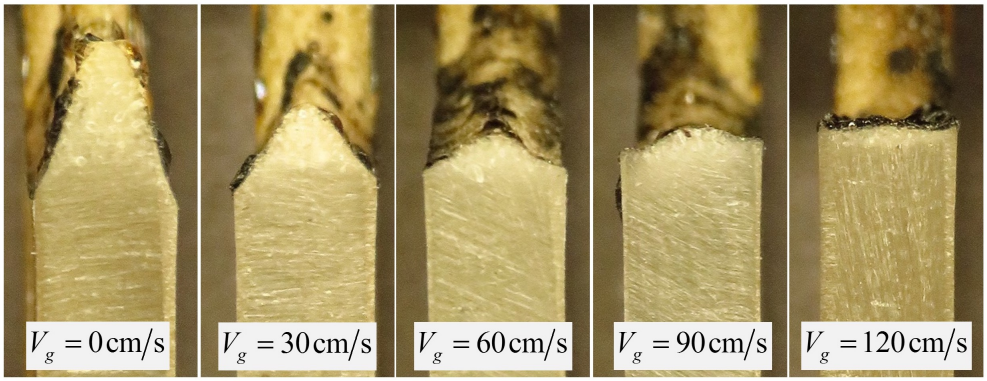

Figure 4.10: Effect of flow velocity on burn angles.

Burn angles and flame spread rates have been measured for four sample thicknesses, and the results are reported in Fig. 4.11. Burn angles were found to be almost independent on thickness between $1 < \tau < 2.2$ mm and until 60 cm/s (on the contrary to what happens in downward flame spread). The thinner samples presented angles larger than 90° for $V_g > 90$ cm/s, meaning that the flame was burning only in the internal part of the sample cross-section (see Fig. 4.9), in analogy with the regressing flames of Huang et al. [86]. Flame spread rates, on the other hand, seem to converge to a value which is independent on fuel thickness, suggesting that this limiting value is controlled by kinetic effects in the gas phase. Flames at high velocities tend to be blue and cover only the cross section of the sample, before suddenly extinguish. These flames were able to survive for a few minutes because of the recirculation zone, but their extinction proves their unsteadiness.

It is interesting to investigate the behavior of the mass burning rate with flow velocity, which can be indirectly evaluated from Eq. 3.18. Because of the large and opposite variations of spread rates and burn angles with flow velocity, we expect the mass flux not to significantly vary with the flow intensity. By using the experimental measurements of spread rates and burn angles, mass fluxes calculated with Eq. 3.18 are reported in Figure 4.12, with the filled symbols indicating the experiments where $\beta \geq 90°$. Thicker fuels

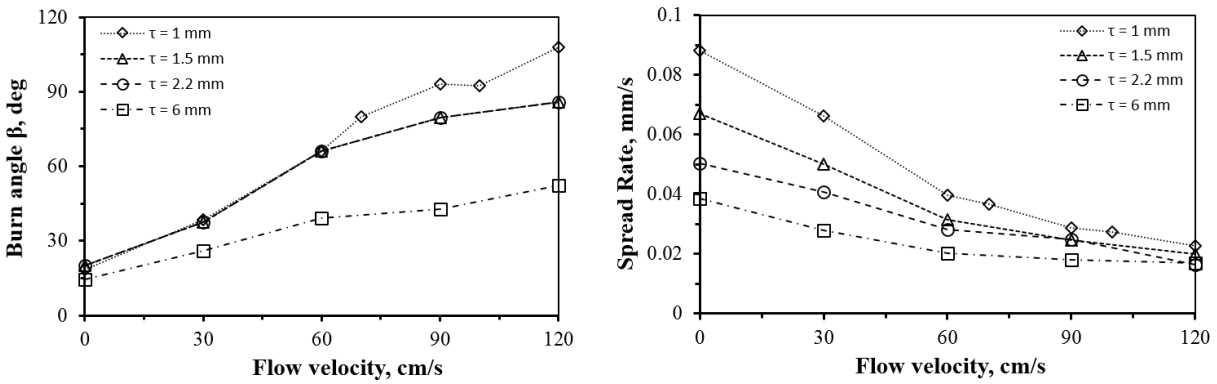

Figure 4.11: Effect of flow velocity on burn angles (left) and spread rates (right). Burn angles in thinner fuels are very similar to each other, whereas spread rates strongly depend on thickness until the flow velocity increases.

have a lower mass flux than thinner fuels, as expected from the results of the previous Chapter. However, the plateau between 30 and 90 cm/s indicates that the mass flux does not significantly vary in this velocity range. Therefore, the variation in burn angle may only depend on the flame spread rate.

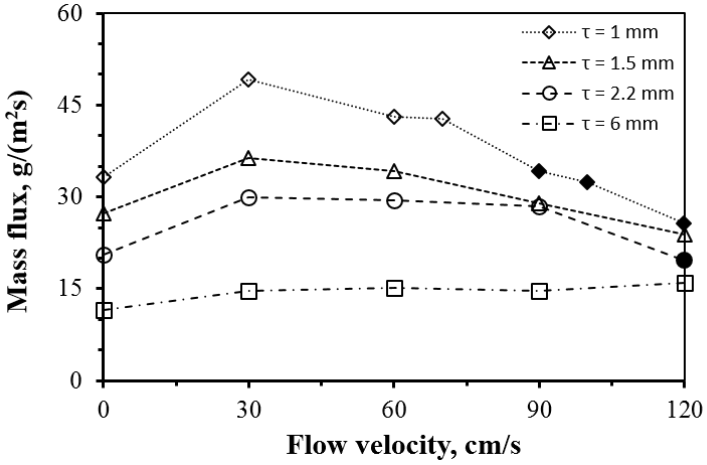

Figure 4.12: Mass flux is higher for thin fuels, but it does not show a strong dependence on flow velocity. The black symbols indicate burn angles equal or larger than 90°.

4.4 A Flow-Driven Flame Length

In Chapter 3 we saw that flame length is related to the mass flux in the pyrolysis region, and we connected the experimental results with the predictive length from pool fires. From the previous sections and other studies it is known that the mass flux does not vary with flow velocity as much as the spread rate. Due to the connection between mass flux and flame length proven in Chapter 3, variations of V_g should not reflect on the flame length. From the direct observation of flames at higher velocities (see Fig. 4.8), however,

the flame length decreases and becomes similar over the various thicknesses of PMMA.

It comes naturally to question whether Eq. 3.21, along with Eq. 3.18 give reasonable solutions for the flame length. The variation of flame length with opposed flow velocity for the tested thicknesses is reported in Fig. 4.13. From the graph we can notice the similar behavior of the thinner fuels by their slope, while flames over the 12 mm samples seem to be less affected by the flow. Unfortunately, Eq. 3.21 predicts an almost constant value of flame length (represented by the solid lines in Fig. 4.13 for each thickness), because the mass flux calculated from the experiments does not change much with V_g (see Fig. 4.12). The wrong prediction in this case is not due to the wrong mass flux calculation. The relation suggested by Pagni and Shih for forced flow would actually predict an increase in mass flux with higher V_g [96], similarly to other fundamental models [68].

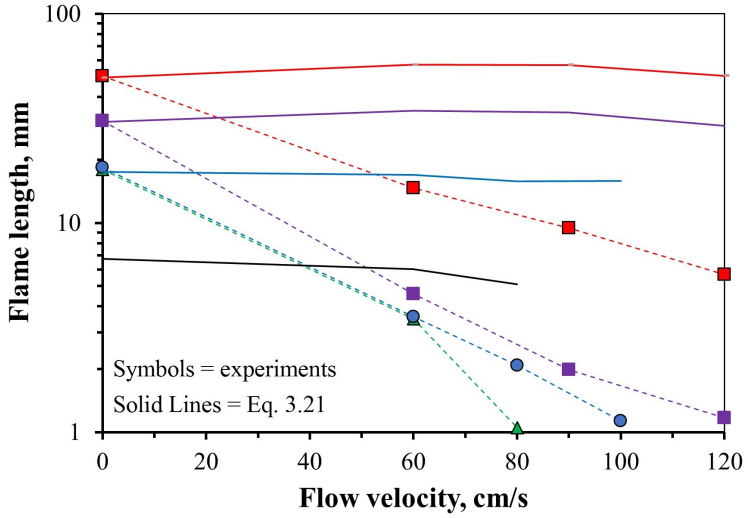

Figure 4.13: Experimental flame lengths are compared to the prediction from Eq. 3.21. The constant average mass flux does not satisfy the decrease of flame length with V_g.

To better estimate the flame conditions varying with flow velocity we considered additional experiments. Flame steadily burning with $V_g = 0$ flow was suddenly exposed to an opposed velocity of 70 cm/s. A thickness of 3.2 mm was chosen because of the longer pyrolysis region with respect of 2 mm thick samples, but lower than the 4.5 mm, which is affected by flow recirculation. The flame evolution is shown in Fig. 4.14. The first frame shows the steady flame spreading downward, while in the second one the flame is facing a flow of 70 cm/s. The flame initially reacts with an increase in flame length, probably due to the vaporized fuel brought at a higher location by the forced flow velocity. After about 10 s the flame length is reduced until it reaches the new equilibrium.

The evolution in time of flame length and pyrolysis region is shown in Fig. 4.15. The vertical dashed lines indicate the time when the flow was changed. The flame length reaches a peak after about 10 s, before

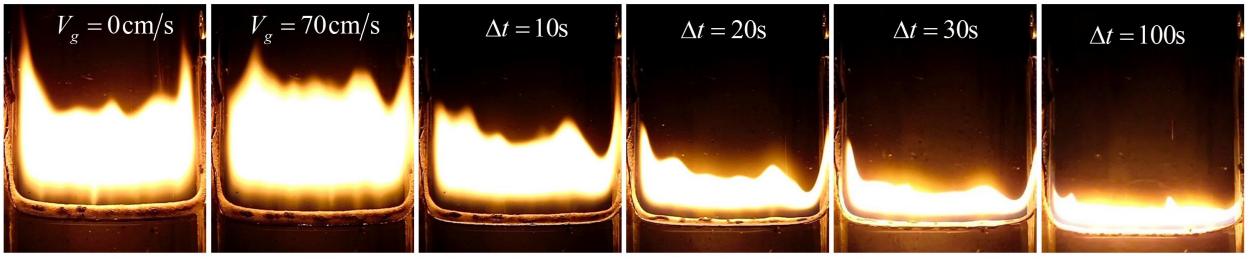

Figure 4.14: A downward spreading flame (first frame) is suddenly exposed to a flow of 70 cm/s (second frame). The flame length eventually adjusts to the new V_g in about 30 s.

shrinking to a much lower value. The pyrolysis region, on the other hand, does not immediately react to the flow, since it is controlled by the slower solid phase. This is also suggested by the pictures of the flame length inside of the graph, representing the symmetric half of steady flames before and after the change in velocity and during the change.

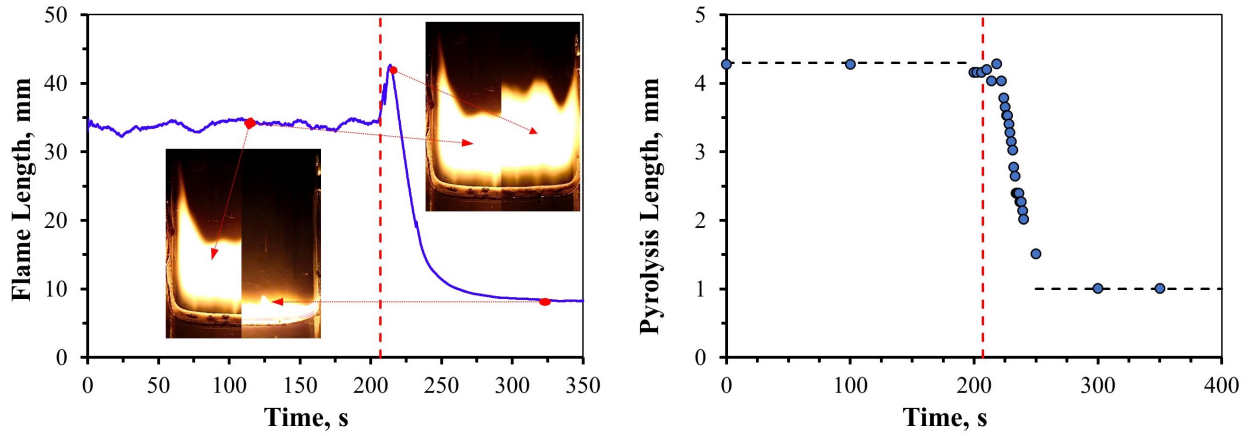

Figure 4.15: The evolution of flame length and L_p is measured over time. After the sudden increase of V_g, the flame length first increase and then reaches a lower value. The pyrolysis region slowly decreases to the new value, but does not seem to vary with a sudden flow velocity.

4.4.1 Kinetic Effects on Flame Length

Since flame length is inversely proportional to V_g and seems to be driven by the gas-phase, we can consider a new mass balance between the vaporized fuel and the oxidizer. By indicating the stoichiometric coefficient with s, we have $\dot{m}'_O = s\dot{m}'_F = 2\rho_s V_f \tau$. The mass consumption rate of oxidizer $\dot{m}'_O$ can be related to the diffusive mass flux:

$$\dot{m}'_O = \int_0^{L_f} \rho_g D \frac{\partial y_O}{\partial x} dx \tag{4.5}$$

We can assume that the length scale of the concentration gradient $\partial y_O/\partial x$ is proportional to the thickness of the thermal boundary layer over the fuel surfaces, which is:

$$\delta_T = \frac{5x}{\mathrm{Re}_x^{1/2}\mathrm{Pr}^{1/3}} \tag{4.6}$$

The thickness δ_T depends on the flow velocity V_g and x because of the local Re. By substituting $\partial y/\partial x$ with $\Delta y_0/\delta_T$, we can integrate Eq. 4.5, obtaining:

$$\frac{2\rho_g D\Delta y_O}{5}\mathrm{Pr}^{1/3}\sqrt{\frac{V_g L_f}{\nu}} = s2\rho_s V_f \tau \tag{4.7}$$

This equation can be solved for L_f:

$$L_f = \frac{\nu}{V_g}\left(\frac{5}{2}\frac{s\rho_s V_f \tau}{\rho_g D y_O \mathrm{Pr}^{1/3}}\right)^2 \tag{4.8}$$

Finally, assuming Pr = 1 and Le = 1, and neglecting the numerical constants the last equation simplifies to:

$$L_f \sim \frac{1}{V_g \alpha_g}\left(\frac{s\rho_s V_f \tau}{\rho_g y_O}\right)^2 \tag{4.9}$$

The flame length in this case depends on the flame spread rate V_f, and is inversely proportional to V_g. The closed-form solution of flame spread rate in the thermal regime for thin fuels is not expected to satisfy Eq. 4.9, because by definition it does not consider kinetic effects. However, we can substitute it in Eq. 4.9 and use it to normalize the experimental flame lengths over a *thermal* flame length:

$$L_{f,\mathrm{th}} \sim \left(\frac{sF}{y_O}\right)^2 \frac{\lambda_g c_g}{\rho_g V_g c_s^2} \tag{4.10}$$

Both Eq. 4.9 and 4.10 show a decrease of L_f with flow velocity; Eq. 4.9 depends also on the product $V_f \cdot \tau$, which is assumed constant in the thermal regime. Figure 4.16 compares the values of experimental flame length (symbols) and the ones predicted by Eq. 4.9 with experimental V_f (dashed lines, with the same color of the reference thickness), normalized with $L_{f,\mathrm{th}}$. The values from Eq. 4.9 multiplied by a constant of 0.1 agree well with experiments at high velocities, but overestimates the values at low V_g because $\delta_T \to \infty$ when $V_g \to 0$. The value of $L_{f,\mathrm{th}}$ is multiplied by 0.03 to match the flame length of the 2 mm samples in downward flame spread. The thinner fuels show similar values of $L_f/L_{f,\mathrm{th}}$ at $V_g = 0$ cm/s and $V_g = 60$ cm/s. At higher velocities, in contrast, they diverge from $L_{f,\mathrm{th}}$ with a similar slope. This divergence could be attributed to the effects on finite-rate kinetics on flame spread.

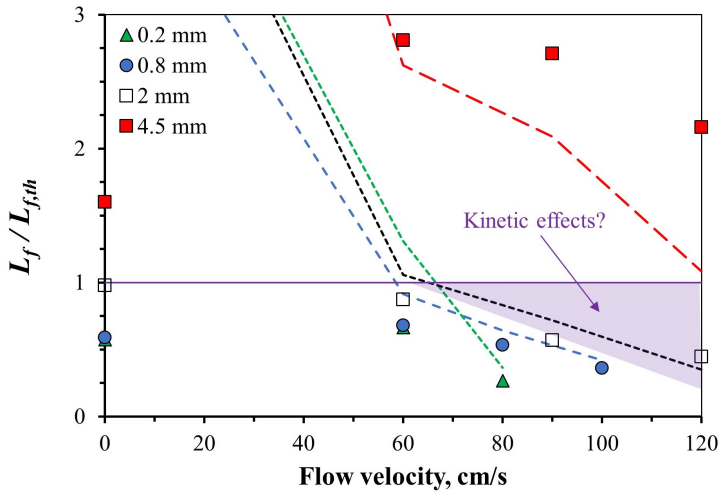

Figure 4.16: Experimental flame lengths are normalized with the thermal flame length from Eq. 4.10. The dashed lines correspond to the calculated values according to Eq. 4.9 by using experimental values of V_f.

4.5 Burn Angles in the Kinetic Regime

The fuel burning rate has been theoretically analyzed by Emmons [68] as discussed in the previous Chapter. In his similarity solution, Emmons assumed a non-spreading flame and neglected the development length x_d so that he could use similarity between flow velocity and coupling function fields, along with the flame sheet approximation and a constant surface temperature. A surface energy balance produced a closed-form analytical expression for the average burning rate as [107]:

$$\dot{m}''_{\text{avg}} = \rho_g V_g \left[-f(0)\right] \sqrt{\frac{2}{\text{Re}_L}} \tag{4.11}$$

Where the Reynolds number is based on free stream velocity and length of the vaporization zone, and $-f(0)$ is the value of the Blasius function at the surface, which can be expressed in terms of the mass transfer number B and numerically solved. The term $-f(0)$ goes from 0 for $B = 0$ to an asymptotic limit of 1.238 for $B = \infty$ (when the boundary layer is blown away) [107, 108]. For a more practical range of B (1 through 10), the increase is logarithmic.

Obviously, the similarity hypothesis used by Emmons between velocity and coupling function boundary layers (energy and species equations combined) breaks down if the boundary layer has a non-zero development length, i.e., $x_d \gg 0$. Recently, Li et al. [109] explored the effect of the development length with an impermeable plate in front of the flame, showing how the flame location inside of a boundary layer affects its characteristics. However, a creeping flame spread over the surface introduces another complication for a similarity solution.

In Chapter 3 we introduced the burn angle as a competitive mechanism between flame spread and regression rate, and used it to indirectly calculate mass burning rates. It is interesting to explore how the flow velocity affects the burn angle formation. By approaching the problem with scale analysis we will investigate the conditions under which the burn angle varies, establishing qualitative correlations between spread and regression rates under the effects of flow velocity, fuel thickness and other burning parameters.

4.5.1 Scale Analysis: an Alternative *B* Number

Most of the heat transferred from the flame to the fuel surface is absorbed by the solid for its vaporization. The radiative loss from the surface and a radiative gain due to incident gas radiation have a cancelling effect, and it can be shown that except for very low V_g, possible only in a microgravity environment, radiation terms become small relative to gas to surface conduction $\dot{Q}''_g$ [6]. An energy balance at the pyrolyzing surface, therefore, produces:

$$\overline{\dot{m}}'' \Delta h_v^\circ \sim \dot{Q}''_g - \dot{Q}''_s \tag{4.12}$$

where $\overline{\dot{m}}''$ is the mass vaporization rate averaged over L_p, and Δh_v° is the enthalpy of vaporization at T_v. Assuming that $\dot{Q}''_s$, the heat conducted to the interior, is used to heat up the solid to its vaporization temperature T_v, Eq. 4.12 can be simplified by substituting $\dot{Q}''_s \approx \overline{\dot{m}}'' c_s \left(T_v - T_\infty\right)$ and defining an effective heat of vaporization as:

$$\Delta h_v \sim \Delta h_v^\circ + c_s \left(T_v - T_\infty\right) \tag{4.13}$$

Substituting Eq. 4.13 in Eq. 4.12, and expressing the gas to surface conduction in terms of the flame stand-off distance δ_T, Eq. 4.12 can be rewritten as:

$$\overline{\dot{m}}'' \Delta h_v \sim \lambda_g \frac{T_f - T_v}{\delta_T} \tag{4.14}$$

Furthermore, we can assume that the flame stand-off distance scales with the thermal boundary layer thickness that starts developing from the flame leading edge and is embedded in the velocity boundary layer. It can be shown that the slenderness of the thermal layer is related to the square root of the Reynolds number based on the effective flow velocity V_{eff} seen by the flame [110]:

$$\frac{L_p}{\delta_T} \sim \text{Pe}_L^{1/2}; \qquad \text{with} \qquad \text{Pe}_L = \frac{V_{\text{eff}} L_p}{\alpha_g} = \text{PrRe}_L \tag{4.15}$$

With Pe_L being the Pecklet number. Substituting δ_T from Eq. 4.15 into Eq. 4.14, after some algebra the

expression for the average mass vaporization rate reduces to:

$$\overline{\dot{m}}'' \sim \rho_g V_{\text{eff}} B' \sqrt{\frac{1}{\text{Re}_L \text{Pr}}}; \qquad \text{where} \qquad B' \sim \left[\frac{c_g\left(T_f - T_v\right)}{\Delta h_v}\right] \tag{4.16}$$

This result from scaling theory has a similar form of Emmons' exact solution given in Eq. 4.11. B' represents the driving force for mass transfer, and can be interpreted as the B number; however, how does the quantity B' represent the Blasius function at the surface $-f(0)$?

Using the standard properties listed in Table A.1 for the burning of PMMA in an oxygen-nitrogen mixture and using the online thermodynamic calculator n-IG Combustion Calculator [111], the adiabatic flame temperature is calculated for different oxygen mass fractions. By using Eq. 4.13 to calculate the effective enthalpy of vaporization, B' is calculated and plotted in Fig. 4.17, as well as the B number used by Emmons:

$$B = \left[\frac{\Delta h_c^\circ\left(x_{\text{Ox},\infty}/s\right) - c_p\left(T_v - T_\infty\right)''}{\Delta h_v^\circ + \dot{Q}_s''/\dot{m}_{\text{avg}}}\right] \approx \left[\frac{\Delta h_c^\circ\left(x_{\text{Ox},\infty}/s\right) - c_p\left(T_v - T_\infty\right)}{\Delta h_v}\right] \tag{4.17}$$

Although B' from Eq. 4.16 does not exactly reproduce B, we see the similar trend of the number increasing with oxygen level. Aside from very high oxygen level, B' reasonably represents the driving force for mass transfer.

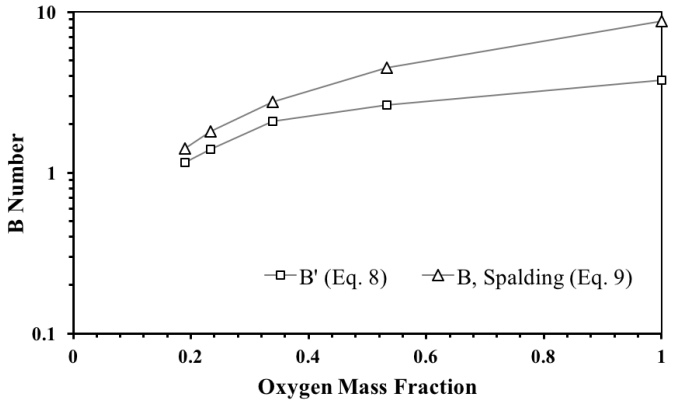

Figure 4.17: B number from Spalding's formula for droplet combustion (which is also used in Emmons' solution) and the proposed formula.

The B number can also be obtained from the conserved scalar $(x_F - x_O/s)$, where s is the oxygen-fuel mass stoichiometric ratio and x_F and x_O are respectively the mass fractions of fuel and oxygen, producing an expression for B_m:

$$B_m = \frac{x_{F,w} + x_{O,\infty}/s}{1 - x_{F,w}} \tag{4.18}$$

Equating B_m with B' in Eq. 4.16, produces an approximate expression for the mass fraction of fuel at the vaporizing surface:

$$x_{F,w} \approx \frac{c_g\,(T_f - T_v) - \Delta h_v x_{O,\infty}/s}{c_g\,(T_f - T_v) + \Delta h_v} \tag{4.19}$$

The fuel mass fraction, according to Eq. 4.19, is now a thermodynamic quantity just like the adiabatic flame temperature, and they are both plotted in Fig. 4.18 using the property values listed in Table A.1. Unlike the flame temperature, the wall mass fraction of the fuel seems to reach an almost asymptotic value of about 0.65 for an oxygen mass fraction of 0.4 and thereafter does not change much with the oxygen level.

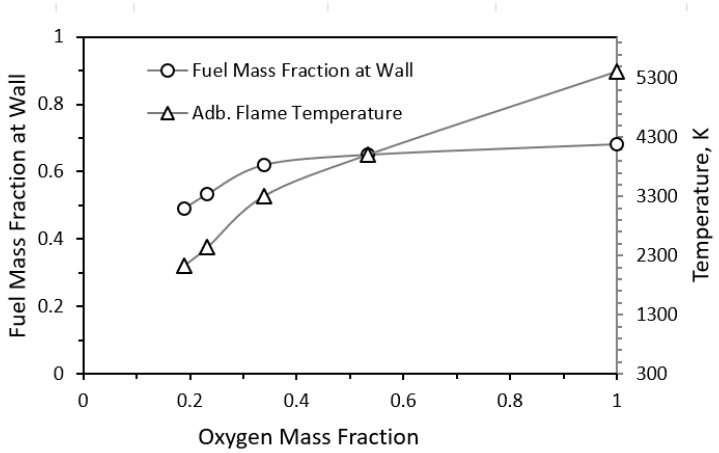

Figure 4.18: Fuel mass fraction of the wall and the adiabatic flame temperature as a function of the oxidizer oxygen mass fraction.

In the scale analysis of heat or mass transfer, we assume a linear variation of the conserved variables perpendicular to the burning surface. However, blowing from the surface makes the conserved profiles exponential rather than linear, reducing the diffusive flux. This linearization, which is also used in de Ris' exact solution [47], enhances the mass transfer by a factor of $B/\ln(1+B)$ for droplet vaporization and combustion. If we use the inverse of this factor to correct for the artificial amplification of vaporization rate due to linearization, Eq. 4.16 becomes:

$$\overline{\dot{m}}'' \sim \rho_g V_{\text{eff}} \ln(1+B') \sqrt{\frac{1}{\text{Re}_L \text{Pr}}} \tag{4.20}$$

A comparison among $-f(0)$, B', and $\ln(1+B')$ is made in Fig. 4.19 for the entire range of oxygen mass fraction (19% through 100%). Use of B' instead of $-f(0)$ as the driving force understandably over-predicts the blowing effect by a factor of 2.7 at 19% oxygen level through a factor of 5.3 at 100%. Also

$\ln(1+B')$ over-predicts the blowing, but by a factor of 1.83 through 2.2 for the same range. In fact, as can be seen from the plot (filled circles), a constant coefficient of 0.35 in front of $\ln(1+B')$ captures the exact solution quite effectively.

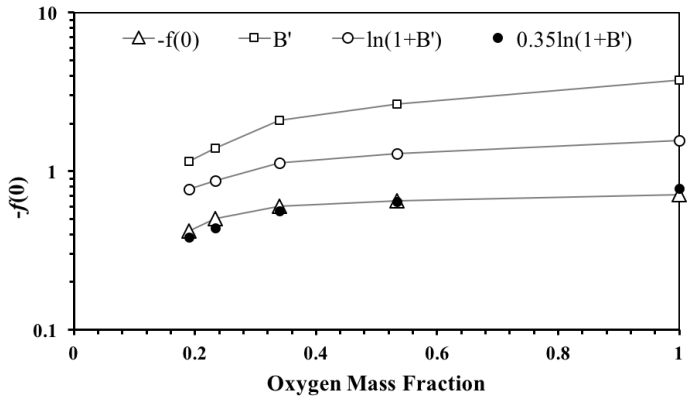

Figure 4.19: Contribution of the mass transfer driving force: Emmons' exact solution vs. scaling (Equations (2) and (12)).

Equation 4.20 multiplied by coefficient (presumably about 0.35) reproduces the Emmons' expression (Eq. 4.11) when the development distance is set to zero and Prandtl number is assumed to be 1 (as assumed by Emmons). But Eq. 4.20 offers several advantages over Eq. 4.11: the mass transfer number B' obtained from scaling is much easier to evaluate compared to the exact expression for B_h, there is no need to obtain a numerical solution for $-f(0)$, and use of the effective velocity allows correction for a developing boundary layer in front of the advancing flame. Furthermore, it should be noticed that the B-number has been used in the past as a constant boundary condition at the wall, but to better describe the problem Rangwala [70] and Torero et al. [71] proposed a variable B-number based on the flame stand-off distance. The variation of the stand-off distance in our model is included by considering the effective velocity V_{eff} and therefore B' is a constant depending on the burning conditions.

To explore the parametric dependence of the burn angle introduced in Chapter 3 we can use an analytical expression for the spread rate. We choose the linearized expression of Eq. 4.16, obtained directly from scaling without the correction factor. While it makes the expression less accurate, it exposes the parameters of the problem explicitly. It should be noted that de Ris also neglected this correction factor in obtaining the flame temperature in his seminal work. Starting from the mass balance (see Fig. 4.1) and the burn angle definition $\sin\beta = \tau/L_p$ and Eq. 4.16, we obtain:

$$\sin\beta \sim \left(\frac{\lambda_g \rho_g}{\rho_s^2 c_g}\right) B'^2 \left(\frac{V_{\text{eff}}}{\tau V_f^2}\right) \tag{4.21}$$

If a flame slows down, i.e. the spread rate decreases, the burn angle will increase, suggesting that the

flame will try to burn the cross-sectional fuel before proceeding further along the surface. The dependence of the burn angle on the effective velocity expressed by Eq. 4.21 changes based on the burning regime; in the thermal regime, for example, V_f for thin fuels mainly depends on fuel thickness and not on flow velocity, implying that the burn angle increases with V_{eff} and decreases with τ. However, V_f decreases with flow velocity when the flame enters in the kinetic regime, both for thin and thick fuels, so the effect of V_{eff} could dominate over the thickness dependence. On the other hand, a higher V_g is beneficial in the radiative regime, and could cause an decrease in the burn angle if the flame spreads faster.

The effect of ambient pressure on Eq. 4.21 can be estimated through the dependence on the gas density; by looking at Eq. 3.1 and 3.2 in the thermal regime, for example, the burn angle is linearly dependent on pressure for thin fuels and inversely proportional for thick fuels.

The influence of oxygen concentration is mainly controlled by the spread rate V_f and its dependence on the flame temperature. In general, we expect lower oxygen concentrations to slow down the flame, causing the burn angle to increase. This conclusion is qualitatively supported by the cone angle measurement of the 12.7 mm thick cylinders tested at three oxygen levels by Sibulkin and Little [85]; from the photographs of their Fig. 2, the cone angles are respectively 7.9°, 17.7° and 41° when the oxygen mass fraction is 0.232, 0.217 and 0.206 (corresponding to volumetric fraction of about 0.21, 0.195 and 0.185).

The experimental results presented in the previous section can be compared to Eq. 4.21. The experimental values of V_g refer to the forced flow velocity, and they can be converted to effective velocities according to Eq. 4.4. Experimental results are compared to Eq. 4.21 in Fig. 4.20 by using de Ris' spread rate formula for thin fuels and parameters from Table A.1. The experimental results show a linear increase of $\sin\beta$ with the effective velocity in the range 10 - 30 cm/s, in agreement with Eq. 4.21, although the latter overestimates the effect of fuel thickness. It should be noticed that at higher effective velocities the experimental results show burn angles larger than 90°, suggesting the presence of regressing flames like the ones observed by Huang et al. [86]. These flames cannot burn at high velocities, in analogy with the blow-off extinction over thin fuels observed at effective velocities of about 30 cm/s. In these conditions, flames are likely affected by kinetics effects and the experimental results are not well described by the thermal regime.

Chapter 4, in part, has been published on the Fire Technology Journal (L. Carmignani, G. Celniker, S. Bhattacharjee, The effect of Boundary Layer on Blow-Off Extinction in Opposed-Flow Flame Spread over Thin Cellulose: Experiments and Simplified Analysis, Fire Technol. 53, pp. 967-982, 2017) and other parts are extracted from (L. Carmignani, O. Kaskir, E. Tagger, S. Bhattacharjee, S., Connecting Burning Rate and Flame Spread Rate in Opposed-Flow Flame Spread over Flat Fuel Beds, 11th U.S. National Combust. Meeting, Pasadena CA, March 24-27, 2019). The thesis author was the primary investigator in

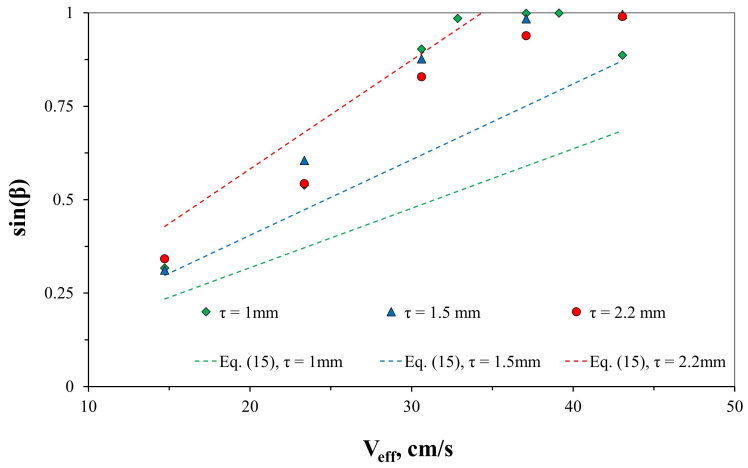

Figure 4.20: Variation of the burn angle with effective velocity as described by Eq. 4.21 by assuming a thin fuel. The influence of the effective velocity is compared to the experimental results.

these publications. Parts of Chapter 4 have also been published in Combust. Theory and Modelling (S. Bhattacharjee, L. Carmignani, Burn angle in forced and natural convection: a simplified scaling approach, Comb. Sci. Modelling 23, pp. 956-968, 2019), of which the dissertation author was among the primary contributors in these papers.

Chapter 5

The Radiative Regime

5.1 The Microgravity Environment

In the previous Chapter we have seen how the boundary layer affects the velocity gradient experienced by the flame, with consequences on flame spread and extinction in the kinetic regime. The lowest velocity considered so far is the buoyant velocity, which is naturally driven. In microgravity, on the other hand, the buoyant flow generated by a flame can be almost completely suppressed by reducing the forced flow velocity to zero. In this case the residence time, and therefore the Damköhler number, become large. Therefore, the importance of flame radiation can drastically increases despite the small size of the flames [40], since the characteristic radiation time for gas and solid phases becomes comparable to the increased residence time. The radiation time can be defined as the time needed to radiate away all the energy produced by combustion:

$$t_{\mathrm{rad}} \sim \frac{\rho_g x_F \Delta h^\circ}{4\varepsilon_g \sigma \left(T_f^4 - T_\infty^4\right)} \tag{5.1}$$

In analogy with the Damköhler number, the ratio between t_{res} and t_{rad} is inversely proportional to the flow velocity V_g. A higher ratio increases the importance of radiation losses, suggesting the name of radiative regime. This ratio, however, depends on several burning conditions.

Oxygen and pressure effects have been studied in microgravity in the 1990s with the Solid Surface Combustion Experiment (SSCE), where thin cellulosic and PMMA samples were tested in a quiescent environment. Bhattacharjee and Altenkirch [112], and later Ramachandra et al. [113], analyzed the flame spread over thin cellulosic fuels at oxygen levels of 35 and 50%, with pressures of 1, 1.5 and 2 atm, to understand the role of gas and surface radiation in the radiative regime. They concluded that the flame leading edge

was stable and reached steady conditions, and they noticed that higher oxygen and pressure levels produced brighter flames with the formation and growth of the yellow region of the flame. Despite the high oxygen levels (up to 70% by volume), experiments with thick PMMA samples showed an unstable flame behavior with eventual extinction [114], as captured by numerical results that identified radiation losses as the cause [42]. Conductive losses through the sample holder due to the small sample size (59.9 mm long, 3.18 mm thick and 6.35 mm wide), however, might have played a role in flame extinction.

In the BASS experiments, flames over PMMA extinguished as soon as the forced flow was suppressed, and radiative losses strongly influenced flame spread also at low velocities [18].

Due to the importance of the velocity gradient in the kinetic regime, it is interesting to evaluate its influence in microgravity. In this Chapter, we will compare numerical results to the BASS experiments to evaluate the effect of a developing boundary layer. We will also investigate the effects of burning conditions on flame radiation. Finally, the comparison between SSCE and BASS experiments reveals that also fuel geometry could play a role in the radiative emissions of a flame. A scale analysis is used to consider the case of a completely quiescent environment.

5.2 Boundary Layer Effect in the Radiative Regime

Previous microgravity experiments showed that flow velocities below a critical value cause the flame to extinguish [115]. This quenching velocity in the radiative regime is the counter part of the blow-off velocity in the kinetic regime. If the boundary layer in the kinetic regime has such a significant effect on blow-off extinction, the question naturally arises as to if it also affects flame spread in the radiative regime in a similar manner. In this section we present numerical results to explore how the spread rate and flame structure are affected in a low-velocity regime. The results are compared to the BASS experiments.

5.2.1 Numerical Results

In our steady-state model, the fuel is fed to the flame, allowing any desired length of the boundary layer development zone. Spread rates calculated for thin PMMA sheet (0.1 mm thick) with air flowing over a wide range of opposing flow velocities are shown in Fig. 5.1 for two different development lengths, $x_d = 20$ and $x_d = 60$ mm. In the kinetic regime (small Damköhler number), the spread rate keeps decreasing with V_g until blow-off extinction occurs. The development length clearly has a strong impact on spread rate the blow-off extinction velocity, increasing from 55 cm/s to 111 cm/s as x_d is increased from 20 to 60 mm. As the flow velocity is reduced, the radiative regime sets at about $V_g = 20$ cm/s and the spread rate starts decreasing leading to radiative extinction. However, in contrast with the kinetic regime, the development

length seems to gradually have less impact; the quenching velocity only slightly changes from 1 cm/s to 1.5 cm/s as x_d is increased from 20 to 60 mm.

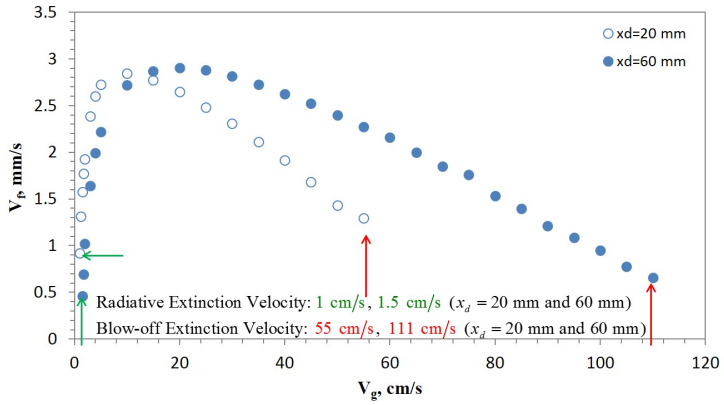

Figure 5.1: Computed spread rate as a function of opposing flow velocity for two different development lengths.

Two flame shapes (temperature contours) are shown in Fig. 5.2 for the same development lengths considered in Fig. 5.1. To understand the effect of the boundary layer on the flow near the leading edge in the radiative regime, the axial velocity profiles at the flame leading edge for a free stream velocity of 5 cm/s are shown in the same figure below the computed flames. The boundary layer thickness is defined as 99% of the local maximum of gas velocity. From the velocity profiles, it can be seen that the boundary layer is almost twice as thick for $x_d = 60$ mm. Even though the free stream velocity is 50 mm/s, the actual flow velocity at the leading edge of the flame at a height of the diffusion length, $L_g = 1.8$ mm, is only 6.9 mm/s for $x_d = 60$ mm, which increases to 17.3 mm/s for $x_d = 20$ mm. The flame leading edge is clearly deep inside the boundary layer with L_g/δ decreasing with an increase in x_d. The flame strengthens as indicated by its size and flame temperature as the development length is reduced and the flame encounters a higher effective velocity. The increase in spread rate is relatively mild, from 2.3 to 2.7 mm/s.

The experimental conditions of analogous BASS experiments (forced flow velocity, thickness and oxygen level) were numerically reproduced to compare the results. In the BASS experimental matrix the flow velocity was often changed during the experiments to maximize the range of burning conditions; unfortunately, this limited the distance (and x_d) covered by a flame with a constant forced velocity. The effect of development length on computed and experimental flame spread rates, whose values are indicated respectively by empty and filled symbols, is plotted in Fig. 5.3 for three values of opposed flow velocity. The spread rate can be seen to decrease with V_g consistently with the radiative theory of flame spread [115]. With a decreasing flow velocity, the residence time monotonically increases until it is comparable to radiation time scale, ushering in radiative quenching. For a given V_g, Fig. 5.3 also shows that the spread rate increases as

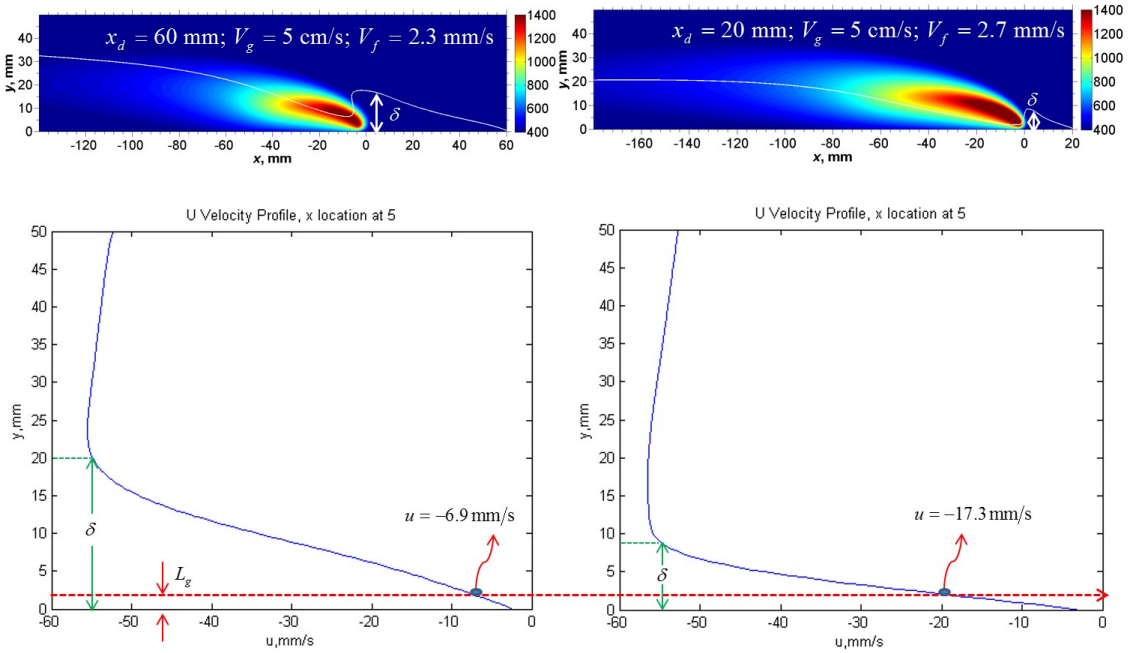

Figure 5.2: Computed flame shape and velocity profile at the leading edge for two different development lengths.

the flame advances along the sample.

By isolating the case of 0.1 mm thick PMMA burning against $V_g = 3$ cm/s, numerical temperature profiles are compared in Fig. 5.4 to pictures of the experimental flames' front view (on the right). The oxygen level is these experiments (labeled B6 and B1, see Table A.2) are 21% and 22.2%, respectively. Despite the different views of numerical and experimental flames in Fig. 5.4, flame length and spread rates can be compared. Simulated flame shapes clearly indicate a weakening flame when x_d increases, as shown also by flame length variations, and this trend is qualitatively confirmed by the experiments on the right side of Fig. 5.4. Flame length values in Fig. 5.4 were measured with FIAT for the experimental flames, whereas for the simulated flames they were obtained by locating points along the x-axis corresponding to a threshold temperature (±10 K). The temperature was estimated with the aim of matching the experimental results. In the case of $V_g = 3$ cm/s the temperature considered for the flame length was about 730 K, while in the case of $V_g = 5$ cm/s, the temperature was significantly higher, at about 1000 K. The lower temperature for $V_g = 3$ cm/s can be justified with the lower level of oxygen available for the reactions. Furthermore, smaller flame length for lower V_g or higher x_d is accompanied by a reduction in the maximum flame temperature and spread rate; for example, at $x_d = 60$ mm, the maximum flame temperature is 1553 K for $V_g = 5$ cm/s, and 1370 K for $V_g = 3$ cm/s, while the spread rate goes from about 2.5 to 1.71 mm/s.

The spread rate of the two experiments represented in Fig. 5.4 is on the order of 2 mm/s, and there is a little increase along the sample as indicated by the computational results, but the span of boundary layer

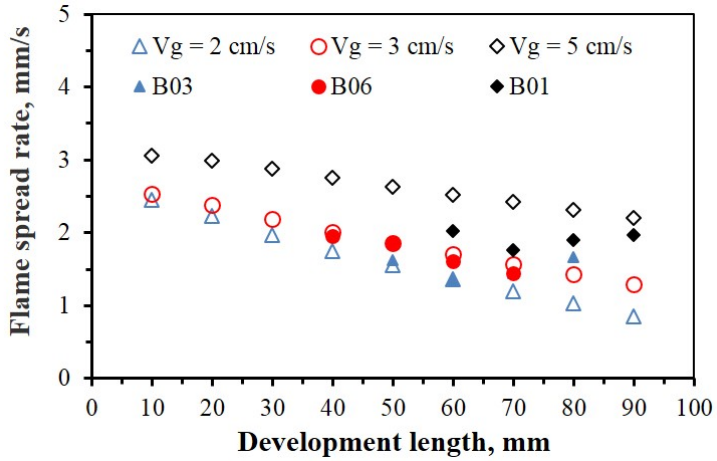

Figure 5.3: Computed (empty symbols) and experimental (filled) flame spread rate vs. development length of boundary layer for three different flow velocities.

distance covered is too low to make an experimental case. However, flames in the opposed-flow configuration react pretty fast to local velocity changes in microgravity [2], and the flame length seems to be an easier parameter to analyze.

To explore how the flame length changes with x_d, a larger set of experimental test matrix was used. Isolating the portion of the experiments where the flow velocity was fixed at 5 cm/s (and same fuel width of 20 mm and oxygen level of 22%) over different sample thicknesses, the data plotted in Fig. 5.5 (experiments B1, B5, and B4) clearly indicate that flame length increases with the flame getting closer to the sample leading edge (decrease in x_d). Near the ignition point, flames seem to be slightly shorter for thicker fuels, but there seems to be little thickness effect as x_d decreases, at least in the flame length growth rate. One possible explanation for this thickness dependence of flame length is that thicker fuels take a longer time for their pyrolysis front to reach steady-state condition. It is interesting to notice how the flame length growth rate is similar for different thicknesses initially, even though the absolute lengths still depend on thickness in analogy with the results from Sec. 3.4. It seems also that the thickness effect becomes smaller reducing the development length, suggesting that the flame length is controlled by the opposed-flow velocity and boundary layer for very low development lengths. To explore how the flame length varies with x_d as the opposed flow velocity, data from three tests — B3, B6, and B1 — are isolated and the flame lengths calculated for three different values of velocity (respectively 2, 3, and 5 cm/s) are plotted in Fig. 5.6. Once again the data confirm that the flame length decreases with an increase in x_d for each V_g; however, there is a clear trend that for higher flow velocity the flame length is slightly larger. This is exactly what can be observed in the simulated flames of Figure 5.4, where the flame length increases when the flow velocity is increased from 2 cm/s to 3 cm/s, because of the higher mixing of oxidizer and reactants.

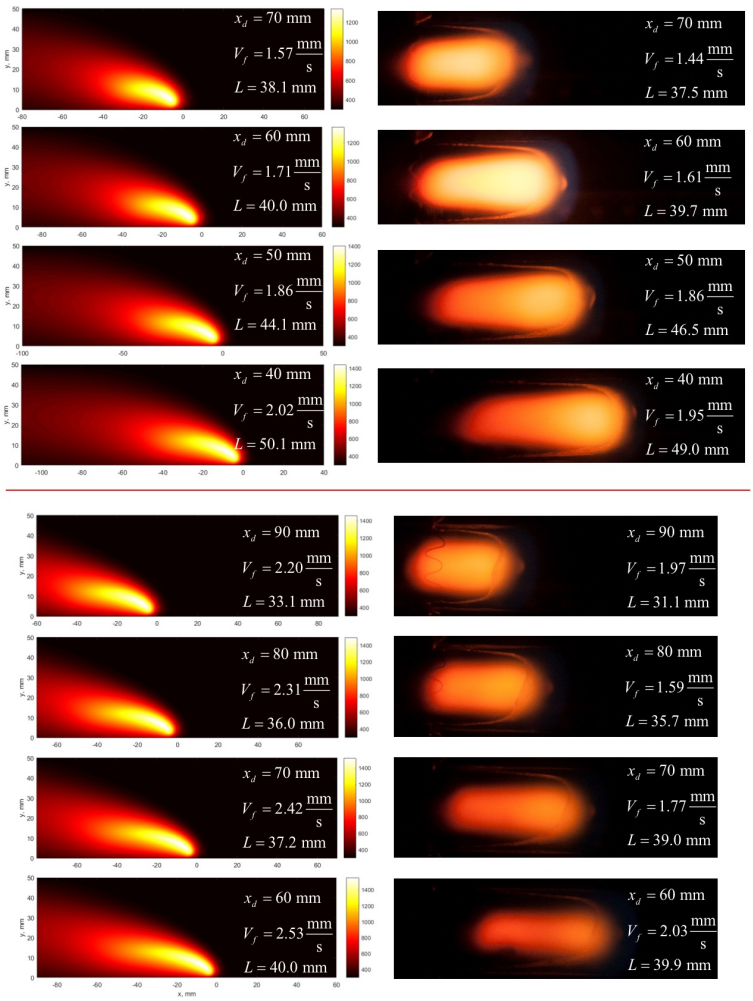

Figure 5.4: Computed flames (on the left, side-view) and pictures from experiments (on the right, frontview), representing B6 (above red line) and B1 (below red line) tests, where the thickness of PMMA was 0.1 mm and the flow was respectively 3 cm/s and 5 cm/s.

Defining the conduction time scale in the solid phase as $t \sim \tau^2/\alpha_s$, in the set of experiments considered it goes from about $2.32 \cdot 10^{-2}$ s for a thickness of 0.1 mm to 0.37 s for 0.4 mm. This time scale is much smaller than the gas-phase time scale, $t \sim L_g/V_f$, which is in the order of 1 s considering a preheat length $L_g \approx 2$ mm and $V_f \approx 2$ mm/s. Therefore, according to existing models where flame spread rate is governed by heat conduction in the condensed phase [12, 116], the flame leading edge reaches steady-state during the experimental time considered, which was between 15 s and 40 s. This time scale comparison suggests that the evolution of flame length and spread rate discussed above occurred in pseudo-steady conditions, where the changes are affected by a varying velocity gradient rather than thermal inertia.

The strengthening of a flame as x_d decreases is consistent with the experimental findings. It should be noted that, while the radiation computation includes the three-dimensional domain (through side losses), the CFD is completely 2D and side losses or diffusion in the width-wise direction are neglected. The side-wise

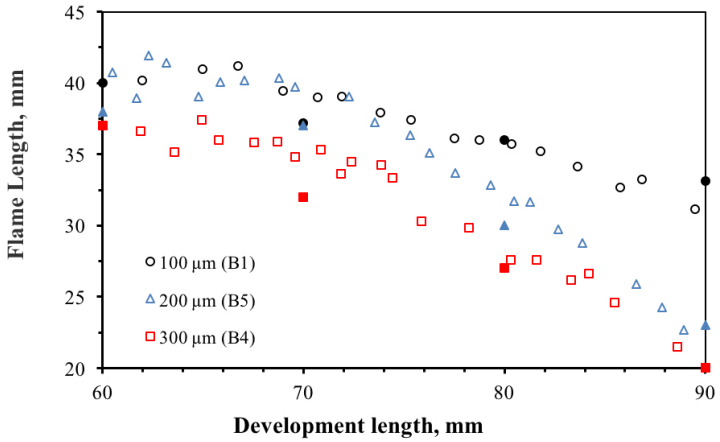

Figure 5.5: Experimental results (B1, B5, B4) showing fuel thickness effect on the dependence of flame length on the development length. Flow velocity is 5 cm/s. Filled symbols represent numerical results relative to the experimental conditions.

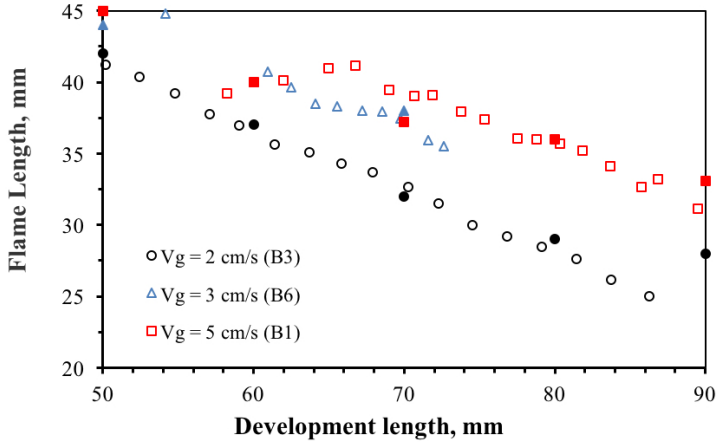

Figure 5.6: Experiments (B3, B6, B1) showing flow velocity effect on the dependence of flame length on the development length. Fuel thickness is 100 µm. Filled symbols represent numerical results relative to the experimental conditions.

losses (to the sample holder and ambient air) are expected to reduce the overall size of the flame and total radiation emitted by the flame. If the sample width is decreased, we would expect the flame to be cooler (due to increase in losses through the side as a fraction of heat produced) and its size to decrease. Flame shapes from two tests (B11 and B21) where the conditions are almost identical except for the sample width of 20 and 10 mm ($2\tau = 0.2$ mm, $V_g = 5$ cm/s, and oxygen level of 21 and 20.8%, respectively), are shown in Fig. 5.7. The flame clearly is much smaller when the width is halved. Also the radiometer peak signal drastically decreases from about 30 to 11 mV (after adjusting the raw radiometer data with the sensor gain). However, for both cases the flame length does show a similar increase rate of length as the development length decreases.

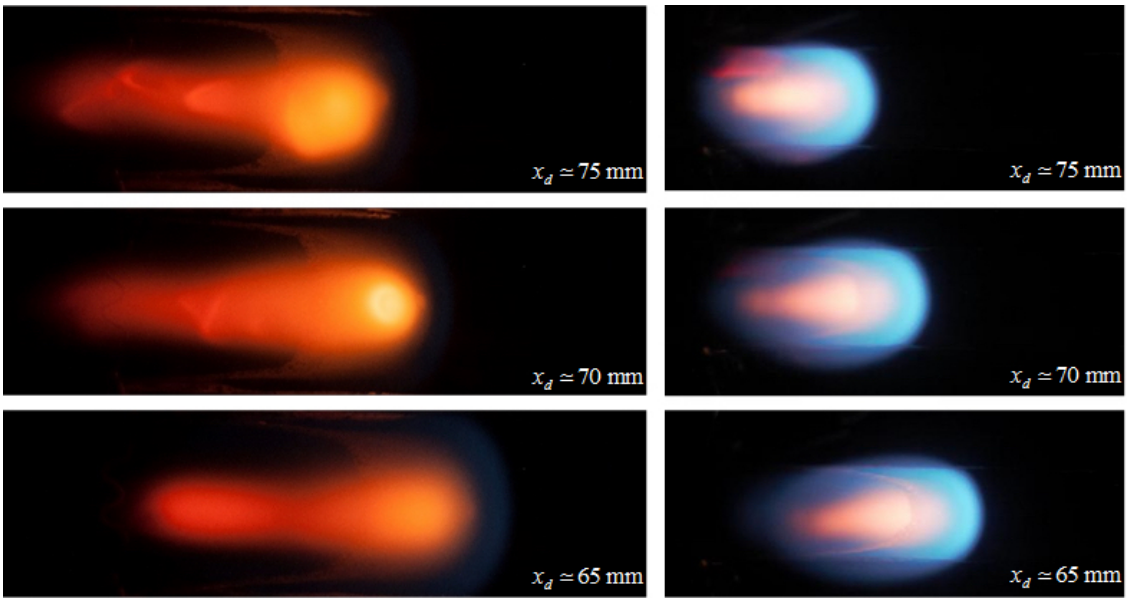

Figure 5.7: Front-view pictures of experiments with two different sample width: 2 cm (left side), and 1 cm (right side). Flame length clearly increases as the development length decreases.

5.3 Flame Radiation in Microgravity

Despite the importance of radiation in microgravity flames, direct measurements of radiation emitted by flames over solid fuels had never been measured before the BASS investigation. The experimental results from BASS have been used in several ways, but the variation of flame geometry (measured by projected area and length) with oxygen concentration, and the total radiation captured by the thermopile sensor have not been described.

Radiation measurements from the new microgravity experiments Saffire have been recently discussed by Urban et al. for solid fuels burning in a concurrent configuration [117]. However, the burning conditions in these experiments were fixed, and their influence on flame radiation is hard to determine.

Many factors contribute to the total flame radiation, e.g. flame area, presence of soot, gas and surface temperatures, pressure, etc. The presence of soot is expected to increase the radiative emission and can be estimated by measuring the yellow region of a flame [118, 119]. Indeed, there can be an excess of fuel in the central region of a flame, causing high soot concentrations. The sooty region in carbon-based fuels is often yellow-orange, and the radiative intensity of this region should be proportional to the soot volume fraction and flame temperature. Often, as in the case of PMMA, a dim blue zone can be identified along the outer contour of a flame, mainly given by luminescent radicals CH^*. The sooty region is much brighter than the blue zone, but the latter can be revealed by adjusting video settings. Flames close to extinction, both in normal gravity (Fig. 4.8) and microgravity, assume this blue color, suggesting lower flame temperatures.

In this section, we present total radiation data gathered from the BASS microgravity experiments as functions of opposed flow velocity, oxygen level, and fuel thickness. With image processing, we explore the variation of total and yellow regions of a flame (from the top view of the experiments) to describe the observed behavior of the emitted radiation. The experimental variables are reproduced numerically (neglecting soot formation) to further explore the importance of total radiation by varying the burning conditions.

5.3.1 Radiation Measurements

The FIAT analysis of the top-view video created from the BASS still images provides the evolution of the flame leading edge, spread rate, flame length, and flame areas (total and yellow) with respect to time. These information are matched with radiometer and anemometer data printed on the frames of the side-view videos to create the corresponding time profiles of radiation and opposed flow velocity. Since the flame spread rate can vary during the experiment (due to changes in opposed-flow velocity), the time profiles are converted to the relative location of the flame leading edges along the samples. The anemometer has a response time of approximately one minute [24], so the flow velocity adjustments were matched with the astronauts' vocal confirmations recorded during the experiments, whereas no time delay was considered for the radiometer.

An example of radiometer values obtained from the experiment B6 is given by the red squares in Fig. 5.8, which are read on the first frame of each second of the side video. These values are plotted along the sample, starting from the flame leading edge location when the igniter is turned off (see right pictures in Fig. 5.8). The total flame area was directly measured with FIAT, whereas the two-dimensional flame area was obtained by multiplying the flame length, independently measured with the intensity tracking method of FIAT, by the sample width of 20 mm; in this way it is possible to compare flame length and area. The first rise of the radiometer signal is accompanied by the initial growth of the flame. The values of the forced flow velocity are indicated by the red line in the plot of Fig. 5.8, and the increase in flame length could be associated to the varying velocity gradient encountered by the flame while spreading along the sample. The initial portion of the sample (0-40 mm) reflects the first 10-20 seconds of the experiment, where the flame is still growing. The position of the flame affects the solid angle described by the radiometer, but this effect could be small compared to the increase in radiative emission from a flame (the heated sample holder might have a role as well). By looking at the interval between 40 and 70 mm, the radiometer values are quite stable around 34 mV, while the 2D flame area increases by about 120 mm^2 (corresponding to a variation of about 6 mm in flame length) and the measured area oscillates between 400 and 600 mm^2. After the initial growth of the flame, measured and 2D flame areas seem to stabilize giving an almost constant radiometer measurement.

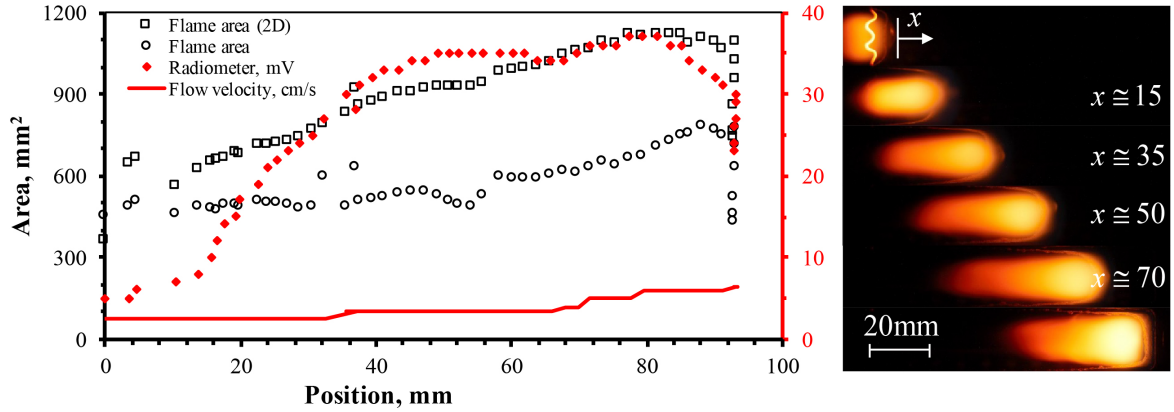

Figure 5.8: Radiometer and anemometer values read from the side video are shown in red corresponding to the right red axis for the flame spreading along the sample B6. The graph also shows the variation of flame area measured with the FIAT area tracking, and two-dimensional area (obtained by multiplying flame length by sample width), with values associated to the black left axis. On the right, still-pictures show the flame evolution with time intervals of 10 s, with the corresponding x position expressed in mm.

5.3.2 A Parametric Study of Burning Conditions

The three main burning conditions considered in this section are oxygen concentration, flow velocity and sample thickness. By selecting the experiments (or parts of them) where the ambient conditions are not varying (for at least 10 s), the radiometer signal (averaged over the time range with constant conditions) can be plotted as a function of each variable. For a better comparison, the averaged values are calculated when a flame is spreading over the central part of the sample ($x_d \approx 50$ mm); in this way changes in solid angles between flame and radiometer become minimal. Figure 5.9 shows the variation of experimental radiometer values (red symbols) with the three variables, with representative flame pictures on the right of each plot. Radiation values from the numerical simulations are reported in the graphs as well (black symbols) but will be discussed later. After an initial increase with flow velocity, flame radiation decreases with faster flows. The flame pictures show the initial growth sustained by higher velocities, as well as the final reduction in length and area. By keeping flow velocity and thickness constant and increasing oxygen concentration, the flame radiation shows a non-monotonic behavior, although the difference in radiometer values between 21 and 22% could be attributed to experimental uncertainties. The flame pictures show an increment in flame area when varying the oxygen from 17.4 to 22.2%, but the yellow region at 22.2% is actually smaller than at 21%. Although this could explain the experimental behavior of the radiometer, the number of data points are insufficient to confirm this trend. Finally, when oxygen concentration and flow velocity are constant

(bottom graph of Fig. 5.9), radiometer values increase by about 20% when a thicker sample is burnt. The pictures show larger flame lengths for thicker fuels, but with smaller yellow regions. Direct visualization of the experiments with 0.3 and 0.4 mm thick samples and their analysis suggest that these flames did not reach steady state in the limited experimental time and sample length.

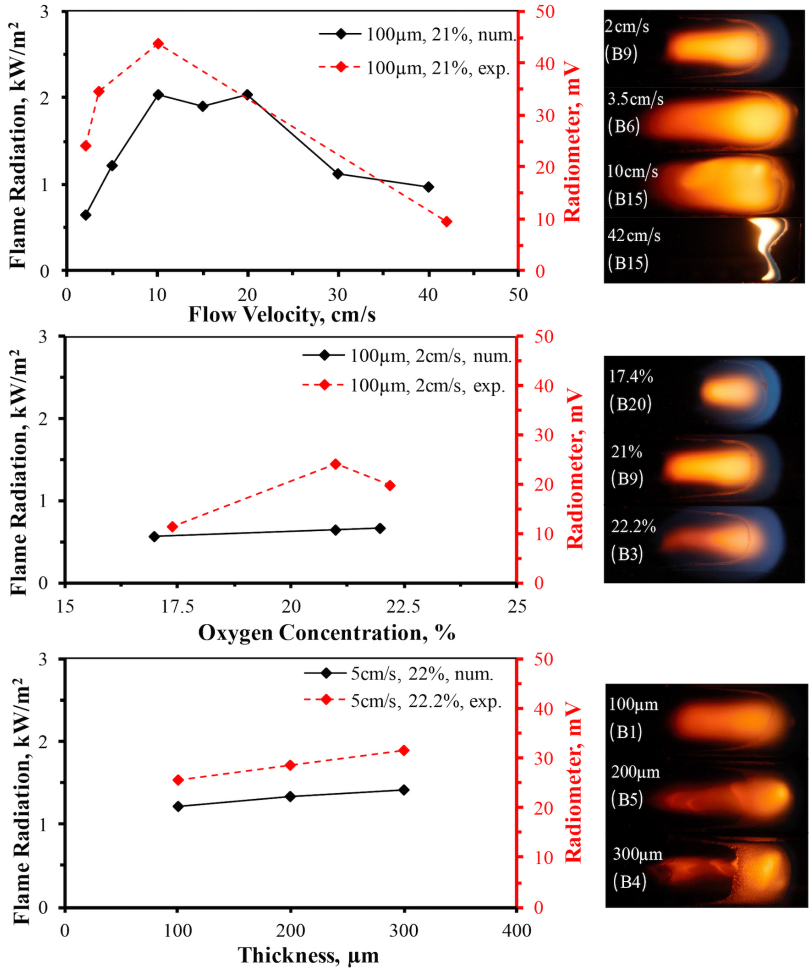

Figure 5.9: Radiometer signal read from the side videos (red symbols, dashed line) measured in mV, and from numerical simulations (black symbols, solid line). Flame radiation is plotted against flow velocity, oxygen concentration and thickness by isolating the experiments with two out of three variables being constant for at least 10 s.

The variation of yellow and blue flame with flow velocity and oxygen concentration is qualitatively shown in Fig. 5.10 for the 0.1 mm samples. The diameter of the circles in this figure reflects the ratio of yellow and blue areas. The flame pictures inside the graph show larger blue areas at low velocities (because of radiative losses) and oxygen concentration (lower flame temperature). The radiometer measurements of the relative flames are indicated next to the pictures. These values increase with flow velocity, with the flame being more vigorous, whereas there are no clear trends by varying oxygen concentration.

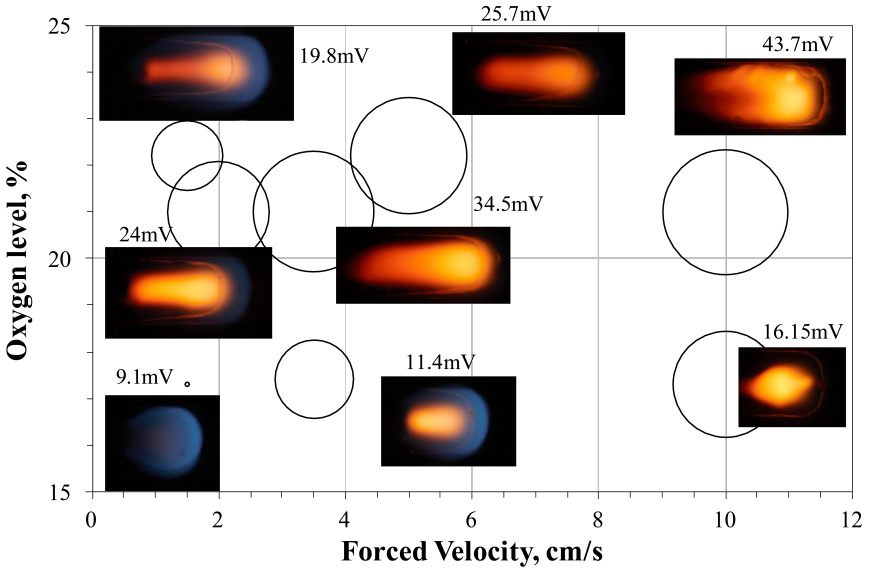

Figure 5.10: The diameter of the circles in the graph reflects the ratio of yellow and blue area of BASS flames over 0.1 mm thick samples. Examples of flames and their measured radiation are given for several burning conditions.

The pictures and radiometer values in Fig. 5.8 and Fig. 5.9 indicate how changes in flame geometry and burning conditions affect flame strength and radiation. The experiments offer important information regarding flame geometry, which we characterize by tracking flame length and area of the yellow region. Meanwhile, numerical results can provide variable distributions such as temperature fields. Experimental and numerical results are compared qualitatively by considering the flame length.

Figure 5.11 shows the evolution of simulated 2D flames (from a side view) with increasing flow velocity from 2 to 40 cm/s. The velocity values are similar to those of the experimental flames shown (from a top view) on the right of Fig. 5.11. When the forced flow was set to zero all the experimental flames extinguished within a few seconds, in agreement with the numerical results in a quiescent atmosphere with an oxygen concentration of 21 %. The simulated temperature fields show a stronger flame with higher flow velocity, meaning that the maximum flame temperature increases. However, the length of the 1200 K flame boundary (indicated by the blue contours in the simulated flames) first increases and then decreases, in the same way as the real flames. At 40 cm/s the flame gets closer to the solid surface and the hottest region shrinks significantly, as expected in the kinetic regime. The yellow regions on the right of Fig. 5.11 enlarge at higher velocities before shrinking again, and the increasing brightness suggests stronger flames. While a direct correlation between image color and temperature cannot be established, the similar trend between the experimental and numerical results enables the comparison between the two. It should be noticed that the flame at 42 cm/s looks similar to flames in normal gravity under similar conditions 4.8; still, this near-extinction flame is very bright and sooty. While kinetic extinction is driven by a lower residence time, the

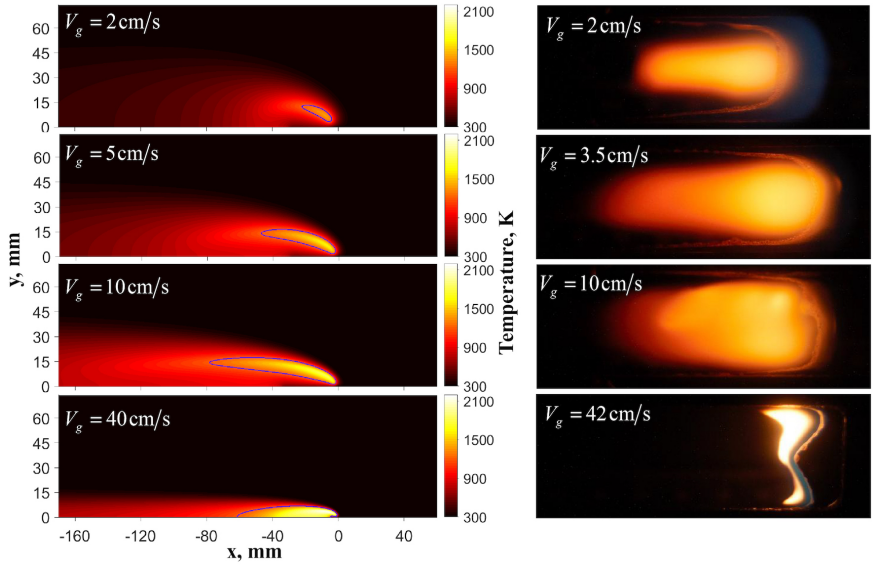

Figure 5.11: Comparison of simulated temperature fields (left) and top view of experimental flames (right) over 0.1 mm thick PMMA samples at 21% oxygen. The figure shows the effect of flow velocity on the temperature field inside of the domain and flame structure in the real flames.

chemical time is not changing and the flames can still be very hot. On the other hand, close to radiative quenching flames become cooler, suggesting the two different extinction mechanisms.

The total radiation of a flame, with contributions from gas and solid phases, is calculated numerically via the RADCAL method at a point in space analogous to the radiometer position in the BASS tunnel (see Fig. 2.5). The variation of the radiation per unit area is plotted in Fig. 5.9 to replicate the experimental conditions. When varying flow velocity, numerical radiation values follow the same trend as the experimental, although the curve presents a strange behavior between 10 and 20 cm/s. This oscillation is explained by the different maxima of gas and solid radiation, which do not occur at the same velocity. The increase in numerical radiation with oxygen concentration is mild with respect to the experimental values, whereas the thickness dependence has a similar slope to the radiometer values.

The fuel burning rate can be used to estimate the total flame radiation [120]. Obviously it could have not been directly measured in the BASS experiments, but it can be estimated by multiplying the mass balance of Eq. 3.11 by the sample width. The numerical model directly supplies the burning rates and, together with the experimental values, are plotted on the left graphs of Fig. 5.12 for the same range of burning conditions as in Fig. 5.9 (flow velocity, oxygen concentration and fuel thickness). On the third axis of the left graphs in Fig. 5.12 the numerical flame temperature is reported (defined as the highest temperature in the domain). Flow velocity has a similar effect on burning rates and radiative values in Fig. 5.9, despite the increase in flame temperature shown in the top graph of Fig. 5.12. Approaching the kinetic regime the

flame area is reduced, and radiation is weaker; however, at large V_g radiation losses are not relevant, and the flame temperature increases asymptotically to the adiabatic value. Numerical and experimental burning rates show the same trend despite the offset in values. Oxygen concentration is the variable in the second graph of Fig. 5.12 and, as expected, higher values are beneficial for both flame temperature and burning rates. The flame temperature does not depend on fuel thickness, as shown in the bottom graph of Fig. 5.12, because it is controlled by the gas phase. However, the burning rates and radiometer values increase with thickness in Fig. 5.9, in contrast with the results from thermal and kinetic regimes. Because of the different radiative contributions of soot content and flame temperature, the slower increase of the latter with respect to flame radiation at higher oxygen concentration and larger fuel thicknesses suggests that these flames produce more soot.

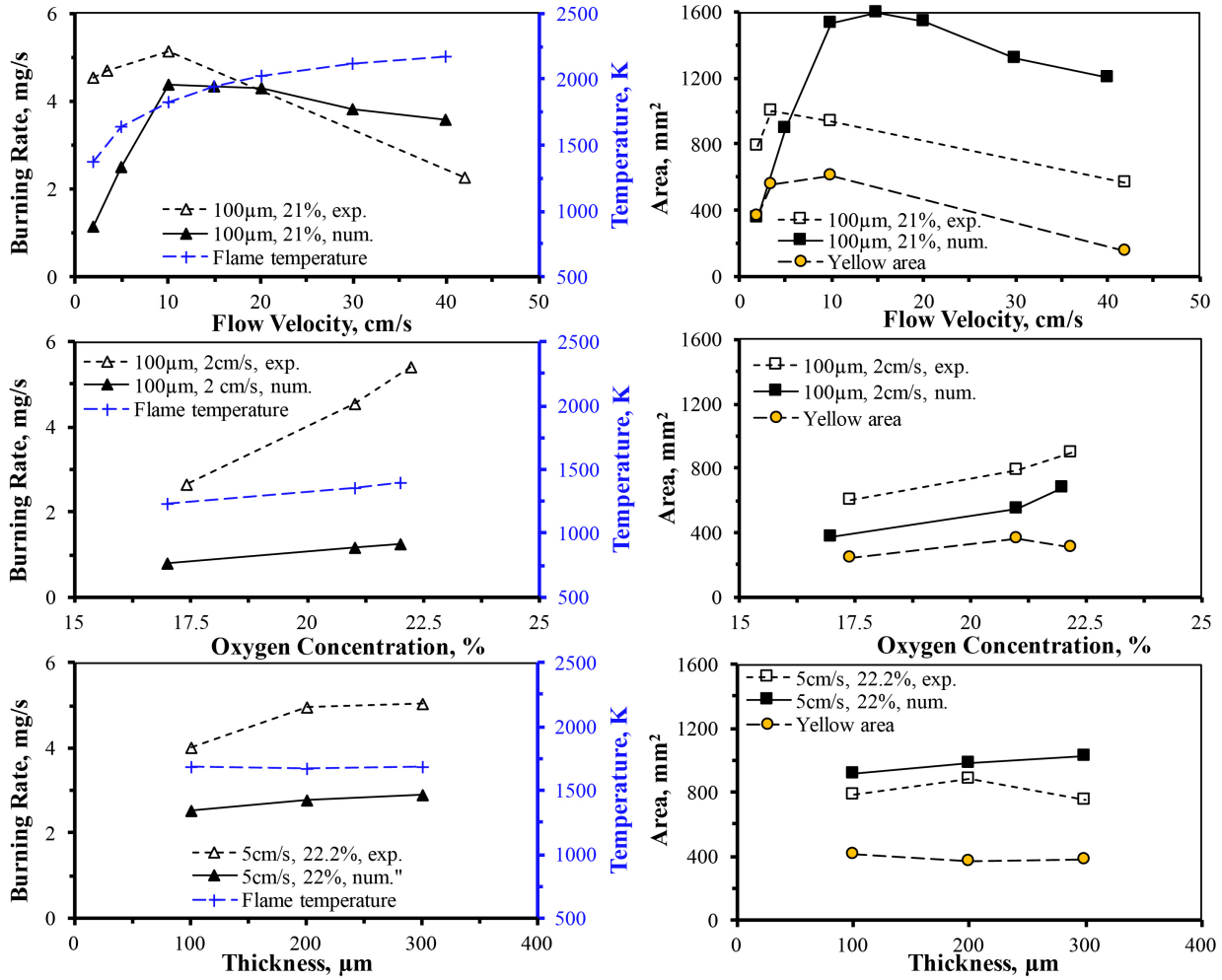

Figure 5.12: Parametric study of (left) burning rate and (right) flame area as function of flow velocity, oxygen concentration and fuel thickness. The numerical flame temperature is reported on the third axis of the left graphs.

The graphs on the right of Fig. 5.12 show the same parametric study on yellow flame areas and total

flame areas (obtained by multiplying flame length by sample width). Numerical values of flame length were multiplied by the sample width as well, and the calculated areas are indicated by filled symbols. The trends of flame areas with the three variables are very similar to the burning rate trends, and the offset between numerical and experimental values reduces except for flow velocity. The similarity between burning rates and flame areas suggest that the latter, easy to measure, could be used to measure the radiative intensity of small flames or when $\dot{m}$ is not available. The abnormal reduction in radiometer output for higher oxygen concentration in Fig. 5.9 could be justified by the smaller yellow flame measured in Fig. 5.12, but by looking at the bottom graphs showing the thickness dependence in Fig. 5.9 and Fig 5.12 we can see that the yellow area does not completely agree with the radiative strength of a flame. Also, from Fig. 5.12 we can see that in the range of variables considered, the yellow regions are mostly affected by flow velocity, and secondly by oxygen concentration but not fuel thickness. It should be noticed, however, that flames burning over thicker samples require more time to reach steady-state, making the thickness effect difficult to establish from the BASS experimental matrix (Table A.2). This is also suggested by the videos, where values of radiometer, flame length and area tend to increase monotonically throughout the experiments for thicker fuels.

5.4 An Extreme Case: The Quiescent Environment

5.4.1 Radiative Extinction

Bhattacharjee and Altenkirch investigated computationally the importance of gas-phase and surface radiation for thin fuels in the low flow regime in microgravity [40], and later compared them to the SSCE cellulosic fuels [112], concluding that surface radiation losses can lead the flame to extinction in a quiescent environment if the fuel thickness increases. These results were confirmed by the next missions of SSCE, where thick slabs of PMMA showed an unsteady flame spread with eventual extinction [6, 42]. Bhattacharjee et al. indicated solid surface radiation as the responsible mechanism of unsteady flame spread for thick PMMA slabs [52], and a non-dimensional radiation number was introduced to quantify these losses for flat fuels.

Flames over thick slabs of PMMA can be affected by additional conductive heat losses from the solid fuel to the sample holder, but this practical problem can be avoided by considering cylindrical samples. The cylindrical geometry has been extensively studied in theoretical and computational works [61, 62, 121, 122]. Cylindrical samples were tested in SSCE in a 50% oxygen atmosphere without forced flows, and the flames burnt the samples completely [114].

Cylindrical PMMA samples were also used in the more recent BASS investigation on the ISS to study the effect of a forced flow and oxygen concentration on flame spread [123, 124]. Even though the

cylinders in BASS could burn at very low flow velocities, when the forced flow was set to zero the flames were not able to spread and they eventually extinguished [125].

A scale analysis introduced by Higuera and Linan for cylinders revealed that curved surfaces are less affected by surface radiation losses than flat ones [67]. Curvature also increases flame spread rates, as discussed in Chapter 3 [63], because of enhanced heat transfer in the gas phase and faster temperature rise of the solid fuel.

The importance of surface radiation in a quiescent environment is still not clear because of the peculiarity of the burning conditions. Numerical models suffer from extremely small values of spread rate and flow velocity (resulting in extremely large diffusion length). In this work we investigate the importance of surface radiation on flame spread in the quiescent environment and different oxygen levels, to establish if the extinction mechanisms for flat fuels apply to cylindrical samples as well.

5.4.2 Effects of Fuel Geometry on Radiation

During the 1990s, several experiments using cellulosic fuel (filter paper) and PMMA were performed on the Space Shuttle for the Solid Surface Combustion Experiment (SSCE), more than 15 years after the tests in Skylab [4]. SSCE explored the effect of oxygen concentration (up to 70%) and pressure levels (1, 1.5 and 2 atm) in a quiescent environment for flat thin and thick fuels. Also two PMMA rods were later burnt at 50% oxygen and 1 atm. Flames over cellulosic samples have been already discussed in the past [112] and will not be reported here. We focus instead on the acrylic samples, and in particular on the cylindrical samples that can be compared to the ones used in BASS.

The two PMMA cylinders tested during SCCE are shown in Fig. 5.13, and were burnt in 1998 on STS-91, the last Shuttle-Mir Docking mission. The thicker cylinder (top one in Fig. 1) had a diameter of 6.4 mm and length of 40 mm, but the first half was hollow with an external thickness of 1 mm [114]. The thinner cylinder instead had a diameter of 2 mm with similar length (44 mm), and both samples were burnt with pressure of 1 atm with an oxygen concentration of 50%, inside of the 39L combustion chamber designed for SSCE [4].

The flat PMMA samples used in SSCE showed a tendency to extinguish in a quiescent environment also with high oxygen concentration, because of the high thermal losses through surface radiation related to the high vaporization temperature. However, flames over the PMMA rods seem to spread steadily, even though the flame lengths grow for the entire experiment.

Due to the large technological gap in image acquisition between SSCE (1990s) and BASS (2010s), the video quality of the cylinders burning in SSCE is much lower than the ones in BASS, but still enough to extrapolate important qualitative results.

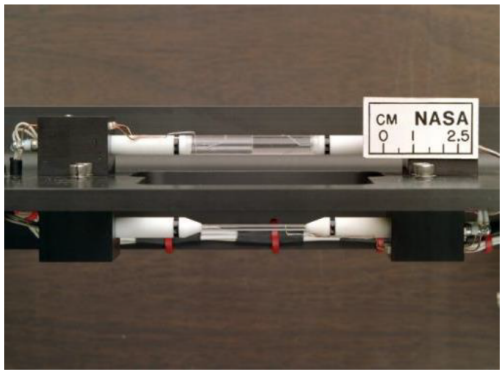

Figure 5.13: Picture of the two cylindrical samples tested in 1998 (*Credit: NASA*).

Figure 5.14 shows frames at different time after ignition of the flame generated over the thicker cylinder, which was hollow in the first half. The flame gets bigger and bigger, but the speed of the flame leading edge is constant as can be interpolated from the flame front position during time as shown in the graph on the left of Fig. 5.15. The blue flame front was tracked with FIAT, starting from the initial flame right after the igniter went off (second frame from left in Fig. 5.14), and ending when it reached the end of the sample (about 90 s after ignition). The transition between the blue flame in the second frame to the bright and yellow one at later times suggests that the flame can burn in a quiescent environment in contrast with flat fuels. When the main region of the flame reaches the fuel transition from hollow to full sections (between 40 and 50 s), it adjusts to the new thickness with strong changes in color and brightness, and the blue flame front basically becomes invisible in the video. The spread rates obtained from leading edge tracking with FIAT differ from the previously published values [114] of less than 10%, except for the full section of the thicker cylinder that is much lower (only 40% of the previously reported value). The flame over the thinner cylinder is so fast that it only takes a few seconds to spread along the 44 mm sample (about 8 s as shown in Fig. 5.15). Even though the thin cylinder has the same fuel thickness of the hollow section of the thicker sample (1 mm), the flame spreads more than three times faster because of the smaller curvature. Beside the absolute values of the spread rate, Fig. 5.15 shows that flames advance steadily, unlike the unsteady propagation on the thick slabs.

The experimental cases are not enough to establish if the flames over the two cylindrical samples of SSCE were completely steady, especially because all the cylinders in BASS extinguished when $V_g = 0$.

An energy balance and a scale analysis can be used to study the importance of surface radiation. Delichatsios et al. [63] compared flat and cylindrical fuels, and they showed that the heat transferred from the flame to the virgin fuel is enhanced due to curvature (see Chapter 3). The constant c of Eq. 3.4 has a value of 3.2 for microgravity [63], but it can be neglected for scale analysis. Neglecting surface radiation, only the conductive term in the gas phase and the vaporization term in the solid phase are responsible of

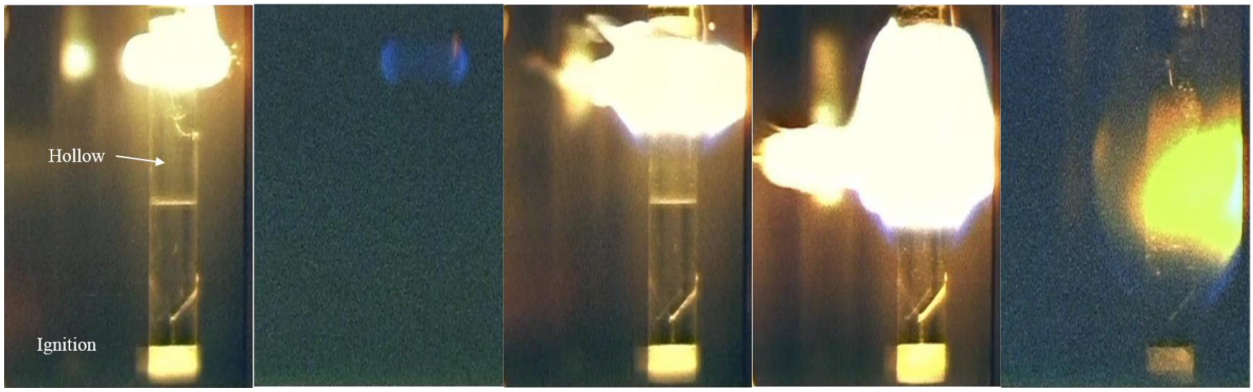

Figure 5.14: Frames of the SSCE video where a flame spreads over a cylinder (diameter of 6.4 mm) in a quiescent environment and oxygen concentration of 50%. Referring to the ignition time, the frames were captured at (starting from left to right): 0, 4, 21, 36, 66 s.

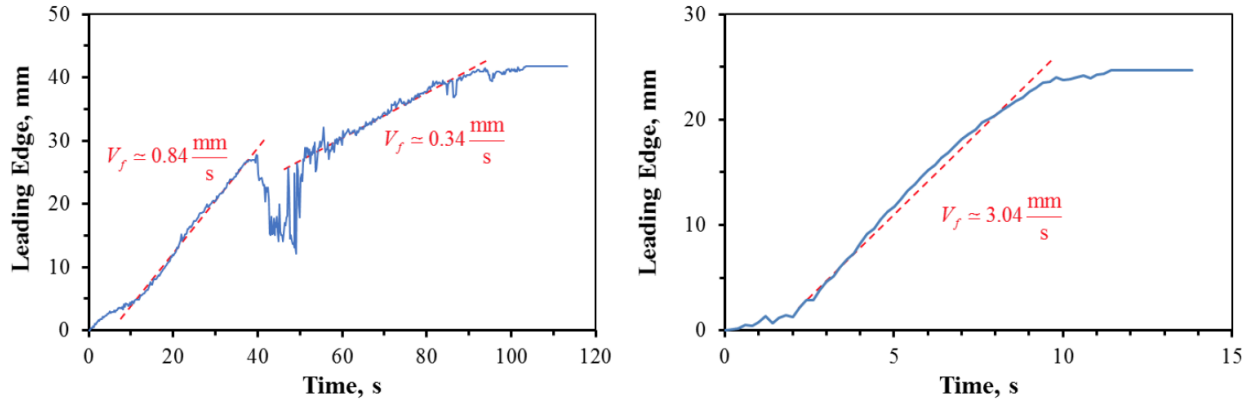

Figure 5.15: Position of the leading edge during time of the 6.4 mm cylinder (left), and 2 mm (right).

flame spread [52]:

$$V_f \rho_s c_s \left(T_v - T_\infty\right) \pi \left[r^2 - \left(r - \tau_h\right)^2\right] \sim \lambda_g \left(T_f - T_v\right) f_{\text{cyl}} 2\pi r \tag{5.2}$$

Therefore, the spread rate in the thermal regime can be obtained:

$$V_{f,\text{cyl,thn}} \sim f_{\text{cyl}} \left(1 - \frac{\tau_h}{2r}\right)^{-1} \frac{\pi}{4} \frac{\lambda_g}{\rho_s c_s \tau_h} \cdot F \tag{5.3}$$

Which corresponds to Eq. 3.6 in case of thin cylynders ($\tau_h = r$), whereas the expression following from the energy balance for τ_h (Eq. 3.5) can be used for thick fuels (Eq. 3.7).

The distinction between thermally thin and thick limits fades away in a quiescent environment ($V_g = 0$). The gas diffusive length becomes $L_g \sim \alpha_g/(V_f + V_g) \sim \alpha_g/(V_f)$, and since τ_h is related to L_g, this value increases because of the small V_f (in presence of a flow typically $V_g \gg V_f$). In other words, we can define the penetration depth as [42, 63]:

$$\tau_h \sim \sqrt{\alpha_s t} \sim \sqrt{\alpha_s L_g / V_f} \qquad \rightarrow \qquad \tau_h \sim \sqrt{\alpha_s \alpha_g}/V_f \tag{5.4}$$

Considering thin PMMA cylinders, we could substitute Eq. 3.6 in Eq. 5.4 to get a relation between thermal depth and radius, that is:

$$\tau_h \sim \frac{\sqrt{\alpha_s \alpha_g}\rho_s c_s}{2\pi f_{\text{cyl}} \lambda_g} r \tag{5.5}$$

From this relation we can see that the penetration depth is directly proportional to the fuel radius, and the proportionality factor is constant except for f_{cyl}. This term, however, does not have a strong influence on τ_h, because in a quiescent environment it becomes:

$$f_{\text{cyl,q}} = \frac{\frac{\alpha_g}{V_f r}}{\ln\left(1 + \frac{\alpha_g}{V_f r}\right)} \tag{5.6}$$

The spread rate depends on f_{cyl} again, but it is also known that large variations in V_f in Eq. 3.6 are due to the inverse proportionality with r. Therefore, the product $V_f \cdot r$ can be considered almost constant, or at least a secondary effect on Eq. 5.4. Therefore, larger radii cause the penetration depth to increase as well. The direct proportionality between the two suggests that in a quiescent environment cylinders can be considered thermally thin (no temperature gradient along thickness) unless the product $V_f \cdot r$ causes large variations of the cylindrical factor. In other words, the flame has enough time to heat up the entire fuel thickness before proceeding along the virgin fuel, on the contrary of what happens with an external flow. Flame spread rate still decreases with thickness, as proven by the spread rates of SSCE, but both sample diameters would act like thin fuels.

The situation changes if we include surface radiation in the energy balance of Eq. 5.2:

$$V_f \rho_s c_s \left(T_v - T_\infty\right) \pi 2 r \tau_h \left(1 - \frac{\tau_h}{2r}\right) + \epsilon\sigma \left(T_v^4 - T_\infty^4\right) 2\pi r L_g \sim \lambda_g \left(T_f - T_v\right) f_{\text{cyl}} 2\pi r \tag{5.7}$$

This equation can be normalized and solved for the spread rate; introducing the non-dimensional terms $\eta_f = V_f/V_{f,\text{th}}$ and $\eta_g = V_g/V_{f,\text{th}}$, with $V_{f,\text{th}}$ corresponding to V_f in the thermal regime. We can rewrite the previous equation as:

$$(\eta_f + \eta_g)(\eta_f - 1) + \mathbb{R} \sim 0 \tag{5.8}$$

where

$$\mathbb{R} = \left(1 - \frac{\tau_h}{2r}\right) \frac{\varepsilon \sigma \tau_h}{\lambda_s} \frac{\Omega^2}{f_{\text{cyl}}^2 F^2} \frac{T_v^4 - T_\infty^4}{T_v - T_\infty} \qquad \text{and} \qquad \Omega^2 = \frac{\lambda_s \rho_s c_s}{\lambda_g \rho_g c_g} \tag{5.9}$$

$\mathbb{R}$ is the so-called radiation number, and it is equivalent to the one obtained for flat fuels except for the cylindrical factors [52]. It should be noticed that no assumptions have been made on fuel thickness. This dependence is included in the length scale τ_h, which depends on the flow conditions as illustrated above.

To show how the two extra terms in the cylindrical radiation number influence its value, we consider a flat sample with the same thickness as the radius of the thicker cylindrical PMMA sample, which was 1 mm in the hollow section and 3.2 mm in the other half. By using the properties listed in Table A.1, and the experimental values of the spread rate obtained with FIAT to estimate f_{cyl} (the diffusion length in the gas phase would otherwise be hard to determine in a quiescent environment because of the dependence on the small velocity scale V_f), we can calculate the radiation numbers for flat and cylindrical geometries:

$$\mathbb{R}_{\text{flat}} = 40.02; \qquad \mathbb{R}_{\text{cyl}} = 0.68 \qquad (\tau = 1\text{mm}) \tag{5.10}$$

$$\mathbb{R}_{\text{flat}} = 128.08; \qquad \mathbb{R}_{\text{cyl}} = 0.33 \qquad (\tau = 3.2\text{mm}) \tag{5.11}$$

The radiation number of the flat geometry is one order of magnitude larger than the respective cylindrical in the case of $\tau = 1$ mm, and even more in the case of $\tau = 3.2$ mm, indicating that surface radiation is very important in flame extinction over flat samples, while it might not play an important role in the cylindrical geometry. Using the spread rate values from Altenkirch et al. [114], the radiation numbers do not change significantly, $\mathbb{R}_{\text{cyl}} = 0.48$ for $\tau = 1$ mm, and $\mathbb{R}_{\text{cyl}} = 0.70$ for $\tau = 3.2$ mm. For simplicity, we assumed $\varepsilon = 1$, because a lower value would just reduce the radiation numbers without changing the order of magnitude between the two geometries. The flame temperature was calculated at equilibrium [111], resulting in $T_f = 2800$ K, whereas $T_v = 650$ K and $T_\infty = 300$ K.

When the oxygen concentration is lower, for example 21% as in some of the BASS experiments, the only thermodynamic parameter that changes significantly is the flame temperature ($T_f = 2300$ K at equilibrium), and the relative radiation numbers are: $\mathbb{R}_{\text{cyl}} = 0.81$ for $\tau_h = 1$ mm, and $\mathbb{R}_{\text{cyl}} = 1.19$ for $\tau_h = 3.2$ mm. These values are calculated to compare the effect of a possible variation of oxygen concentration on surface radiation, therefore the values of f_{cyl} were considered the same as before although the spread rate would tend to zero. Higher values of f_{cyl} imply lower surface radiation, suggesting that extinction over cylindrical surfaces is not driven by solid radiation as for flat fuels. Other mechanisms, such as gas-phase radiation, might be responsible for that.

Chapter 5, in part, has been published in Combustion Science and Technology (L. Carmignani, S. Bhattacharjee, S.L. Olson, P.V. Ferkul, Boundary Layer Effect on Opposed-Flow Flame Spread and Flame Length over Thin Polymethyl-Methacrylate in Microgravity, Combust. Sci. Technol. 190, pp. 534-548, 2018), Fire Technology (L. Carmignani, K. Dong, S. Bhattacharjee, Radiation from flames in a microgravity environment: experimental and numerical investigations, Fire Technol., 2019, in press), and other parts are extracted from (L. Carmignani, S. Sato, S. Bhattacharjee, Flame spread over acrylic cylinders in microgravity: effect of surface radiation on flame spread and extinction, 48th ICES, Albuquerque, NM, July 2018). The thesis author was the primary investigator in these publications.

Chapter 6

Conclusions

Opposed-flow flame spread is a complex problem that depends on many variables. Theoretical and numerical models offer a basic understanding of the problem, whereas experimental studies can give information in a broader range of conditions. In this work we combined results from experiments, computations and scale analysis to compensate some of the limitations related to each methods.

In downward flame spread, the spread rate is significantly enhanced by the presence of sharp edges. The internal angle at the edge controls the propagation of the edge flame: the sharper the edge, the faster the flame. Edge flames begin spreading steadily immediately after ignition, while the central flame accelerates and eventually reaches the same value. For irregular cross-sections, different edge flames propagate at different spread rates, and the global flame does not reach steady state. An effective radius is defined to convert the edge propagation into a cylindrical propagation problem, which spread rate equations are known. Based on this experimental study, different types of cross sections can be arranged in order of fire safety.

The mass burning rate of downward spreading flames is studied through the burn angle, which represents the competition between flame spread and surface regression. Experimental results from previous works were included to firmly establish that the burn angle increases with fuel thickness, going from 0° for very thin fuel to a maximum value of 20° for thicknesses between 2 and 3 mm, before decreasing to an asymptotic limit of 11° for thick fuels. The rapid increase of burn angles in thin fuels is well explained by a phenomenological model. However, the characteristic hump of the experimental data can only be explained with a thickness-dependent pyrolysis region temperature, as suggested by the numerical results.

A forced flow reduces flame spread rates, and flame extinction is tested over thin fuels. The results can be correlated to a critical extinction velocity. However, this velocity does not necessarily reflect the free stream velocity. The velocity gradient encountered in a developing boundary layer can be important also at relatively low velocities.

The mass burning rate, in contrast with the spread rate, is not changing in the range of velocity used in this work (0 - 150 cm/s). A scale analysis of the classical problems of surface regression and flame spread shows the same qualitative trends of the closed-form solutions obtained by Emmons and de Ris. An alternative B-number is defined starting from an energy balance on the fuel surface, taking into consideration the flame stand-off distance and the effective velocity facing the flame embedded in a boundary layer. By using B' the average mass burning rate in the pyrolysis region can be estimated for different burning conditions such as oxygen concentration, ambient pressure, and gravity level.

Overall, a forced flow affects more the gas phase (reducing the residence time) than the solid phase, as suggested by the results on flame length and spread rate. Without a forced flow, the flame length is proportional to the fuel mass flux. However, with a forced flow the flame length is better described by the dependence on flow veloci. The amount of fuel burning is limited by the oxidizer reaching the flame, and the flame length can be predicted by considering the diffusion of oxygen inside of the thermal boundary layer.

The effect of a developing boundary layer over thin PMMA sheets is studied in a microgravity environment at low forced velocities. Computational results show that the flame strengthens as it propagates into a thinning boundary layer, as reflected by its size, temperature, and spread rate. The experimental flames from BASS show an increase in size as well. However, the spread rate does not show any significant increase. An experiment where the flame is allowed to propagate all the way to the edge of the boundary layer is necessary before the computational results can be definitively verified.

Despite the importance of radiation in microgravity flames, direct measurements of radiation emissions are rare. The total hemispherical emission recorded in the BASS experiments and its variation with burning conditions is studied experimentally by isolating the effects of flow velocity, oxygen concentration and fuel thickness. The numerical model reproduces in a qualitative manner the observed dependence of the flame shape and radiation signature on the parameters. Higher flow velocities are beneficial for flame temperature and flame size, but the flames can shrink causing the radiative emission to drop. The experimental data to describe the effect of oxygen concentration are not enough to establish a trend, but they suggest that soot production might play a bigger role than flame temperature with increasing oxygen levels. The total flame area does not change significantly with fuel thickness, and the increase in radiation is attributed to a larger emission from the pyrolysis region. Fuel burning rates, calculated from the instantaneous flame spread rates and compared to the simulated values, are shown to correlate well with the radiation signatures. Measurements of total and yellow areas, however, show similar trends for total radiation, and are supported by the numerical results. This suggests that soot (not included in the numerical model), might play a smaller role in the radiative emission of a flame over solid fuels rather than from gaseous fuels because of the strong influence of surface radiation. Further studies are needed to prove this conclusion. Understanding

the radiative transfer of flames in reduced gravity is necessary to improve fire safety onboard spacecraft.

Finally, the review of previous videos from SSCE suggested that flames over cylindrical fuels could spread steadily in a quiescent environment, even though flames over flat fuels cannot reach steady conditions. Our findings include the following: (i) in a quiescent environment cylindrical fuels behave as thermally thin because the thermal penetration depth increases in step with an increase in cylinder radius. (ii) Cylindrical surfaces are less affected by surface radiation than flat surfaces because of their curvature. (iii) A comparison between the burning conditions of SCCE and BASS shows that surface radiation losses might not be responsible for the extinction of cylindrical fuels, in contrast with the behavior of flat fuels. An accurate analysis of gas-phase radiation is needed to evaluate its importance at extinction.

Bibliography

[1] D. Dietrich, H. Ross, Y. Shu, P. Chang, and J. T'ien. "Candle Flames in Non-Buoyant Atmospheres". *Combust. Sci. Technol.* 156.1 (2000), pp. 1–24.

[2] S. Olson and F. Miller. "Experimental comparison of opposed and concurrent flame spread in a forced convective microgravity environment". *Proc. Combust. Inst.* 32.2 (2009), pp. 2445–2452.

[3] M. Thomsen, C. Fernandez-Pello, G. A. Ruff, and D. L. Urban. "Buoyancy effects on concurrent flame spread over thick PMMA". *Combust. Flame* 199 (2019), pp. 279–291.

[4] M. K. King and H. D. Ross. "Overview of the NASA Microgravity Combustion Program". *AIAA J.* 36.8 (1998), pp. 1337–1345.

[5] K. Dotson, P. Sunderland, Z.-G. Yuan, and D. Urban. "Laminar smoke points of coflowing flames in microgravity". *Fire Saf. J.* 46.8 (2011), pp. 550–555.

[6] R. A. Altenkirch, L. Tang, K. Sacksteder, S. Bhattacharjee, and M. A. Delichatsios. "Inherently unsteady flame spread to extinction over thick fuels in microgravity". *Symp. (Int.) Combust.* 27 (1998), pp. 2515–2524.

[7] *NASA-STD-6001B, Flammability, Offgassing, and compatibility Requirements And Test Procedures.* Tech. rep. NASA, 2011.

[8] S. L. Olson and P. V. Ferkul. "Microgravity Flammability of PMMA Rods in Concurrent Flow". *9th U.S. National Combust. Meeting, May 17 - May 20, Cincinnati, OH.* 2015.

[9] G. Jomaas, J. L. Torero, C. Eigenbrod, J. Niehaus, S. L. Olson, P. V. Ferkul, G. Legros, A. C. Fernandez-Pello, A. J. Cowlard, S. Rouvreau, N. Smirnov, O. Fujita, J. S. T'ien, G. A. Ruff, and D. L. Urban. "Fire safety in space – beyond flammability testing of small samples". *Acta Astronautica* 109 (2015), pp. 208–216.

[10] K. E. Lange, A. T. Perka, B. E. Duffield, and F. F. Jeng. *Bounding the Spacecraft Atmosphere Design Space for Future Exploration Missions.* Tech. rep. NASA Johnson Space Center, 2005.

[11] M. Thomsen, C. Fernandez-Pello, X. Huang, S. L. Olson, and P. V. Ferkul. "Opposed flow burning of PMMA cylinders in normoxic atmospheres". *Fire Saf. J.* 110 (2019), (in press).

[12] I. S. Wichman. "Theory of opposed-flow flame spread". *Prog. Energy Combust. Sci.* 18 (1992), pp. 553–593.

[13] G. Lengelle. "Thermal degradation kinetics and surface pyrolysis of vinyl polymers". *AIAA J.* 8.11 (1970), pp. 1989–1996.

[14] F. Williams. "Mechanisms of fire spread". *Symp. (Int.) Combust.* 16.1 (1977), pp. 1281–1294.

[15] A. C. Fernandez-Pello and F. A. Williams. "A theory of laminar flame spread over flat surfaces of solid combustibles". *Combust. Flame* 28 (1977), pp. 251–277.

[16] S. Crescitelli, F. Pota, G. Santo, and V. Tufano. "Influence of Solid Phase Thermal Properties on Flame Spread over Polymers". *Combust. Sci. Technol.* 27 (1981), pp. 75–78.

[17] S. Rybanin. "The dependence of the flame spread rate over solid fuel on Damköhler number and heat loss". *Symposium (International) on Combustion* 26 (1996), pp. 1487–1493.

[18] S. Bhattacharjee, A. Simsek, F. Miller, S. Olson, and P. Ferkul. "Radiative, thermal, and kinetic regimes of opposed-flow flame spread: A comparison between experiment and theory". *Proc. Combust. Inst.* 36.2 (2017), pp. 2963–2969.

[19] S. Bhattacharjee, M. Bundy, C. Paolini, G. Patel, and W. Tran. "A novel apparatus for flame spread study". *Proc. Combust. Inst.* 34.2 (2013), pp. 2513–2521.

[20] W. Camperchioli. *Narrow Angle Wide Spectral Range Radiometer Design*. Tech. rep. NASA Glenn Research Center, 2005.

[21] Y. Son. "Transport and Chemical Effects on Flame Spread over Thick Solid Fuel Beds in Microgravity and Earth Gravity Environments". PhD thesis. University of Southern California, 2004.

[22] P. Ferkul, S. Olson, F. Takahashi, M. Endo, M. Johnston, and J. T'ien. "Thickness and Fuel Preheating Effects on Material Flammability in Microgravity from the BASS Experiment". *29th Annual Meeting of the American Society for Gravitational and Space Research*. Nov. 2013.

[23] P. Ferkul, S. Bhattacharjee, A. Fernandez-Pello, F. Miller, S. Olson, F. Takahashi, and J. T'ien. "Combustion of Solids in Microgravity: Results from the BASS-II Experiment". *30th American Society for Gravitational and Space Research Conference*. Oct. 2014.

[24] S. Olson, P. Ferkul, S. Bhattacharjee, F. Miller, A. Fernandez-Pello, S. Link, J. T'ien, and I. Wichman. "Results from on-board CSA-CP and CDM Sensor Readings during the Burning and Suppression of Solids – II (BASS-II) Experiment in the Microgravity Science Glovebox (MSG)". *45th Int. Conf. Environmental Systems*. Bellevue, Washington, 2015.

[25] A. Nadertabar. "Flame analyzer: a matlab based flame spread analysis tool". MA thesis. San Diego State University, 2019.

[26] G. D. Celniker. "Flame Analyzer 2: A fully two dimensional flame spread video analysis tool". MA thesis. San Diego State University, 2017.

[27] R. F. McAlevy III and R. S. Magee. "The mechanism of flame spreading over the surface of igniting condensed-phase materials". *Symp. (Int.) Combust.* 12 (1969), pp. 215–227.

[28] A. C. Fernandez-Pello, S. R. Ray, and I. Glassman. "Flame spread in an opposed forced flow: the effect of ambient oxygen concentration". *Symp. (Int.) Combust.* 18 (1981), pp. 579–589.

[29] F. A. Lastrina, R. S. Magee, and R. F. M. III. "Flame spread over fuel beds: solid-phase energy considerations". *Symp. (Int.) Combust.* 13 (1971), pp. 935–948.

[30] T. Hirano, K. Sato, and K. Tazawa. "Instability of downward flame spread over paper in an air stream". *Combust. Flame* 26 (1976), pp. 191–200.

[31] S. Bhattacharjee, C. Paolini, W. Tran, J. R. Villaraza, and S. Takahashi. "Temperature and CO2 fields of a downward spreading flame over thin cellulose: A comparison of experimental and computational results". *Proc. Combust. Inst.* 35.3 (2015), pp. 2665–2672.

[32] A. Arakawa, K. Saito, and W. Gruver. "Automated infrared imaging temperature measurement with application to upward flame spread studies. Part I". *Combust. Flame* 92.3 (1993), 222–IN2.

[33] C. Qian and K. Saito. "An Empirical Model for Upward Flame Spread over Vertical Flat and Corner Walls". *Fire Saf. Sci.* (1997), pp. 285–296.

[34] A. Ito, D. Masuda, and K. Saito. "A study of flame spread over alcohols using holographic interferometry". *Combust. Flame* 83.3 (1991), pp. 375–389.

[35] T. Konishi, A. Ito, Y. Kudo, A. Narumi, K. Saito, J. Baker, and P. M. Struk. "Simultaneous measurement of temperature and chemicalspecies concentrations with a holographic interferometer and infrared absorption". *Appl. Opt.* 45.22 (2006), pp. 5725–5732.

[36] R. Klimek and T. Wright. *Spotlight Image Analysis.* Tech. rep. NASA Glenn Research Center, 2006.

[37] S. Olson, F. Miller, S. Jahangirian, and I. Wichman. "Flame spread over thin fuels in actual and simulated microgravity conditions". *Combust. Flame* 156.6 (2009), pp. 1214–1226.

[38] S. Bhattacharjee, W. Tran, M. Laue, C. Paolini, and Y. Nakamura. "Experimental validation of a correlation capturing the boundary layer effect on spread rate in the kinetic regime of opposed-flow flame spread". *Proc. Combust. Inst.* 35 (2015), pp. 2631–2638.

[39] G. Avinash, A. Kumar, and V. Raghavan. "Experimental analysis of diffusion flame spread along thin parallel solid fuel surfaces in a natural convective environment". *Combust. Flame* 165 (2016), pp. 321–333.

[40] S. Bhattacharjee and R. A. Altenkirch. "Radiation-controlled, opposed-flow flame spread in a microgravity environment". *Symp. (Int.) Combust.* 23.1 (1991), pp. 1627–1633.

[41] S. Bhattacharjee, R. A. Altenkirch, and K. Sacksteder. "The Effect of Ambient Pressure on Flame Spread Over Thin Cellulosic Fuel in a Quiescent, Microgravity Environment". *J. Heat Transfer* 118 (1996), pp. 181–190.

[42] J. West, L. Tang, R. A. Altenkirch, S. Bhattacharjee, K. Sacksteder, and M. A. Delichatsions. "Quiescent flame spread over thick fuels in microgravity". *Symp. (Int.) Combust.* 26.1 (1996), pp. 1335–1343.

[43] S. Bhattacharjee, R. Nagarkar, and Y. Nakamura. "A Correlation for an Effective Flow Velocity for Capturing the Boundary Layer Effect in Opposed-Flow Flame Spread over Thin Fuels". *Combust. Sci. Technol.* 186 (2014), pp. 975–987.

[44] S. Patankar. *Numerical Heat Transfer and Fluid Flow.* CRC Press, 1980.

[45] W. L. Grosshandler. *A Narrow-Band Model for Radiation Calculations in a Combustion Environment.* Tech. rep. Gaithersburg, MD: NIST, 1993.

[46] S. Bhattacharjee, C. Paolini, F. Miller, and R. Nagarkar. "Radiation signature in opposed-flow flame spread". *Prog. Computational Fluid Dynamics* 12 (2012), pp. 293–301.

[47] J. N. De Ris. "Spread of a laminar diffusion flame". *Symp. (Int.) Combust.* 12 (1969), pp. 241–252.

[48] M. A. Delichatsios. "Exact Solution for the Rate of Creeping Flame Spread over Thermally Thin Materials". *Combust. Sci. Technol.* 44 (1986), pp. 257–267.

[49] S. Bhattacharjee, M. Laue, L. Carmignani, P. Ferkul, and S. Olson. "Opposed-flow flame spread: A comparison of microgravity and normal gravity experiments to establish the thermal regime". *Fire Saf. J.* 79 (2016), pp. 111–118.

[50] L. Carmignani, B. Rhoades, and S. Bhattacharjee. "Correlation of Burning Rate with Spread Rate for Downward Flame Spread Over PMMA". *Fire Technol.* 54.3 (2018), pp. 613–624.

[51] A. C. Fernandez-Pello and F. A. Williams. "Laminar flame spread over PMMA surfaces". *Symp. (Int.) Combust.* 15 (1975), pp. 217–231.

[52] S. Bhattacharjee, R. Ayala, K. Wakai, and S. Takahashi. "Opposed-flow flame spread in microgravity-theoretical prediction of spread rate and flammability map". *Proc. Combust. Inst.* 30.2 (2005), pp. 2279–2286.

[53] G. Markstein and J. de Ris. "Upward fire spread over textiles". *Symp. (Int.) Combust.* 14.1 (1973), pp. 1085–1097.

[54] J. V. Creeden Jr and M. Sibulkin. "The Effect of an Uninhibited Edge on Downward Flame Propagation". *Combust. Sci. Technol.* 14.1-3 (1976), pp. 123–124.

[55] H. W. Emmons and T. Shen. "Fire spread in paper arrays". *Symp. (Int.) Combust.* 13.1 (1971), pp. 917–926.

[56] W. Mell and T. Kashiwagi. "Effects of finite sample width on transition and flame spread in microgravity". *Proc. Combust. Inst.* 28.2 (2000), pp. 2785–2792.

[57] W. Mell, S. Olson, and T. Kashiwagi. "Flame spread along free edges of thermally thin samples in microgravity". *Proc. Combust. Inst.* 28 (2000), pp. 2843–2849.

[58] C. Kumar and A. Kumar. "A Computational Study on Opposed Flow Flame Spread Over Thin Solid Fuels with Side-Edge Burning". *Combus. Sci. Technol.* 182.9 (2010), pp. 1321–1340.

[59] B. Comas and T. Pujol. "Experimental Study of the Effects of Side-Edge Burning in the Downward Flame Spread of Thin Solid Fuels". *Combust. Sci. Technol.* 184.4 (2012), pp. 489–504.

[60] J. Gong, X. Zhou, J. Li, and L. Yang. "Effect of finite dimension on downward flame spread over PMMA slabs: Experimental and theoretical study". *Int. J. Heat and Mass Transfer* 91 (2015), pp. 225–234.

[61] A. Fernandez-Pello and R. Santoro. "On the dominant mode of heat transfer in downward flame spread". *Symp. (Int.) Combust.* 17.1 (1979), pp. 1201–1209.

[62] M. Sibulkin and C. K. Lee. "Flame Propagation Measurements and Energy Feedback Analysis for Burning Cylinders". *Combust. Sci. Technol.* 9.3-4 (1974), pp. 137–147.

[63] M. A. Delichatsios, R. A. Altenkirch, M. F. Bundy, S. Bhattacharjee, L. Tang, and K. Sacksteder. "Creeping flame spread along fuel cylinders in forced and natural flows and microgravity". *Proc. Combust. Inst.* 28.2 (2000), pp. 2835–2842.

[64] S. Bhattacharjee, L. Carmignani, G. Celniker, and B. Rhoades. "Measurement of instantaneous flame spread rate over solid fuels using image analysis". *Fire Saf. J.* 91 (2017), pp. 123–129.

[65] K. Zhao, X. Zhou, X. Liu, W. Tang, M. Gollner, F. Peng, and L. Yang. "Experimental and theoretical study on downward flame spread over uninhibited PMMA slabs under different pressure environments". *Applied Thermal Engineering* 136 (2018), pp. 1–8.

[66] K. Zhao, X. Zhou, L. Yang, J. Gong, Z. Wu, Z. Huan, and X. Liu. "Width effects on downward flame spread over poly(methyl methacrylate) sheets". *J. Fire Sciences* 33.1 (2015), pp. 69–84.

[67] F. Higuera and A. Liñán. "Flame spread along a fuel rod in the absence of gravity". *Combust. Th. Modell.* 3.2 (1999), pp. 259–265.

[68] H. W. Emmons. "The Film Combustion of Liquid Fuel". *Z. Angew, Math. Mech.* 36 (1956), pp. 60–71.

[69] D. B. Spalding. "Combustion of liquid fuel in gas stream". *Fuel* 29 (1950), pp. 2–7.

[70] A. Rangwala. "Flame spread analysis using a variable B-number". *Fire Saf. Sci.* 9 (2008), pp. 243–254.

[71] J. L. Torero, T. Vietoris, G. Legros, and P. Joulain. "Estimation of a total mass transfer number from the standoff distance of a spreading flame". *Combust. Sci. Technol.* 174.11-12 (2002), pp. 187–203.

[72] M. Sibulkin, A. Kulkarni, and K. Annamalai. "Burning on a vertical fuel surface with finite chemical reaction rate". *Combust. Flame* 44.1 (1982), pp. 187–199.

[73] L. Zhou and A. C. Fernandez-Pello. "Turbulent burning of a flat fuel surface". *Fire Saf. Sci.* 3 (1991), pp. 415–424.

[74] R. Ananth, C. C. Ndubizu, and P. Tatem. "Burning rate distributions for boundary layer flow combustion of a PMMA plate in forced flow". *Combust. Flame* 135.1 (2003), pp. 35–55.

[75] L. Orloff, J. D. Ris, and G. Markstein. "Upward turbulent fire spread and burning of fuel surface". *Symp. (Int.) Combust.* 15 (1975), pp. 183–192.

[76] Y. Pizzo, J. Consalvi, P. Querre, M. Coutin, L. Audouin, B. Porterie, and J. Torero. "Experimental observations on the steady-state burning rate of a vertically oriented PMMA slab". *Combust. Flame* 152.3 (2008), pp. 451–460.

[77] A. V. Singh and M. J. Gollner. "Estimation of local mass burning rates for steady laminar boundary layer diffusion flames". *Proc. Combust. Inst.* 35.3 (2015), pp. 2527–2534.

[78] A. V. Singh and M. J. Gollner. "Steady and transient pyrolysis of a non-charring solid fuel under forced flow". *Proc. Combust. Inst.* 36.2 (2017), pp. 3157–3165.

[79] T. Ahmad and G. Faeth. "Turbulent wall fires". *Symp. (Int.) Combust.* 17 (1979), pp. 1149–1160.

[80] S. Agrawal. "Determination of Surface Heat Flux in the Burning Zone During Wind-Aided Flame Spread Using Burned PMMA Samples". *Combust. Sci. Technol.* 91.1-3 (1993), pp. 187–190.

[81] L. Krishnamurthy and F. Williams. "Laminar combustion of polymethylmethacrylate in O2/N2 mixtures". *Symp. (Int.) Combust.* 14.1 (1973), pp. 1151–1164.

[82] C. Ndubizu, R. Ananth, and P. Tatem. "Transient burning rate of a noncharring plate under a forced flow boundary layer flame". *Combust. Flame* 141.1 (2005), pp. 131–148.

[83] K. Mekki, A. Atreya, S. Agrawal, and I. Wichman. "Wind-aided flame spread over charring and non-charrring solids: An experimental investigation". *Symp. (Int.) Combust.* 23 (1991), pp. 1701–1707.

[84] A. C. Fernandez-Pello, S. R. Ray, and I. Glassman. "Downward Flame Spread In an Opposed Forced Flow". *Combust. Sci. Technol.* 19.1-2 (1978), pp. 19–30.

[85] M. Sibulkin and M. W. Little. "Propagation and extinction of downward burning fires". *Combust. Flame* 31 (1978), pp. 197–208.

[86] X. Huang, S. Link, A. Rodriguez, M. Thomsen, S. Olson, P. Ferkul, and C. Fernandez-Pello. "Transition from opposed flame spread to fuel regression and blow off: Effect of flow, atmosphere, and microgravity". *Proc. Combust. Inst.* 37.3 (2019), pp. 4117–4126.

[87] M. Ayani, J. Esfahani, and R. Mehrabian. "Downward flame spread over PMMA sheets in quiescent air: Experimental and theoretical studies". *Fire Saf. J.* 41.2 (2006), pp. 164–169.

[88] Y.-T. T. Liao and J. S. T'ien. "A numerical simulation of transient ignition and ignition limit of a composite solid by a localised radiant source". *Combust. Th. Modell.* 17.6 (2013), pp. 1096–1124.

[89] A. E. Frey Jr. and J. S. T'ien. "A theory of flame spread over a solid fuel including finite-rate chemical kinetics". *Combust. Flame* 36 (1979), pp. 263–289.

[90] A. Kacem, M. Mense, Y. Pizzo, G. Boyer, S. Suard, P. Boulet, G. Parent, and B. Porterie. "A fully coupled fluid/solid model for open air combustion of horizontally-oriented PMMA samples". *Combust. Flame* 170 (2016), pp. 135–147.

[91] K. McGrattan, S. Hostikka, R. McDermott, J. Floyd, and M. Vanella. *Fire Dynamics Simulator Technical Reference Guide Volume 1: Mathematical Model.* NIST. 2013.

[92] W. A. Sirignano. "A Critical Discussion of Theories of Flame Spread across Solid and Liquid Fuels". *Combust. Sci. Technol.* 6.1-2 (1972), pp. 95–105.

[93] A. Kulkarni and C. Kim. "Heat Loss to the Interior of a Free Burning Vertical Wall and its Influence on Estimation of Effective Heat of Gasification". *Combust. Sci. Technol.* 73 (1990), pp. 493–504.

[94] F. Roper. "The prediction of laminar jet diffusion flame sizes: Part I. Theoretical model". *Combust. Flame* 29 (1977), pp. 219–226.

[95] F. Roper, C. Smith, and A. Cunningham. "The prediction of laminar jet diffusion flame sizes: Part II. Experimental verification". *Combust. Flame* 29 (1977), pp. 227–234.

[96] P. Pagni and T. Shih. "Excess pyrolyzate". *Symp. (Int.) Combust.* 16.1 (1977), pp. 1329–1343.

[97] A. C. Fernandez-Pello. "Pool and wall fires: some fundamental aspects". *Proc. ASME/JSME Thermal Eng. Conf.* ASME Book 10309E (1991), pp. 261–268.

[98] P. Thomas. "The size of flames from natural fires". *Symp. (Int.) Combust.* 9.1 (1963), pp. 844–859.

[99] B. D. Wood, P. L. Blackshear Jr., and E. R. G. Eckert. "Mass Fire Model: An Experimental Study of the Heat Transfer to Liquid Fuel Burning from a Sand-Filled Pan Burner". *Combust. Sci. Technol.* 4.1 (1971), pp. 113–129.

[100] J. S. West. "Forced opposed flow flame spread over flat solid fuels in the thermal, near quiescent and chemical kinetic regimes." PhD thesis. University of California, San Diego and San Diego State University, CA, 1998.

[101] R. W. Bilger. "The Structure of Diffusion Flames". *Combustion Science and Technology* 13.1-6 (1976), pp. 155–170.

[102] C. Law. "Heat and mass transfer in combustion: Fundamental concepts and analytical techniques". *Prog. Energy Combust. Sci.* 10.3 (1984), pp. 295–318.

[103] I. S. Wichman, F. A. Williams, and I. Glassman. "Theoretical aspects of flame spread in an opposed flow over flat surfaces of solid fuels". *Symp. (Int.) Combust.* 19 (1982), pp. 835–845.

[104] I. S. Wichman. "A Model Describing the Influences of Finite-Rate Gas-Phase Chemistry on Rates of Flame Spread Over Solid Combustibles". *Combusti. Sci. Technol.* 40.5-6 (1984), pp. 233–255.

[105] R. Altenkirch and M. Vedha-Nayagam. "Opposed-flow flame spread and extinction in mixed-convection boundary layers". *Symp. (Int.) Combust.* 22 (1989), pp. 1495–1500.

[106] I. S. Wichman. "Flame spread in an opposed flow with a linear velocity gradient". *Combust. Flame* 50 (1983), pp. 287–304.

[107] C. K. Law. *Combustion Physics*. Cambridge University Press, 2006.

[108] R. C. Lock. "The Velocity Distribution in the laminar boundary layer between parallel streams". *Quarterly J. Mechanics and Appl. Mathematics* 4.1 (1951), pp. 42–63.

[109] S. Li, Q. Yao, and C. K. Law. "The Emmons problem: Role of an impermeable leading segment". *Combust. Flame* 203 (2019), pp. 334–340.

[110] A. Bejan. *Convection Heat Transfer*. John Wiley and Sons, 1984.

[111] S. Bhattacharjee and C. Paolini. "Property evaluation in The Expert System for Thermodynamics ("TEST") web application". *Calphad* 33.2 (2009). Tools for Computational Thermodynamics, pp. 343–352.

[112] S. Bhattacharjee and R. A. Altenkirch. "A comparison of theoretical and experimental results in flame spread over thin condensed fuels in a quiescent, microgravity environment". *Symp. (Int.) Combust.* 24 (1992), pp. 1669–1676.

[113] P. A. Ramachandra, R. A. Altenkirch, S. Bhattacharjee, L. Tang, K. Sacksteder, and M. K. Wolverton. "The behavior of flames spreading over thin solids in microgravity". *Combust. Flame* 100.1 (1995), pp. 71–84.

[114] R. A. Altenkirch, M. F. Bundy, L. Tang, S. Bhattacharjee, K. Sacksteder, and M. A. Delichatsios. "Reflight of the solid surface combustion experiment: flame radiation near extinction". *5th Int. Microgravity Combust. Workshop*. NASA Glenn Research Center. Cleveland, OH, 1999.

[115] S. Bhattacharjee, A. Simsek, S. Olson, and P. Ferkul. "The critical flow velocity for radiative extinction in opposed-flow flame spread in a microgravity environment: A comparison of experimental, computational, and theoretical results". *Combust. Flame* 163 (2016), pp. 472–477.

[116] A. C. Fernandez-Pello and T. Hirano. "Controlling Mechanisms of Flame Spread". *Combust. Sci. Technol.* 32 (1983), pp. 1–31.

[117] D. L. Urban, P. Ferkul, S. Olson, G. A. Ruff, J. Easton, J. S. T'ien, Y.-T. T. Liao, C. Li, C. Fernandez-Pello, J. L. Torero, G. Legros, C. Eigenbrod, N. Smirnov, O. Fujita, S. Rouvreau, B. Toth, and G. Jomaas. "Flame spread: Effects of microgravity and scale". *Combust. Flame* 199 (2019), pp. 168–182.

[118] B. Haynes and H. Wagner. "Soot formation". *Prog. Energy Combust. Sci.* 7.4 (1981), pp. 229–273.

[119] I. Glassman. "Soot formation in combustion processes". *Symp. (Int.) Combust.* 22.1 (1989), pp. 295–311.

[120] V. Apte, R. Bilger, A. Green, and J. Quintiere. "Wind-aided turbulent flame spread and burning over large-scale horizontal PMMA surfaces". *Combustion and Flame* 85.1 (1991), pp. 169–184.

[121] J. S. Goldmeer, J. S. T'ien, and D. L. Urban. "Combustion and extinction of PMMA cylinders during depressurization in low-gravity". *Fire Saf. J.* 32.1 (1999), pp. 61–88.

[122] O. Fujita, K. Nishizawa, and K. Ito. "Effect of low external flow on flame spread over polyethylene-insulated wire in microgravity". *Proc. Combust. Inst.* 29.2 (2002), pp. 2545–2552.

[123] S. L. Olson and P. V. Ferkul. "Microgravity flammability boundary for PMMA rods in axial stagnation flow: Experimental results and energy balance analyses". *Combust. Flame* 180 (2017), pp. 217–229.

[124] S. Link, X. Huang, C. Fernandez-Pello, S. Olson, and P. Ferkul. "The Effect of Gravity on Flame Spread over PMMA Cylinders". *Scientific Reports* 8.1 (2018), pp. 1–9.

[125] S. Link, X. Huang, C. Fernandez-Pello, S. Olson, and P. Ferkul. "The Effect of Gravity on Flame Spread over PMMA Cylinders in Opposed Flow with Variable Oxygen Concentration". *46th Int. Conf. Environmental Systems*. Vienna, Austria, 2016.

Appendix A

Tables

A.1 PMMA Properties

Table A.1: PMMA and gas property values

Property	Symbol	Unit	PMMA	Air
Density	ρ	kg/m^3	1190	0.518
Pre-exponential factor	A_s	1/s	81.87	-
Pre-exponential factor	A_g	m^3/(kg·s)	-	8.93·10^7
Specific heat	c	kJ/(kg·K)	1.465	1.183
Thermal conductivity	λ	W/(m·K)	0.18	0.052
Combustion enthalpy	Δh_c°	MJ/kg	-25.9	-
Vaporization enthalpy	Δh_v°	MJ/kg	0.941	-

A.2 The BASS Experiments

Table A.2: Experimental conditions of the BASS experiments; values of the flow velocity indicate initial and final values.

Experiment	Thickness, mm	Width, mm	Flow Velocity, cm/s	Oxygen concentration
B1	0.1	20	5-0	22.2
B2	0.2	20	5-0	22.2
B3	0.1	20	2-0	22.2
B4	0.3	20	5-0	22.2
B5	0.2	20	5-0	22.2
B6	0.1	20	1-7	21
B7	0.4	20	2-0	22.2
B8	0.2	20	10-42	21
B9	0.1	20	2-1	21
B10	0.2	10	5-0	21
B11	0.2	20	5-0	21
B12	0.3	20	2-0	22.2
B13	0.4	20	10-0	21
B14	0.2	10	No ignition	15
B15	0.1	20	10-42	21
B16	0.1	20	2-0	17.3
B17	0.2	10	5-0	17.5
B18	0.2	10	10-42	17.4
B19	0.1	20	10-20	17.3
B20	0.1	20	5-0	17.4
B21	0.2	10	5-0	20.8
B22	0.2	10	5-0	20.7